FURTHER DEVELOPMENTS IN 2D OPTICALLY STIMULATED LUMINESCENCE DOSIMETRY

BASED ON Al_2O_3 and MgB_4O_7

By

NISHAN SHRESTHA

Bachelor of Science in Engineering Physics
Southern Arkansas University
Magnolia, AR
2013

Master of Science in Medical Physics
Oklahoma State University
Stillwater, OK
2017

Submitted to the Faculty of the
Graduate College of the
Oklahoma State University
in partial fulfillment of
the requirements for
the Degree of
DOCTOR OF PHILOSOPHY
May, 2020

FURTHER DEVELOPMENTS IN 2D OPTICALLY STIMULATED LUMINESCENCE DOSIMETRY

BASED ON AL2O3 AND MGB4O7

Thesis Approved:

Eduardo G. Yukihara, Ph.D.

Thesis Adviser

John Mintmire, Ph.D.

Salahuddin Ahmad, Ph.D.

Piao, Daqing (Daching), Ph.D.

ACKNOWLEDGEMENTS

Firstly, I would like to express my special appreciation and thanks to my advisor **Dr. Eduardo G. Yukihara**. I would like to thank you for believing in me, encouraging me and allowing me to grow not only as a researcher but the person I am today. I could not have asked for a better mentor for my PhD.

Besides my advisor, I would like to thank the rest of my dissertation committee: **Dr. Salahuddin Ahmad, Dr. John Mintmire,** and **Dr. Daching Piao** for generously offering their time, support and guidance for the advancement of this work.

I wish to show my gratitude to **Dr. Mark Akselrod** and **AGFA** for providing the films. The project would not have been possible without them.

My sincere thanks to our collaborators **Dr. Salahuddin Ahmad** from Oklahoma University Health Sciences Center (OUHSC) and **Oliver Hanson** from St. John Hospital for giving us the opportunity to test the technique in clinical settings and offering valuable guidance. Our gratitude to the collaborators in Italy**, Lorenzo Placidi** and **Davide Cusumano** for their collaboration and guidance in testing the technique in magnetic fields.

I would like to acknowledge **Dr. Stephen Mckeever** for offering me assistantship and giving me the opportunity to work on exciting projects. I would like to thank **Dr. Sergey Sholom** for his support and always being available for discussions.

I would like to thank the Physics department staff, with special thanks to **Susan Cantrell** and **Tammy Austin**. You both have been very welcoming to me from the first day and helped me through any administrative issues during my PhD, which I am forever grateful for.

I cannot thank enough to my lab mates for making the lab a fun and learning environment. I was hoping to make new friends in the lab but with time we grew as a family. I could not have asked for a better group to work with. A special thanks to **Robin** for guiding me in the early stages of my PhD.

My thanks and appreciation to my friends and family. I would not have been able to get here without your love and support. A special thanks to my friends in Stillwater for their love and support throughout these years.

Acknowledgements reflect the views of the author and are not endorsed by committee members or Oklahoma State University

Name: NISHAN SHRESTHA

Date of Degree: May, 2020

Title of Study: FURTHER DEVELOPMENTS IN 2D OPTICALLY STIMULATED LUMINESCENCE DOSIMETRY BASED ON AL2O3 AND MGB4O7

Major Field: PHYSICS

Scope and Method of Study: The objective of this work is to explore potential improvements in 2D OSL dosimetry. These include the introduction of Tikhonov regularization in the pixel bleeding algorithm, which was investigated based both on simulated data as well as experimental results obtained using a 6 MV linear accelerator (linac) and an Accuray CyberKnife. The feasibility of using of Al_2O_3:C and Al_2O_3:C,Mg for its application in dosimetry in the presence of magnetic fields was tested. Finally, initial results of newly developed MgB_4O_7:Ce,Li films for 2D optically stimulated luminescence dosimetry are presented.

Findings and Conclusions: The results show that the implementation of Tikhonov regularization improves the image noise and resolves the directional dependence in the OSL images when compared to the Least Squares algorithm. The initial measurements of off-central ray ratios (OCR), output factors (OF's), and tissue phantom ratios (TPR) in CyberKnife shows good agreement with the measurements using the commercial stereotactic diode. The initial tests using the Al_2O_3 OSLD's in MR linac show that the detectors do not attenuate the beam, independent of angle of irradiation within 1.4%. The gamma analysis of IMRT treatment plans and the OSL images show a good passing rate for both 3% - 3 mm and 2% - 2 mm gamma criteria. The initial studies of MgB_4O_7:Ce,Li films demonstrate the possibility of 2D dosimetry for radiotherapy applications with many advantages over Al_2O_3:C or Al_2O_3:C,Mg films. MBO films show no pixel bleeding in the OSL images, has a linear dose response up to 10 Gy with steep dose gradients, has background equivalent dose of <0.5 mGy. However, it suffers from fading and sensitization. In conclusion, this work demonstrates OSL films have huge potential for its 2D dosimetry in both small fields and MR guided radiotherapy especially with development of new OSL materials to overcome the challenges with the current OSL materials.

TABLE OF CONTENTS

Chapter **Page**

Chapter **Page**

Chapter **Page**

LIST OF TABLES

LIST OF FIGURES

CHAPTER I

INTRODUCTION

The goal of radiotherapy is to treat cancer without health detriment to the patient which requires delivery of prescribed dose to the tumor while sparing healthy tissues. These two competing goals can be understood by looking at the dose dependence of the tumor control probability (TCP) and the normal tissue complication probability (NTCP). Ultimately one must maximize the TCP and minimize the NTCP. Therefore, it is important to accurately and precisely determine the dose delivered.

Advances in various radiation therapy modalities, such as intensity modulation radiotherapy (IMRT), volumetric modulated arc therapy (VMAT), and stereotactic radiosurgery (SRS), are continuously introducing new dosimetric challenges (Das et al., 2000; Haasbeek et al., 2012; Hall et al., 2013; Nutting et al., 2011; O'Brien et al., 2017). Due to superior dose conformity of these techniques, hypo-fractionated treatments are made possible (Thariat et al., 2013). This implies stricter dose and geometry requirements. According to the International Atomic Energy Agency (IAEA), the overall uncertainty of the radiotherapy process must be within 5% with dosimetric uncertainty of 2% or less at a confidence level of 95% (Gomez et al., 1973).

Small photon fields are increasingly used in IMRT and SRS treatments, which utilizes small fields with diameter in the range of 5 mm – 40 mm to deliver large radiation doses in a single fraction. Dosimetry of these small fields cannot be accomplished through traditional means due

to factors such as loss of charged particle equilibrium, partial occlusion of the source, and highdose gradient (Aspradakis et al., 2010). An ideal detector for small field dosimetry should have high spatial resolution with a small sensitive volume, have a wide dynamic range, and be independent from dose rate, energy, angle of irradiation and (Das et al., 2000; De Wagter, 2004). There are commercial detectors available for small field dosimetry, but discrepancies in the measurements between these detectors exist (Das et al., 2000). Ionization chambers response is affected by dose-volume averaging and break down of charged particle equilibrium (CPE) in small fields (Laub and Wong, 2003; Low et al., 2003; Wuerfel, 2013). Diodes are not water equivalent and therefore, over respond to low energy photons. In addition, most of the chambers and diodes are orientation dependent due to their large cavity length and require corrections based on Monte-Carlo simulations (Francescon et al., 2012; Francescon et al., 2014). Plastic scintillators require corrections for the Cherenkov radiation and are currently not available for scanning dose profiles.

Magnetic resonance guided radiotherapy (MRgRT) has become of great interest for cancer treatments, but the effect of magnetic field in detectors introduce additional challenges. MRgRT incorporates an MRI scanner with a radiotherapy source such as a linear accelerator or ^{60}Co source (Mutic and Dempsey, 2014). It provides real-time imaging during the patient treatment, reducing uncertainties in the patient positioning and target localization, potentially improving the precision of the therapy. Nevertheless, the Lorentz force alters the trajectory of the secondary electrons, which effects the detector response of ionization chambers (Meijsing et al., 2009; O'Brien et al., 2017; Reynolds et al., 2013). In addition to ionization chambers, other solid-state detectors like diamond detectors and plastic scintillation detectors also show variability as a function of the magnetic field (Reynolds et al., 2014; Stefanowicz et al., 2013). As for

radiochromic films (Gafchromic EBT3, Ashland Inc.), the magnetic field affects the crystal orientation and polymerization during irradiation with a decrease in response of the films by ~8.7%, 8.0% and 4.3% for the red, blue and green channels respectively (Reynoso et al., 2016).

Al_2O_3:C Optically Stimulated Luminescence detectors (OSLD) are of interest for medical dosimetry. They have high sensitivity to radiation (Akselrod and Kortov, 1990), linear dose response (Jursinic, 2007; Reft, 2009; Viamonte et al., 2008), wide dynamic dose range (Akselrod and McKeever, 1999), potential dosimetric precision of < 1% (Yukihara et al., 2005), minimal dark fading (Viamonte et al., 2008), low energy dependence of ±1% in MV X-ray beams (Viamonte et al., 2008), dose rate independent (Jursinic, 2007), and show small angular dependence for MV X-ray beam (Jursinic, 2007).

Al_2O_3:C,Mg on the other hand was originally developed for optical data storage and fluorescence nuclear track detectors for its radio photoluminescence properties (Akselrod, 2006; Sykora et al., 2007). There has not been a lot of studies regarding the OSL properties of the material compared to Al_2O_3: C. However, Al_2O_3:C,Mg has OSL properties similar to Al_2O_3:C with a higher concentration of F^+- centers, with luminescence lifetime <7 ns which makes it an excellent candidate for 2D OSL dosimetry (Denis et al., 2011a; Evans and Stapelbroek, 1978; Rodriguez et al., 2011).

Nevertheless, Al_2O_3:C Optically Stimulated Luminescence Detectors (OSLD) were until recently limited to point dosimetry. The slow luminescence of the F-center emission, the main luminescence center in this material, has prevented its use in 2D dosimetry using laser-scanning techniques, the imaging modality used in computed radiography. This situation has changed with the development of a correction algorithm for Al_2O_3 films (Yukihara and Ahmed, 2015), which opened the doors to the development of laser-scanning 2D dosimetry based on

dosimetric films of Al_2O_3:C or Al_2O_3:C,Mg (Ahmed et al., 2014; Ahmed et al., 2017). Initial results on 2D dosimetry using Al_2O_3 films shows that it has low background (~mGy), linear response, wide dynamic range (4-5 orders), good spatial resolution (~1mm), and potential dose uncertainty within 2% (Ahmed et al., 2014).

The OSL 2D dose maps obtained using Al_2O_3, however, suffer from an additional noise introduced by the pixel bleeding correction. This is due to the lack of regularization in the mathematical deconvolution analysis used to correct for the pixel bleeding (Yukihara and Ahmed, 2015). Thus, there is the potential to minimize the noise by implementing regularization algorithms such as the Tikhonov (Hansen, 1992b).

To address the limitations caused by the long luminescence lifetime of Al_2O_3, a new material has been developed for 2D dosimetry: MgB_4O_7:Ce,Li (MBO) (Gustafson et al., 2019; Yukihara et al., 2017). MBO has OSL intensity comparable to Al_2O_3:C, linear dose response from 0.1 – 100 Gy (Gustafson et al., 2019). In addition, Ce^{3+} emission has fast luminescence lifetime in order of tens of nanoseconds. In principle, this eliminates the need for pixel bleeding correction algorithm in laser scanning imaging. As opposed to the materials used in image plates such as BaFBr:Eu^{2+} (Z_{eff} = 49.0), MBO has low effective atomic number (Z_{eff} = 8.2).

The objective of this work is to explore potential improvements in 2D OSL dosimetry. These include the introduction of Tikhonov regularization in the pixel bleeding algorithm, which will be investigated based both on simulated data as well as experimental results obtained using a 6 MV linear accelerator (linac) and an Accuray CyberKnife. The feasibility of using of Al_2O_3:C and Al_2O_3:C,Mg for its application in dosimetry in the presence of magnetic fields was tested. Finally, initial results of newly developed MgB_4O_7:Ce,Li films for 2D optically stimulated luminescence dosimetry are presented.

This work is structured as follows. Chapter II discusses the challenges in radiotherapy dosimetry and currently available 2D dosimetry techniques along with their advantages and disadvantages. In addition, the basic OSL mechanism in Al_2O_3 and MBO is discussed along with current progress and challenges towards 2D dosimetry using OSL. Chapter III discusses the general experimental details of this study, including sample properties, irradiation sources, readout equipment, and data acquisition methodologies. The next four chapters focus on specific investigations. Chapter IV presents the studies regarding feasibility of Tikhonov regularization in pixel bleeding algorithm based on simulated data. Chapter V applies the algorithm to experimental data obtained in hospital setting using the 6 MV linac and the Accuray CyberKnife. It also includes results from initial tests on dosimetric performance of Al_2O_3:C,Mg films in small field dosimetry. Chapter VI demonstrates the application of Al_2O_3:C and Al_2O_3:C,Mg films for dosimetry in MRgRT and includes studies on the dose response, angle dependence in irradiation using both point detectors and films. In addition, gamma analysis results from IMRT treatment plans delivered to films are presented. Chapter VII presents feasibility studies of 2D OSL dosimetry using MgB_4O_7, including dose response, fading, re-usability, development of image reconstruction algorithm for MBO using 2D OSL system, and compares its response and other properties with Al_2O_3:C and Al_2O_3:C,Mg. Finally, conclusions and potential future developments are discussed in Chapter VIII.

CHAPTER II

BACKGROUND

In this chapter, the current challenges in dosimetry in radiotherapy are discussed. First, the literature is reviewed to summarize the current challenges in radiation therapy dosimetry. Then, commercially available 2D dosimetry techniques are discussed along with their advantages and disadvantages, as well as different OSL materials used in point dosimetry and in 2D dosimetry. Finally, context is given regarding the system and material corrections that are required for Al_2O_3 for its applications 2D dosimetry along with Tikhonov regularization technique to improve the noise in the OSL signal.

2.1 Challenges in radiation therapy dosimetry

2.1.1 Small field dosimetry

Advanced treatment modalities use small radiation beams in conjunction with real-time imaging to shrink the treatment margin around the target while increasing the dose delivered for greater biological effect (Kilby et al., 2010; Leksell, 1983). Treatments such as SRS, SBRT, and IMRT, which utilizes small fields for treatments, require high levels of precision in quality assurance (QA) and dosimetry since higher dose treatments pose greater potential risk for patients. Treatment field sizes less than 4×4 cm^2 are considered to be small fields and are inherently challenging for dosimetry (Aspradakis, 2009; Das et al., 2008).

The dosimetry in traditional radiation fields is accomplished by the application of cavity theory (Attix, 2008). The most important assumption of cavity theory is that at the location of the detector the number of charged particles entering the volumes is the same as those leaving the volume, which is called charged particle equilibrium (CPE). In small fields, the lateral range of electrons is larger than the field size which leads to a problem referred to in the literature as loss of lateral charged particle equilibrium. This in turn affects the shape of the beam profile and the absorbed dose on the central axis.

In addition, partial occlusion of the radiation source exacerbates the effect. This happens when the collimating output beam of the linac is similar or smaller than the source size as viewed from the detector. In this condition, only a portion of the source is seen by the dosimeter, which causes the detector to measure a lower output compared with larger field sizes, when the detector sees the whole source.

Figure 2-1 demonstrates the effects observed when decreasing the field size. For field sizes large enough to yield CPE and no occlusion of sources (Figure 2-1a), the full width half maximum (FWHM) of dose profiles are used to determine the field size as the field border will be ~50% of the dose level. As the physical collimation increases (i.e. field size decreases), the FWHM of the dose profiles decreases at a faster non-linear rate. This causes the field sizes to be measured larger than they are. Therefore, it is important to accurately measure and characterize the field size using detectors with high spatial resolution.

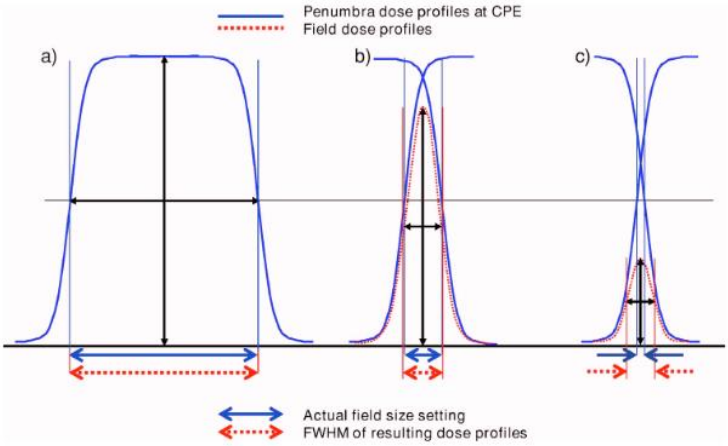

Figure 2-1. Profile widening associated with small fields. Reproduced from Das et al. (2008).

Another problem in small field dosimetry is the volume averaging effect. This occurs when the dosimeter dimension is relatively large compared to the radiation field. All detectors have a finite detection volume and measure the average signal over its given volume. In high gradient dose regions in small fields the dose value changes significantly over the detector's active volume. Thus, the measured signals are artificially lowered.

Figure 2-2 shows volume averaging effect using the dose profiles measured with 3 different ionization chambers: a micro chamber (Exradin A14, 0.009 cc), a farmer chamber (Exradin A12, 0.62 cc), and a PTW chamber (PTW-N31005, 0.125 cc). As can be seen, the dose profiles are artificially flattened with increasing detector volume.

Another problem associated with volume averaging effect is widening of penumbra, which is the width from 80%-20% of the max dose, an important parameter when measuring beam profiles (Low et al., 2003). Since accurate beam profiles are parameters required by the TPS, it is important to characterize them with high precision. Thus, small size detectors with high resolution are desired.

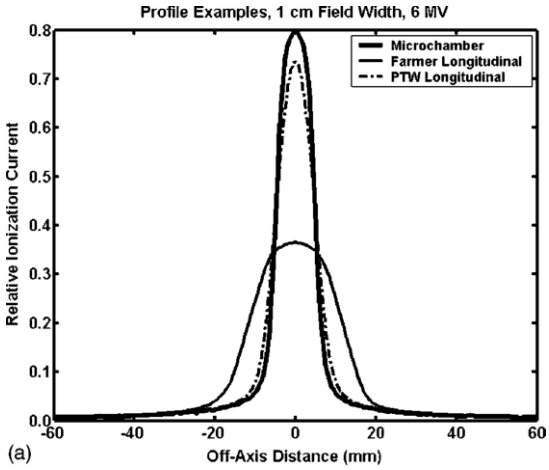

Figure 2-2. Volume averaging effect using dose profiles measured from three types of ionization chamber with different active detector volume. Reproduced from Low et al. (2003)

These inherent characteristics of small field dosimetry pose dosimetric challenges for commercially available dosimeters. Figure 2-3 shows the cone factors (output factors) of an SRS unit Clinac-600SR (Varian Medical Systems). As can be seen for cone size <20 mm there are discrepancies of >14 % between the detectors. In addition, Parwaie et al. (2018) reviewed commercially available dosimeters and concluded that currently no dosimeter has all properties required for dosimetry in small fields.

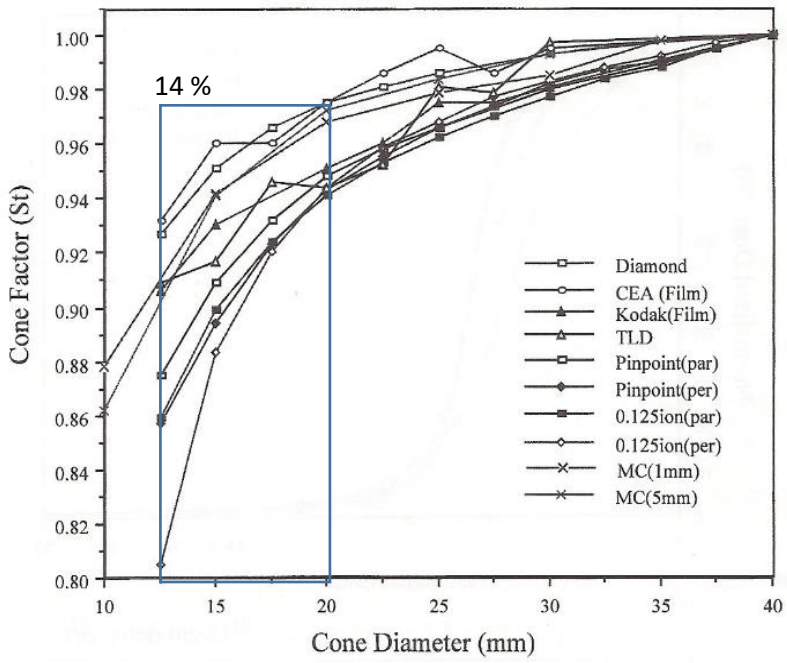

Figure 2-3. Dosimetric variation with different detectors. Reproduced from Das et al. (2000).

2.1.2 MRgRT

Recent developments towards real-time image guided radiotherapy hybrid devices have led to the combination of an MRI scanner with a radiotherapy unit, such as a linear accelerator or ^{60}Co source (Fallone et al., 2009; Jaffray et al., 2010; Mutic and Dempsey, 2014). There are currently four MRI linac designs with different magnetic field strength and two beam-magnetic-filed orientations, perpendicular (transverse) and parallel (inline) (Jelen and Begg, 2019). Table 2-1 shows the currently available MR-linac system along with their magnetic and radiation beam properties. In either configuration, the Lorentz force alters the trajectory of secondary electrons. In transverse configuration, the Lorentz force causes the electron paths to become curved, also called electron return effect (ERE), changing the direction and reducing the range. This causes increased dose deposition at tissue-air interface (Chen et al., 2016; Raaijmakers et al., 2005). In in-line configuration the Lorentz force causes electrons to spiral around the

magnetic field direction causing loss of energy in collisions. These effects change the response of radiation detectors as it depends on paths of electrons traversing their active volume.

Table 2-1. Properties of current MRI-linac systems. Reproduced from Jelen and Begg (2019).

System (vendor)	Magnet properties			Orientation	Radiation beam properties		
	Type	Strength	Opening		Energy	SID	Field size / leaf width
MRIdian (Viewray) [7]	split, super-conducting	0.35 T	70 cm bore	perpendicular	6 MV	0.9 m	27.4×24.1 cm / 4.15 mm
Aurora-RT (MagnetTx) [10,11]	biplanar, high temp. super-conducting	0.5 T	110 (W) × 60 (H) cm	parallel (perpen-dicular possible)	6 MV	1.22 m	30 cm / 5 mm
Australian MRI-linac	open, super-conducting	1.0 T	62 cm bore, 50 cm gap	parallel (perpen-dicular possible)	4 & 6 MV	1.9–3.3 m	30–50 cm / 9.5–16.5 mm
Unity (Elekta) [9,12]	closed, super-conducting	1.5 T	70 cm bore	perpendicular	6 MV	1.435 m	22×57.4 cm / 7.2 mm

SID – source-to-isocentre

It was found both experimentally and using Monte-Carlo simulations that the response of ionization chamber changes by ~1-2% in in-line setting, and up to 10% in transverse magnetic fields, depending on the orientation of the magnetic fields (Meijsing et al., 2009; Reynolds et al., 2013, 2015). Plastic scintillation detectors, even though non-magnetic, were found to show unexplained 7% increase in response in presence of magnetic field (Stefanowicz et al., 2013). As for radiochromic films (Gafchromic EBT3, Ashland Inc.), the magnetic field effects the crystal orientation and polymerization during irradiation causing a decrease in response of the films by ~8.7%, 8.0% and 4.3% for the red, blue and green channels respectively (Reynoso et al., 2016).

Luminescence detectors are considered promising candidate for dosimetry in magnetic fields (Jelen and Begg, 2019). TLDs were found to show no field dependence in a 1.5 T transverse field. In addition, Spindeldreier et al. (2017) observed relatively small decrease in response of Al_2O_3 detectors with increasing magnetic field (-1.3%/T) and no angular dependence.

2.2 2D dosimetry techniques

To measure dose or relative dose distribution in the entire plane, commercial two-dimensional (2D) detectors or films are used. They are widely used in radiotherapy as part of the beam commissioning and QA requirements of IMRT and virtual wedge profile measurements (Ezzell et al., 2009; Klein et al., 2009).

The most widely used films for IMRT dosimetry are radiochromic films. They have high spatial resolution (< 25 μm), which is an advantage for 2D dosimetry. They are self-developing and near tissue equivalent, and widely used for commissioning for patient-specific IMRT and Stereotactic Body Radiation Therapy (SBRT) treatment verifications (Borca et al., 2013; Palmer et al., 2015). Radiochromic films also have some inherent limitations, such as non-linear dose response (Borca et al., 2013), high background (Micke et al., 2011), and narrow dynamic range, with useful dose range only up to 10 Gy (Devic, 2011). In addition, due to its complicated calibration protocol, they are not commonly used for absolute dosimetry.

Diode arrays and ionization chamber arrays have also been used for pre-treatment dosimetry of modulated fields (Létourneau et al., 2004; Poppe et al., 2006). They both have excellent linearity, and reproducibility, but suffer from poor spatial resolution due to the larger separation between detectors and large individual detector size. Diode arrays have angular dependence and field size dependence (Jin et al., 2014). In addition, the ionization chambers suffers from volume averaging effects resulting in field size dependence (Das et al., 2008).

OSL detectors are of interest for 2D dosimetry due to its wide dynamic range, low background, and good spatial resolution (Ahmed et al., 2014; Jahn et al., 2010). Al_2O_3:C and Al_2O_3:C,Mg OSL films have shown the potential to be used in dose verification. They are energy independent, have low background (~mGy), linear response, wide dynamic range (4-5 orders),

good spatial resolution (~1mm), are field size-independent, and offer potentially an overall dose uncertainty within 2% (Ahmed et al., 2014; Ahmed et al., 2017). As mentioned before, Spindeldreier et al. (2017) showed that OSLDs exhibit no angular dependence with the magnetic field and, with proper calibration, it should be suitable for QA in MR-guided radiotherapy devices.

2.3 Optically Stimulated Luminescence

Optically Stimulated Luminescence (OSL) is the luminescence emitted from an irradiated insulator or semiconductor during exposure to light (Bøtter-Jensen et al., 2003).

OSL materials contain defects in the crystalline lattice, introduced intentionally during crystal growth or unintentionally by contaminants. These defects can be missing ions, ions in interstitial position, and extrinsic ions in the lattice points substituting for the original ions of the crystal, and so on. The defects can introduce energy levels within the bandgap of the material: energy levels close to the conduction bands can trap electrons, whereas energy levels close to the valence band can trap holes. Energy levels close to the Fermi level can capture a hole from the valence band and an electron from the conduction band, acting as a recombination center

Figure 2-4 illustrates the OSL process of a crystal with one electron trap and one-hole trap. During exposure to ionization radiation, electrons are excited to the conduction band leaving behind a hole in the valence band. These electrons and holes are free to move in the bands and have a probability to get trapped in the lattice defects (Figure 2-4a). After irradiation, in the absence of optical or thermal stimulation, the trapped charges can remain trapped over geological times, depending on the depth of the traps, i.e., the difference in energy between the trapping level and the delocalized energy bands (Figure 2-4b). Once exposed to stimulation light source of proper wavelength, the trapped electrons can be stimulated to the conduction band.

In the conduction band, the electron is free to recombine with the trapped holes, leaving the luminescence centers in excited state. The excited luminescence center then relaxes to ground state by emission of the photon, which is called OSL (Figure 2-4c).

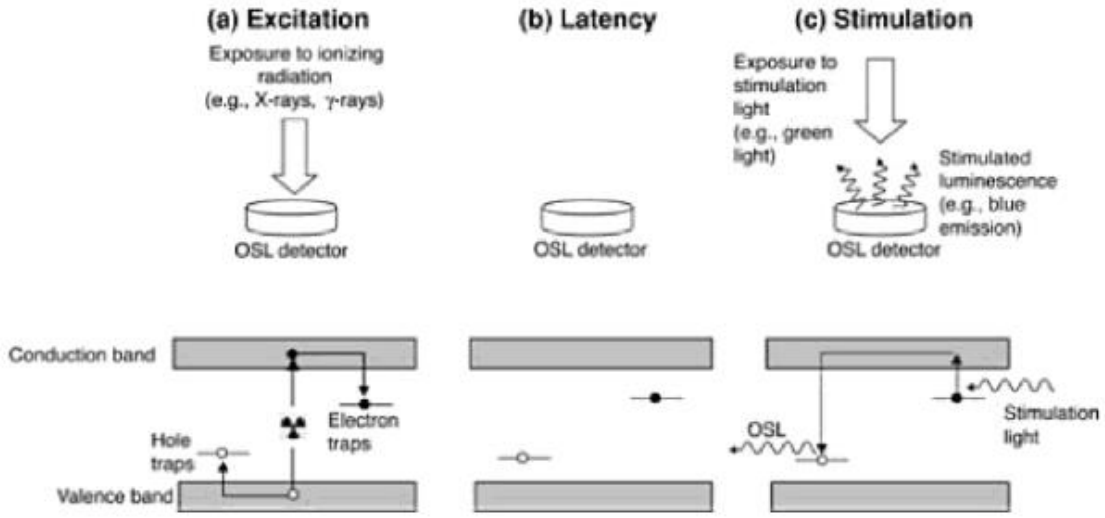

Figure 2-4. Stages in OSL process: (a) Irradiation of OSLD resulting in capture of electrons and holes in electron traps and hole traps respectively, (b) latency period of trapped charges in metastable state unexposed to heat/light and (c) stimulation using light source resulting in electron-hole recombination, emitting OSL. Reproduced from Yukihara and McKeever (2011).

In a simple one trap one, recombination (OTOR) model, the optical transition probability p of an electron escaping from a trapping center is directly proportional to incident photon flux ϕ and the photoionization cross section σ of the trapping center.

$$p = \sigma \Phi \qquad \textbf{(2-1)}$$

If there are *n* trapped electrons, the rate of release of the electrons from the traps is *np.*

$$\frac{dn}{dt} = -np \qquad \textbf{(2-2)}$$

The differential equation can be solved, which shows that the number of trapped electron decays with a first order exponential,

$$n(t) = n_0 e^{-pt} \quad \textbf{(2-3)}$$

where, n_0 is the initial number of trapped charges.

Assuming the light intensity is proportional to the rate of electrons escaping the trapping centers the OSL intensity can be written as:

$$I_{OSL} \alpha \left|\frac{dn}{dt}\right| = n_0 p e^{-pt} \quad \textbf{(2-4)}$$

Some of the key benefits of the OSL technique in dosimetry are: (i) OSLDs can be re-read, as a short stimulation is sufficient for OSL dosimetry (Akselrod and McKeever, 1999; Jursinic, 2007); (ii) OSL has no confounding signals, as the OSL is typically monitored at wavelengths shorter than the wavelength of stimulation light, which is beneficial for low dose measurements (Yukihara and McKeever, 2011); (iii) OSLDs can be read using multiple techniques (CW-OSL, POSL, LM-OSL) based on application needs (Akselrod et al., 2006), and it can be read out fast, as measurements can be as short as milliseconds.

2.4 2D dosimetry using OSL

In spite of the excellent properties of Al_2O_3, its application in radiotherapy was limited to point dosimetry until recently. This is because the F-center emission in this material has a long luminescence lifetime, preventing its use in 2D dosimetry using laser-scanning techniques. With the development of the pixel bleeding correction algorithm, the potential of using Al_2O_3 OSLDs in 2D dosimetry have been studied by Ahmed et al. (2014).

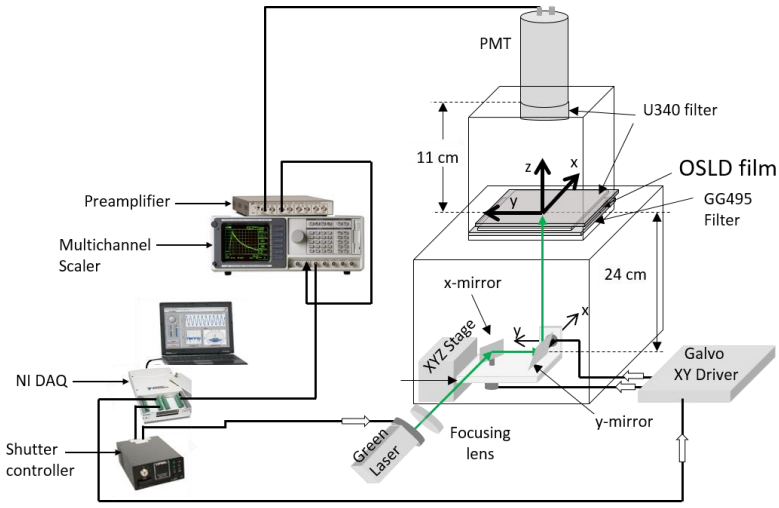

Figure 2-5. Schematics of the 2D OSL laser scanning dosimetry system. Reproduced from Ahmed et al. (2014).

A 2D laser scanning dosimetry system was developed based on newly developed Al_2O_3 films (Figure 2-5). The system incorporates a green laser and a 2D galvo-mirror system that reflects the laser to the film. The mirror moves the laser such that the laser scans the film in alternating directions. The luminescence signal emitted is collected by the PMT placed at the center of the system. The recorded PMT signal is amplified and digitized using a multichannel scaler. Then, the data obtained is processed through an algorithm that includes system and material corrections. The system corrections include the pixel shift correction due to galvo hysteresis, galvo distortion correction due to geometric distortion of the optical system, and PMT light collection efficiency correction. The material corrections include the phosphorescence correction and the pixel bleeding correction.

The dosimetric performance of the system and the film were tested using therapeutic photon beam and pencil heavy ion beams in clinical settings. The results obtained were also compared with commercial radiochromic films (Gafchromic EBT3, Ashland Inc.), analyzed using

the triple channel method (Micke et al., 2011). It was found that the OSL films were homogenous within experimental uncertainty and the OSL film response do not saturate until 75 Gy. The OSL signal from an un-irradiated film is equivalent to <0.5 mGy and therefore, no background subtraction is needed. This eliminates the need for scanning the same film before and after irradiation. The minimum detectable dose (MDD) of the OSL films is <1 mGy with the dynamic range spans 5 orders of magnitude. The OSL films were able to perform dosimetry with a precision of 1-2% with spatial resolution of 2-line pairs/mm.

Nevertheless, some issues have been identified with the 2D OSL dosimetry system. There is background signal before the laser hits the irradiated film which scales with the maximum film signal. This is probably due to OSL from the entire detector, stimulated by scattered laser light which increases as the laser approaches the detector. Nevertheless, this signal is less than 1% of the maximum OSL signal for any dose and can possibly be minimized using light absorbent materials around the galvo mirror.

In addition, the pixel bleeding correction algorithm introduces additional noise in the x-axis without perturbing the signal along the sub-scan direction (y-axis) (Figure 2-6). This leads to a directional dependence in the dose uncertainty. This additional noise is due to the pixel bleeding correction algorithm, which is based on a Least Squares deconvolution algorithm without any regularization (Yukihara et al., 2015). This problem, however, can potentially be reduced by introducing a regularization procedure in the pixel bleeding algorithm. This can remove not only the directional dependence of the image noise, but also improve the overall signal-to-noise ratio (SNR) in the image.

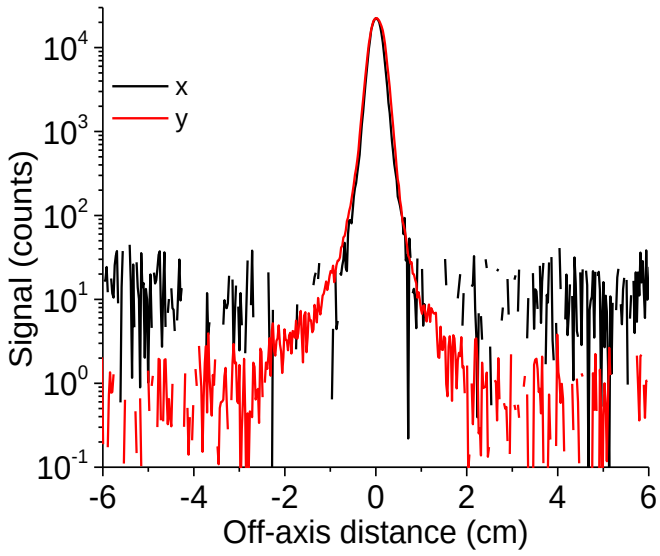

Figure 2-6. Reconstructed signal profiles (average of four rows spanning 1 mm) for Al_2O_3:C film irradiated with a 430 MeV ^{12}C pencil beam with 3.4 mm FWHM. Reproduced from Ahmed (2016).

2.5 A brief review of OSL materials and their suitability for 2D dosimetry

2.5.1 BaFBr:Eu^{2+}

BaFBr:Eu^{2+} phosphor storage plates widely used in computed radiography have been investigated for 2D dosimetry in radiotherapy. One main advantage of image plates as a 2D dosimeter is that it can be used for both imaging and dosimetry. In addition, it has some important features making it a promising candidate for 2D dosimetry. Crijns et al. (2017) showed that it has a linear dose response up to 32 Gy, < 2.6% non-uniformity, and that it can be reused and read out immediately. However, it has high effective Z_{eff} of ~49, high signal fading (>50 % in 36 h), and large energy dependence (over response <100 keV), which makes it difficult to use for precise medical dosimetry (Ariga et al., 2007; Rowlands, 2002).

2.5.2 Other materials investigated for 2D dosimetry

There are other additional OSL materials investigated for 2D dosimetry. BeO has been investigated for 2D dosimetry due to its effective atomic number (Z_{eff} = 7.14), which is close to tissue, and sensitivity comparable to Al_2O_3:C. It has a linear dose response from 5 mGy – 10 Gy, with a spatial resolution of ~1 mm (Jahn et al., 2010). The material also has a fast luminescence lifetime of ~27 μs which is advantageous for 2D dosimetry (Yukihara, 2011). However, the toxicity of BeO in powder form hinders the production of OSL films and, therefore, not much additional work has been done for 2D dosimetry applications, except for the use of BeO ceramic plates.

KCl:Eu^{2+} is another potential candidate for 2D dosimetry. It is dose rate-independent (< 2%), reusable up to 100 times (2 Gy per use), has low fading of 0.1%/h after the first 12 h, is energy independent, and has relatively low effective atomic number (Z_{eff} ~ 18) compared to BaFBr:Eu^{2+}. However, it has a superlinear response and significant fading at least up to 12 h post irradiation, which may be some reasons for it not being used in 2D dosimetry (Han et al., 2009).

Other materials investigated for 2D dosimetry include $NaMgF_3$:Eu,Li (Schuyt and Williams, 2019), LiSrS:Ce,Sm (Idri et al., 2004), and MgO:Nd,Li (Oliveira et al., 2013). Table 2-2 shows some dosimetric characteristics of some additional materials, some of which investigated for 2D dosimetry. As can be seen most of these OSL materials have good linear response and wide dynamic range, but the main disadvantage with some of these materials is their high Z_{eff} and fading.

Table 2-2. Some dosimetric characteristics of OSL materials. Reproduced from Pradhan et al. (2008)

OSL material [Ref]	*Rel. OSL Sensitivity*	*Linear dose range wavelength range/ peak (nm)*	*Stimulation wavelength (nm)*	*Main emission wavelength (nm)*	*Fading rate*	*Z Eff; (Tissue =7.4)*
$Al_2O_3:C$[12]	1.00	μGy-10Gy	450-550	~420	<5% /y	11.3
BeO[36]	~1.00	μGy-10Gy	~ 435	~335	6% in 1st 10 h and then nil	7.2
MgO:Tb[40]	~1.00	100μGy- 10Gy	500-560	375, 420, 440, 470, 500, 650	43% in 1st 36 h and then nil	10.8
$NaMgF_3:Eu$[44]	~10.0	μGy -100Gy	~ 470	360	40% in 1st 24 h and then nil	10.4
$KMgF_3:Ce$[42,43]	~10.0	1μGy- 10Gy	~ 470	~360	High and ^{40}K Self-irradiation.	14.7
$Li_2Al_2O_4:Tb$[41]	~0.01	200μGy- 10Gy	<532	370, 420 and 440	50% in 1st 50 h	9.74
$Mg_2SiO_4:Tb$[41]	~0.11	30μGy- 10Gy	<532	370, 420 and 440	30% in 1st 10 h and then 0	11.23
$Mg_2SiO_4:Tb,Co$[41]	~0.08	40μGy- 10Gy	<532	370, 420 and 440	30% in 1st 10 h and then nil	11.23
KCl:Eu[46,47]	~1.00	100μGy- 10Gy	500-560	350-480 and 560-700	High and ^{40}K Self-irradiation	18.1
KBr:Eu[47]	~1.00	100μGy- 10Gy	500-560	350-480 and 560-700	High and ^{40}K Self-irradiation	31.76
$(NH_4)_2SiF_6:Tl$[45]	~0.02	> few mGy	470	300-370	80% in 1st 10 h	10.31
$Y_3Al_5O_{12}:Ce$[49]	~0.10	10mGy- 100Gy	500-560	350-480 and 560-700	Negligible in 2 months	33.81

2.5.3 $Al_2O_3:C$

The crystal structure of α-Al_2O_3 can be seen in Figure 2-7a. It consists of a hexagonal close packed array with O^{2-} sub-lattice with Al^{3+} ions occupying two out of every three interstitial sites in the lattice so that the charge neutrality is satisfied. Figure 2-7b shows F^+ center containing one electron and formed as charge compensators to C^{2+} impurities that have supplanted Al^{3+} ions during the crystal growth process.

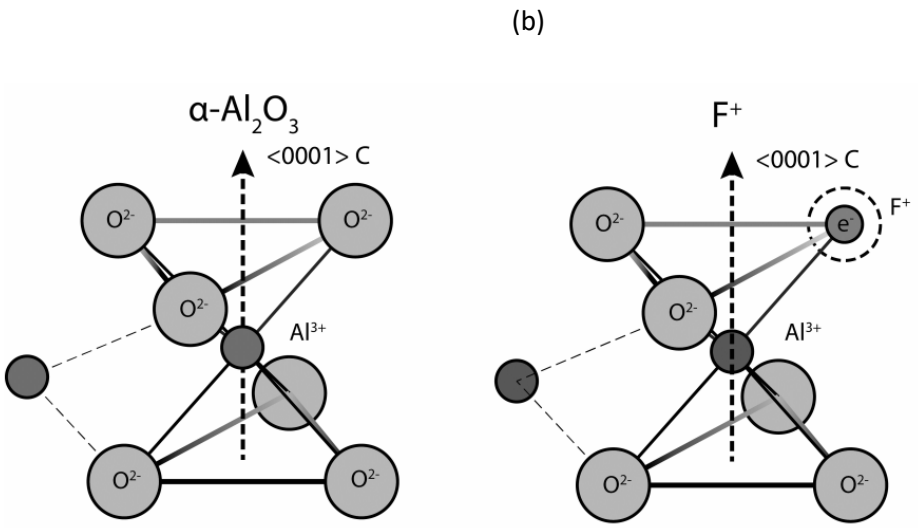

Figure 2-7. Lattice structure of α-Al_2O_3 and a single oxygen vacancy with one electron – F^+ center Reproduced from Kouwenberg (2018).

Al_2O_3:C is the most common OSL material and has been used worldwide since the late 1990s, although the material was originally developed as a thermoluminescence detector (Akselrod et al., 1990). Al_2O_3:C crystals have a high concentrations of oxygen vacancies (Akselrod and Kortov, 1990). An oxygen vacancy that captures two electrons form a defect known as F-centers, and when it captures one electron the defects are known as F^+-centers. These two color centers are responsible for the production of TL and OSL.

The F-center's absorption band is centered at 6.0 eV (205 nm) and the associated luminescence band is centered at about 3.0 eV (450 nm). Figure 2-8 shows an energy band diagram with the absorption and emission transitions for the F- and F^+-centers in Al_2O_3. The F-center absorption band is due to the electron transition from ^1S ground state to ^1P state with absorption of 205 nm (6.1 eV) light. During relaxation, the electrons transitions non-radiatively from the ^3P to the ^1S ground state. The lifetime of this emission was found to be 35 ms (Lee and Crawford Jr, 1977). The absorption bands centered at about 4.8 eV (255 nm), 5.4 eV (230 nm), and 6.0 eV (205 nm) that overlaps with F-center absorption, are associated with F^+-center

absorption. These transitions are from 1A ground state to 1B, 2A, and 2B respectively. The main emission center is associated with the transition from 1B to 1A ground state with the emission of 3.8 eV (326 nm). This emission is associated with a lifetime of < 7 ns (Evans and Stapelbroek, 1978).

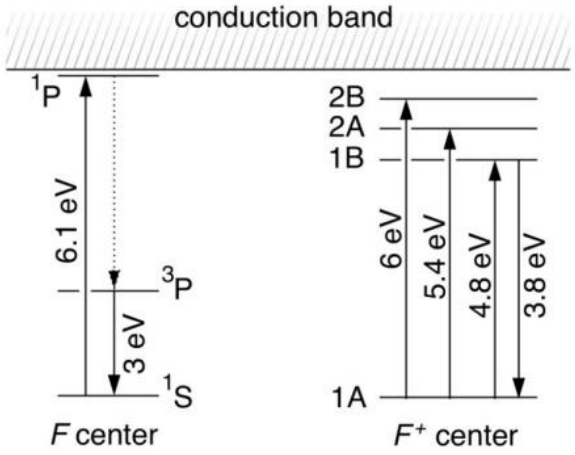

Figure 2-8. Energy level diagram for the absorption and emission processes of F and F^+ center. Dotted lines indicate non-radiative transition. Reproduced from Lee and Crawford Jr (1977).

Al_2O_3:C contains higher concentrations of F-centers than of F^+-centers (Akselrod et al., 1990). The concentration of these two centers, however, have a reciprocal relationship. When an F-center loses an electron or captures a hole, it converts to an F^+-center. Electrons may recombine with F^+-centers, converting it back into an F-center, with emission of 420 nm, as shown in Eq. (2-5) and (2-6).

$$F^+ + e^- \rightarrow F^* \rightarrow F + h\nu_{420\,nm} \quad \textbf{(2-5)}$$

$$F + h^+ \rightarrow F^+ \quad \textbf{(2-6)}$$

Since the two centers have different lifetimes, time resolved techniques are used to separate the two components. Figure 2-9a shows the time resolved OSL (TR-OSL) measurements of Al_2O_3:C (Yukihara and McKeever, 2006). It shows that during laser pulses the two emissions

are centered at ~335 nm (F^+ center) and ~420 nm (F-center). Figure 2-9b shows the OSL decay curves in the time resolved OSL measurements measured by Denis et al. (2011b).

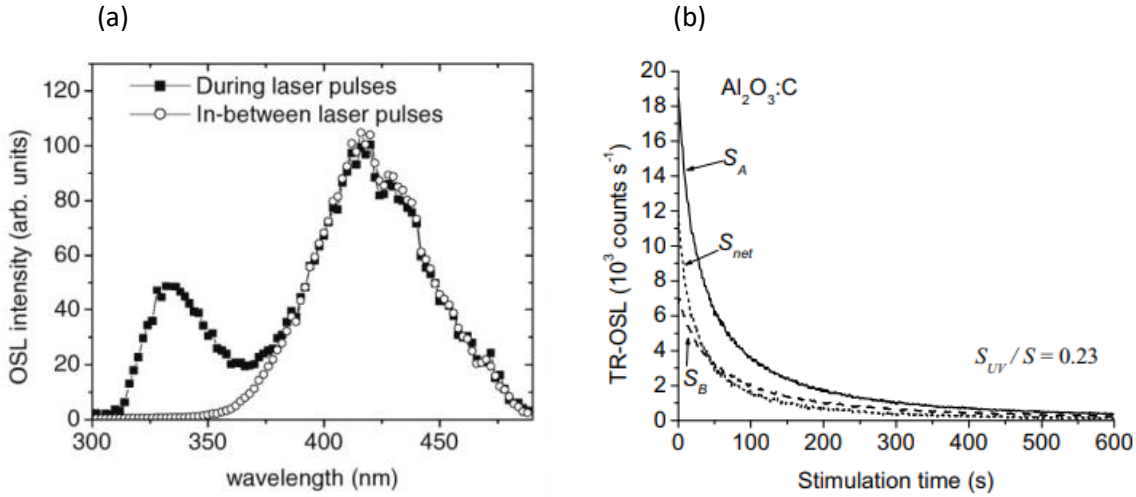

Figure 2-9. (a) Emission spectrum of Al_2O_3:C during and in between laser pulses. (b) TR-OSL decay curves of Al_2O_3:C. Reproduced from Denis et al. (2011) and Yukihara and McKeever (2006).

2.5.4 Al_2O_3:C,Mg

Al_2O_3:C,Mg crystals have much more complex defects created during the crystal growth with the introduction of Mg as a dopant. This results in multiple types of color centers with different absorption and emission bands. In addition to single oxygen vacancy defects, F and F^+ centers present in Al_2O_3:C crystals, new double oxygen vacancies give rise to new F_2 type centers (F_2^{2+} and F_2^+) associated with Mg-purity ions (Figure 2-10). The green coloration of the Al_2O_3:C,Mg crystals are due to a blue (435 nm) absorption band, which is attributed to the F_2^{2+} center (Akselrod et al., 2003). Even though this material was originally developed for optical data storage and fluorescence nuclear track detectors, and for its radiophotoluminescence properties, it is also useful for OSL, especially for 2D dosimetry.

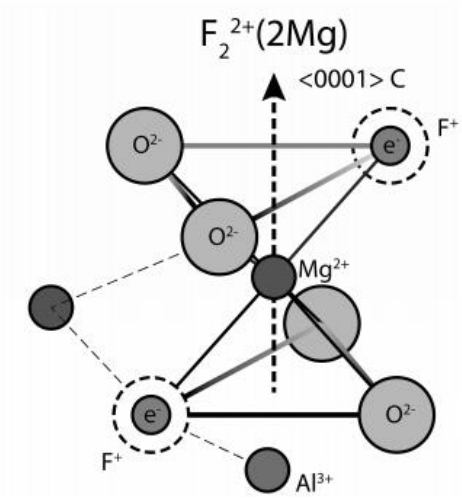

Figure 2-10. Lattice structure of Al_2O_3:C,Mg with two oxygen vacancies charge compensated by two Mg^{2+} ions. Reproduced from Kouwenberg (2018).

Al_2O_3:C,Mg has higher concentration of F- and F^+-centers than Al_2O_3:C, which can be seen by comparing the optical absorption spectra of Al_2O_3:C and Al_2O_3:C,Mg single crystals produced (Akselrod et al., 2003).

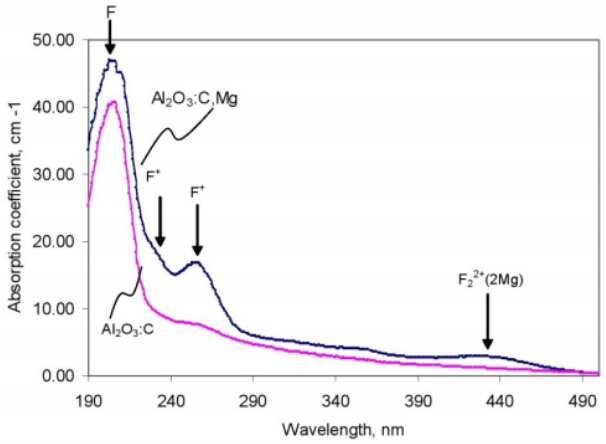

Figure 2-11. Optical absorption spectra of Al_2O_3:C and Al_2O_3:C, Mg single crystals, showing the high concentration of F-centers in Al_2O_3:C and the high concentration of F- and F^+-centers in Al_2O_3:C,Mg. Reproduced from Akselrod et al. (2003).

The spectral analysis of the OSL emission from Al_2O_3:C and Al_2O_3:C,Mg crystals indicated a higher F^+-center OSL emission, as shown in Figure 2-12a (Denis et al., 2011b). In addition, the time resolved OSL measurements showed that the ratio between the F^+-center OSL emission and the total OSL emission is higher in Al_2O_3:C,Mg than in Al_2O_3:C (Section 2.5.3). This is important for 2D dosimetry, because the higher the ratio of F^+- to F-center emission, the smaller the amount of pixel bleeding correction needed, leading to better image SNR.

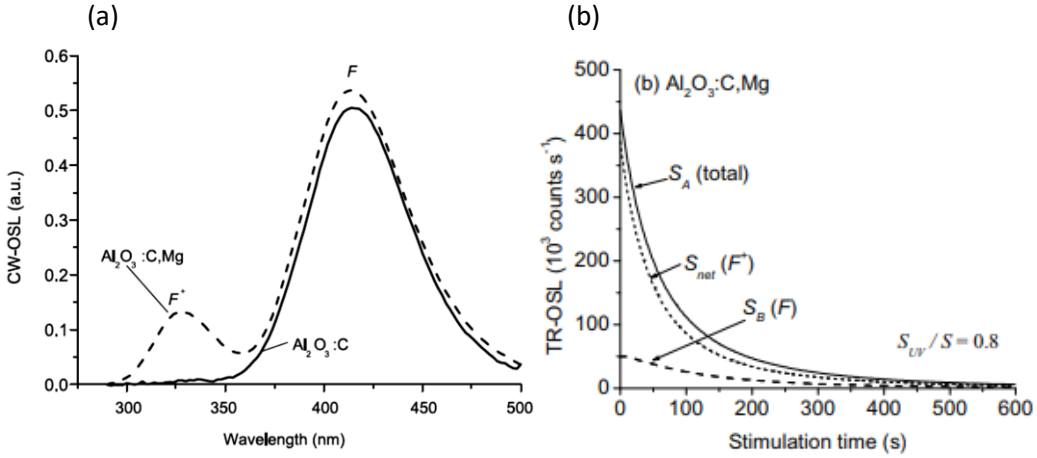

Figure 2-12. (a) CW-OSL emission spectra and (b) OSL decay curves of Al_2O_3:C and Al_2O_3:C,Mg single crystals. Reproduced from Denis et al. (2011b).

2.5.5 MgB_4O_7:Ce,Li

MgB_4O_7 (MBO) doped with Dy/Tm has been used as a TL material for nearly 40 years (Prokić, 1980).The TL material was found to be suitable for dosimetry as it is about 15 times more sensitive than LiF:Mg,Ti, has a low effective atomic number (Z_{eff} = 8.2), and is suitable for neutron dosimetry due to its boron content. Nevertheless, OSL dosimetry using MBO doped with Ce and Li has only recently been reported (Souza et al., 2017; Souza et al., 2019; Yukihara et al., 2017).

There have been recent improvements in the OSL properties of MBO (Gustafson et al., 2019). The new material synthesized with high purity reagents removes the competing recombination at Mn^{2+} emission (~580 nm), resulting in increased emission from Ce^{3+} centers (Gustafson et al., 2019). It has sensitivity comparable to that of Al_2O_3:C and linear dose response from 0.1 – 100 Gy. In addition, Ce^{3+} emission has fast luminescence lifetime (31.5 ns), making it a suitable candidate for 2D dosimetry using laser scanning.

Ce^{3+} is the main emission center in MBO and has emission in the UV region, being therefore suitable for OSL dosimetry with blue or green stimulation. Figure 2-13 shows the photoluminescence emission (PL) and excitation (PLE) spectra of MBO (Gustafson et al., 2019). There are three excitation bands observed at ~270 nm, ~ 293 nm and ~ 320 nm and the two emission bands are seen at ~ 340 nm and ~ 363 nm.

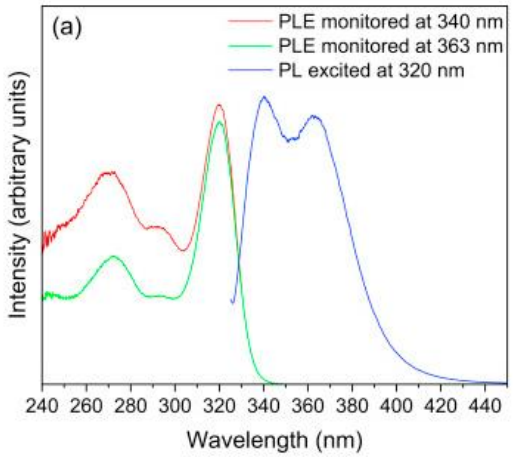

Figure 2-13. PL and PLE spectra of MBO. Reproduced from Gustafson et al. (2019).

2.6 Image corrections needed in 2D OSL dosimetry

2D dosimetry using Al_2O_3 requires series of corrections. The image reconstruction algorithm developed for Al_2O_3 is shown in Figure 2-14. The information required to correct for

each step is shown in the chart as well. The steps highlighted in blue are related to 2D OSL system and those in orange are related to intrinsic material properties.

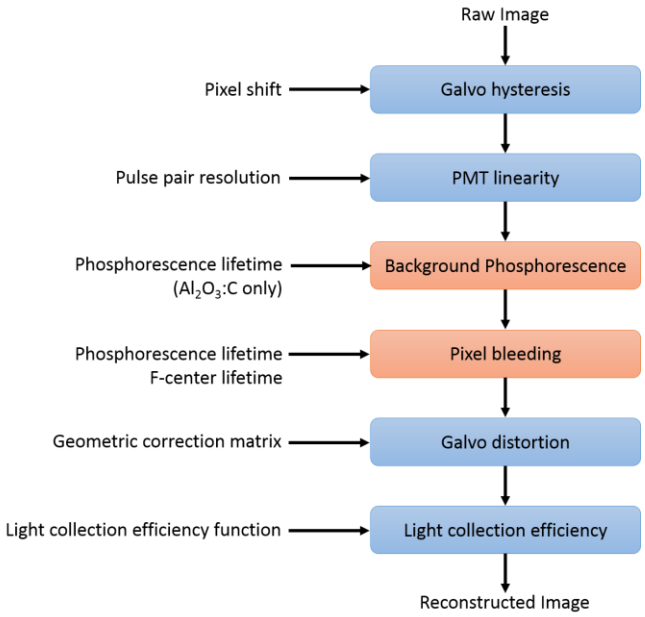

Figure 2-14. Flowchart represents the image reconstruction algorithm for Al_2O_3 films. The main input information required for each step of the correction is shown in the left column of the chart. The steps indicated in blue are related to system design and those in orange are related to intrinsic material properties. Reproduced from Ahmed et al. (2016).

Figure 2-15a shows a raw image from a 10 cm × 10 cm Al_2O_3:C film irradiated using a 6 MV linac (Section 3.5.2) with a total dose of ~20 Gy. Figure 2-15b-c shows the signal profiles from alternate scans at the center of the raw image in x and y direction along with the image corrections required. Individual corrections are briefly explained in the section below, but the full correction itself is explained in detail in Ahmed et al. (2016).

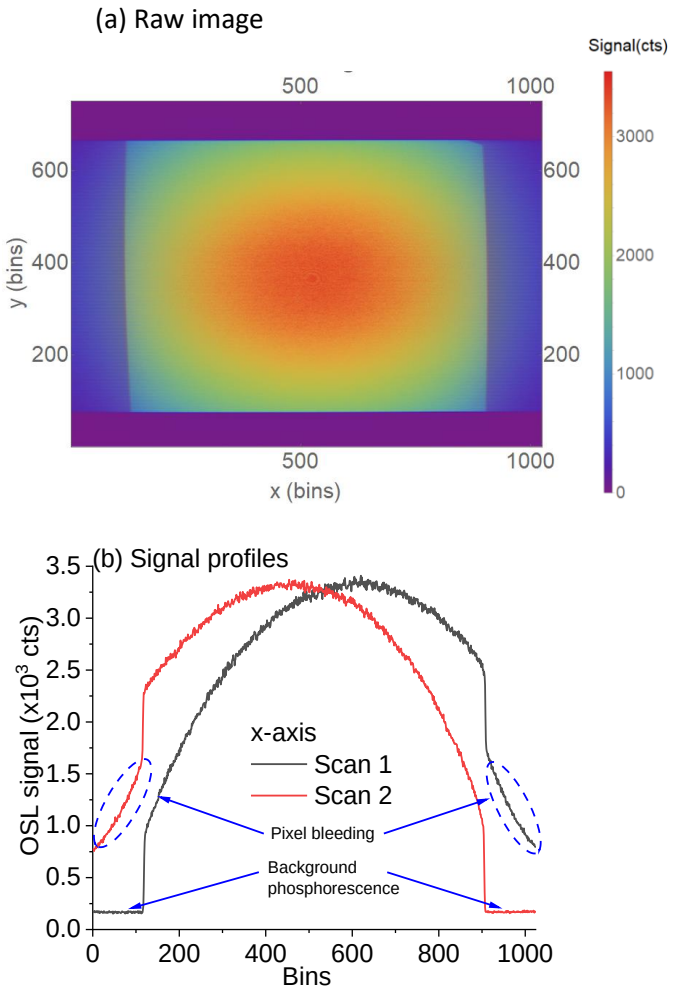

Figure 2-15. (a) Raw image of a 10 cm × 10 cm Al_2O_3:C film irradiated using 6 MV linac with a total dose of ~10 Gy. (b) Signal profiles from alternate scans at the center of the raw image in x direction showing the image corrections required.

Galvo hysteresis

In order to obtain the image, the OSL reader scans the consecutive rows of the film in alternating directions along the x-axis. As a result, at the edge of the detector, a pixel shift is observed between adjacent rows. This is due to galvo hysteresis, the mechanical lag in the galvo system when the motion is reversed, or desynchronization between the galvo and the photon counter.

PMT linearity

The counting rate affects the PMT counting efficiency. When the count rates are high, the signal pulses overlap decreasing the counting efficiency. The counting efficiency at high-count rate can also be limited by the counting system in discriminating overlapping pulses. If the oncoming pulses are not separated by a threshold time difference, known as pulse-pair resolution or dead time, the PMT shows nonlinearity.

Background phosphorescence

Background phosphorescence is the signal present in the OSL image before the laser hits the film. It is originated from the slow phosphorescence of previously scanned rows. This contribution can be corrected by analyzing the signal measured at the beginning of each row, where there is no film present and subtract it from the total OSL signal.

Galvo distortion

The *x*, *y* laser positions in the screen are not linearly related to the mirror angles (Xie et al., 2005) which leads to images with pillow-shaped geometrical distortion, even if the mirrors are perfectly aligned (Cui et al., 2009; Duma et al., 2009; Manakov et al., 2011).

Position dependence of the light collection efficiency

The PMT is fixed at center with respect to the film, thus, the light collection efficiency is position dependent. The signal at the center of the film is larger than the corners and decreases radially between the position in the film and the *z*-axis.

Pixel bleeding algorithm

The pixel bleeding algorithm relies on a model for the luminescence signal from the OSL film with laser scanning.

As explained by Yukihara and Ahmed (2015) the rate of change of concentration of the luminescence centers in the excited state, $m(t)$ is given by,

$$\frac{dm(t)}{dt} = p\, n(t) - \frac{m(t)}{\tau} \qquad \textbf{(2-7)}$$

The term *n(t),* is the rate of excitation with *p* the trapping probability and *n(t)* representing the concentration of trapped charge. $\tau^{-1}m(t)$ is the rate of de-excitation of the luminescence centers, where τ is the lifetime of the excited state. The luminescence intensity is directly proportional to the rate of decay of the luminescence centers and thus, proportional to $\tau^{-1}m(t)$. Assuming the concentration of the trapped charges to be constant $n(t) \cong n_0$ thus,

$$I(t) \propto \tau^{-1}m(t) = p\, n_0\left(1 - e^{-t/\tau}\right) \qquad \textbf{(2-8)}$$

After stimulation period Δt, the OSL signal decays exponentially with a lifetime τ as:

$$I(t) = p\, n_0\left(1 - e^{-\Delta t/\tau}\right)e^{-(t-\Delta t)/\tau} \qquad \textbf{(2-9)}$$

Due to the difference in the lifetime of the two luminescence centers, the fast center decays but the slow center keeps contributing to the next pixels. Thus, the light collected by any pixel at any given bin *i*, can be obtained by integrating Eq. (2-8) and (2-9),

$$g_i = \begin{cases} 0, & i < 1 \\ \Delta t - \tau(1 - e^{-\Delta t/\tau}), & i = 1 \\ \tau\, e^{-i\frac{\Delta t}{\tau}}\left(e^{\Delta t/\tau} - 1\right)^2, & i > 1 \end{cases} \qquad \textbf{(2-10)}$$

If the ratio between the contribution of the F and F^+-center is considered to be $R = S_F/S_{F+}$, Eq. (2-10) can be written as,

$$g_i = \begin{cases} 0, & i < 1 \\ (1-R) + R\,[\Delta t - \tau\left(1 - e^{-\Delta t/\tau}\right)], & i = 1 \\ R\,\tau\, e^{-i\Delta t/\tau}(e^{\Delta t/\tau} - 1)^2, & i > 1 \end{cases} \quad \textbf{(2-11)}$$

For deconvolution, using a Least Squares fitting, the signal can be written as,

$$y = X.a \quad \textbf{(2-12)}$$

where y is a column vector containing the final signal profile in adjacent direction, a is column vector containing the information on the dose in each pixel, and *X* is the design matrix, each column indicating the signal that would be observed the two adjacent scans for a unit dose at pixel *i*, designed using the response function $g_i$in Eq. (2-11). The signal can then be reconstructed as,

$$a = (X^t X)^{-1} X^t y \quad \textbf{(2-13)}$$

If the data are considered to have uncertainties σ, then the solution can be written as:

$$a = (X^t V^{-1} X)^{-1} X^t V^{-1} y \quad \textbf{(2-14)}$$

where V is the diagonal matrix with diagonal elements corresponding to the variances σ^2 in the data points y.

This algorithm was the one used to correct all the data in various publications of the group (Ahmed et al., 2017; Yukihara and Ahmed, 2015).

2.7 Tikhonov regularization

The algebraic problem $\min \|Ax - B\|^2$ is an ill-conditioned inverse problem and the solutions are largely affected by small errors in the input data. Therefore, an arbitrarily small error in the input data can lead to and arbitrarily large error in the solution. The pixel bleeding algorithm, which utilizes a Least Square estimate, introduces additional noise in the reconstructed signal due to the presence of Poisson noise in the input signal. In addition, the dose distribution from a realistic radiation field should be smooth and thus, the recovered

solution from pixel bleeding is also expected to be smooth. Regularization is a technique in which a penalty term in introduced in the equation that solves the problem of overfitting. Tikhonov regularization seeks to minimize the argument (Hansen, 1992a),

$$\|Ax - B\|^2 + \lambda^2 \|Lx\|^2, \tag{2-15}$$

where $\|Ax - B\|^2$ is the residual term, $\|Lx\|^2$ is the regularization term, and λ is the regularization parameter or the damping parameter that balances the two terms and weighs the effect of the regularization matrix L on the minimization problem. If $\lambda = 0$ the solution becomes a Least Squares solution.

By choosing L to be the identity matrix *I*, we give preference to solutions with smaller norms, and, theoretically, allow finer resolutions for the kernel to produce distribution behavior. The optimal λ value can be determined by obtaining the location of the corner of the log-log plot of solution norm $\|Lx\|^2$ and residual norm $\|Ax - B\|^2$ known as the L-Curve, as shown in Figure 2-16. The right part of the L-curve corresponds to solutions where regularization error dominates, resulting to over filtering due to over damping, whereas the steep part of the L-curve corresponds to regularized solutions where the errors dominate, resulting in less filtering due to less damping.

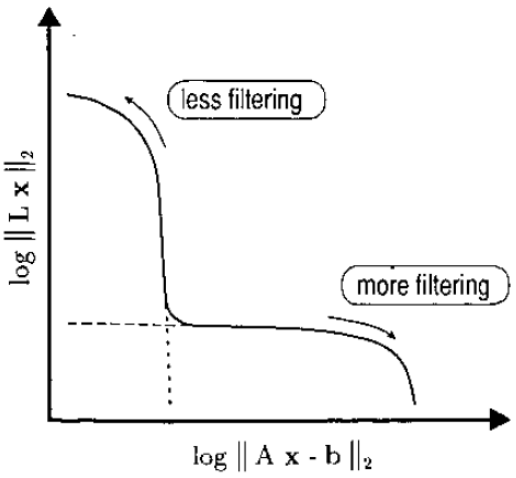

Figure 2-16. A generic plot of the L-curve for Tikhonov regularization on a log-log scale. Reproduced from (Hansen, 1992a).

Using Tikhonov based deconvolution, the signal can be written as,

$$(X^t X + \lambda^2 L^t L)\, a = X^t y \tag{2-16}$$

where, L is the identity matrix with dimensions μ and μ is the number of parameters in g_i.

The solution to Eq. (2-16) can be written as,

$$a = (X^t X + \lambda^2 L^t L)^{-1} X^t y \tag{2-17}$$

If the data are considered to have uncertainties σ, then the solution can be written as:

$$a = (X^t V^{-1} X + \lambda^2 L^t L)^{-1} X^t V^{-1} y \tag{2-18}$$

The choice of regularization matrix L in the Tikhonov regularization significantly affects the quality of the computed solution. When $L \neq I$, where once again *I* is the identity matrix, the regularization problem is in general form. There are many regularization matrices but the most common choices of L are,

$$L_1 = \begin{bmatrix} 1 & -1 & & & & 0 \\ & 1 & -1 & & & \\ & & 1 & -1 & & \\ & & & \ddots & \ddots & \\ & & & & \ddots & -1 \\ 0 & & & & & 1 \end{bmatrix} \quad \textbf{(2-19)}$$

$$L_2 = \begin{bmatrix} 1 & -2 & 1 & & & 0 \\ & 1 & -2 & 1 & & \\ & & 1 & -2 & 1 & \\ & & & \ddots & \ddots & 1 \\ & & & & \ddots & -2 \\ 0 & & & & & 1 \end{bmatrix} \quad \textbf{(2-20)}$$

These matrices L1 and L2 are the finite difference approximation of first derivative and second derivatives. They minimize the difference in the amplitude of the signal without affecting the amplitude of the recovered signal and thus resulting in a smooth solution.

CHAPTER III

MATERIALS AND METHODS

This chapter discusses the experimental details of the studies presented in this dissertation. The details include physical properties of detectors, readout equipment, irradiation sources and data acquisition methodologies.

3.1 Samples

Films

The OSLD films Al_2O_3:C (Lot. # 31218Y2N), also known as Mipox, and Al_2O_3:C,Mg (Lot. # 41128Y2N) are made from (47 ± 3) µm thick layer of Al_2O_3 powder mixed with binder and deposited on a 75 µm thick polyester substrate. The powder used in the Al_2O_3:C films is made of the same material used in Luxel™ and InLight™ dosimetry systems, but with smaller grain size.

MBO powder was prepared using high purity reagents as describe by Gustafson et al. (2019) with 0.3 mol% Ce and 10 mol% Li concentration. The films were manufactured by Agfa NV, Mortsel, Belgium. The powder was milled and mixed with a binder (Lanco™ Wax TF1780 ,The Lubrizol Co.) and deposited on a 175 µm thick PET substrate with a total film thickness of 550 µm.

Point detectors

Al_2O_3:C material was used as point detectors. It is the same material from the OSLD films Al_2O_3:C (Lot. # 31218Y2N) cut into small round pieces of diameter ~7 mm.

As for MBO, the newly developed MBO films were cut into small round pieces of diameter ~7 mm.

3.2 Lifetime equipment

Figure 3-1 shows a diagram of the setup used to measure the lifetime of the phosphorescence signal from the MBO samples. The system uses a green (532 nm) green laser as stimulation source. A 38 mm focal length lens is used to focus the laser into the light guide and a long pass filter (GG425, Schott Corporation) to filter the laser. The laser light is guided towards the sample placed inside the Risø TL/OSL-DA-15 reader using a light guide. A Hoya U-340 filter (7.5 mm thick, Hoya Corporation) is used to filter the OSL signal from the samples and the filtered signal is detected using a PMT (Electron Tube, 9235 QB) which was connected to a dual-channel gated photon counter (model SR-445, Stanford Research Systems). A pulse generator (model BCN 500, Berkeley Nucleonics Corporation) was used to synchronize the laser and photon counter.

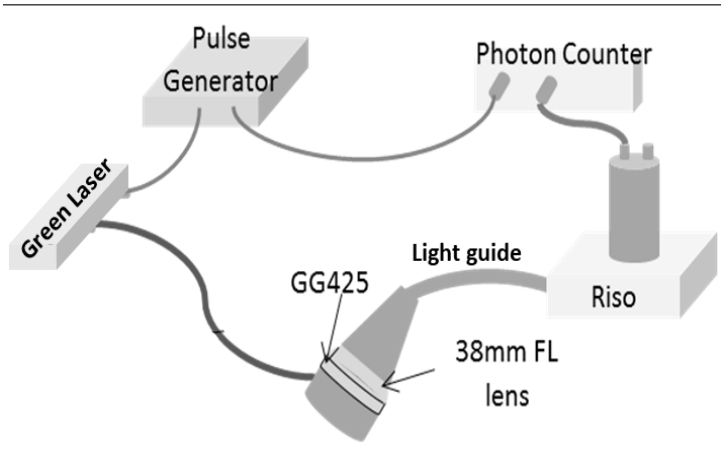

Figure 3-1. Diagram of setup used for lifetime measurements.

3.3 Bleaching

The OSL bleaching unit consists of two halogen lamps, along with Schott GG-495 long-pass filter (3 mm thick, Schott Corporation) for Al_2O_3 films or Schott GG-400 long-pass filter (3 mm thick, Schott Corporation) for MBO films. The average optical power is ~2.4 mW cm^{-2}. The OSL films were bleached overnight to eliminate accumulated dose during storage.

3.4 Detector preparation for clinical irradiations

The Al_2O_3:C and Al_2O_3:C,Mg films were cut into 10.0 cm × 10.0 cm pieces for clinical studies. One corner of the film was cut for proper alignment of the images. The film stack was packaged inside two sheets of light absorbing adhesive flock paper (Stock number 54-586, Edmund Optics) to protect from light.

As for the small detectors, they were packaged in a removable double-sided tape (3M Scotch Double Sided Tape, 3M Scotch, MN, USA). An additional paper sheet was used in front of the sensitive layer of the detectors to prevent the thin detectors from being damaged when removing the tape. Each package contained 5 Mipox detectors.

3.5 Irradiations

3.5.1 Laboratory beta and X-ray sources

Laboratory irradiations were performed using: (i) a 40 mCi $^{90}Sr/^{90}Y$ beta source in the Risø TL/OSL reader (~69 mGy/s), (ii) a 100 mCi $^{90}Sr/^{90}Y$ beta source (~1 mGy/s), and (iii) a cabinet X-ray system (output voltage: 10 – 110 kVp, 3 mA continuous current, Faxitron 43805 N, Hewlett-Packard, ~6.7 mGy/s).

3.5.2 6 MV photon beam

The OSL images used in the algorithm test were from films irradiated using a linear accelerator model Varian 2100EX at the University of Oklahoma Health Sciences Center (OUHSC). The films were irradiated in solid plastic water phantom at 1.5 cm depth with a source-to-surface distance (SSD) of 100 cm.

The OSL films used for small field irradiations were calibrated using a linear accelerator model Siemens Oncor (SN: 4135) at St. John Hospital in Tulsa, Oklahoma. The films were irradiated in solid plastic water phantom at a depth of 10.0 cm with a field size of 10 cm × 10 cm and SSD of 100 cm.

3.5.3 CyberKnife

The small field irradiations were carried out using the CyberKnife Robotic Radiosurgery system (Accuray, Inc., Sunnyvale, CA) located St. John Hospital. It consists of a linear accelerator mounted to a robotic manipulator. The system delivers beams of different field sizes ranging from 5 mm to 60 mm. During irradiation, the films were placed in solid plastic water phantom, at 1.5 cm or 10 cm depth with source to axis distance (SAD) of 80 cm.

3.5.4 MR linac

The magnetic field irradiations using the films were performed using MRidian device (ViewRay Inc., OH, USA) at Fondazione Policlinico Universitario Agostino Gemelli in Italy. It is equipped with three ^{60}Co heads on a ring gantry combined with a 0.35 T split-magnet MRI system. In this system the magnetic field and radiation beam are aligned perpendicular to each other. The measurements using the point detectors were made using the upgraded system with a linear accelerator which replaced the ^{60}Co as radiation source.

3.6 2D laser-scanning system

Figure 2-5 shows the schematics of the 2D OSL reader, which consists of a 532 nm DPSS laser (model GMLN-532-100FED, 100 mW output power, Lasermate Group, Inc.) for stimulation. A 2D galvanometer mirror system (model GVS002, Thorlabs, Inc.) is used to reflect and scan the laser to the OSL film placed on top of a Schott GG-495 long-pass filter (15 cm × 15 cm × 3.5 mm, Schott Glass Corporation). A Hoya U-340 band-pass filter (15 cm × 15 cm × 3 mm thick, Hoya Corporation) is placed on top of the film to keep the film flat. An additional 5-mm thick Hoya U-340 filter is placed in front of the PMT (51 mm diameter, 9235QA, Electron Tubes Inc.) to block any laser light reaching the PMT. The signal recorded by the PMT is amplified by a pre-amplifier (model SR-445, Stanford Research Systems) and digitized using a multichannel scaler (model SR-430, Stanford Research).

During a scan, consecutive rows of the films are scanned in opposite directions and are separated by ~0.17 mm. Each scanned row is divided into 1024 bins with each bin equivalent to 327.68 μs (bin width). The laser power is constantly monitored with a photodiode during scanning (model DET10A, Thorlabs, Inc.).

3.7 Risø TL/OSL readers

OSL measurements from point detectors were done using a Risø TL/OSL reader (model TL/OSL-DA-15, Risø National Laboratory, Denmark). It is equipped with a 40 mCi $^{90}Sr/^{90}Y$ beta source (~69.5 mGy/s) and the OSL signal is detected using a PMT (model 9235QA, Electron Tubes). Blue (broad band centered at 470 nm, 30 mW/cm^2) or green LEDs (broad band centered at 525 nm, 10 mW/cm^2) were used for stimulation.

Figure 3-2. Risø TL/OSL reader, DTU Nutech 2014.

Lifetime measurements of MBO and Al_2O_3 were performed using a Risø TL/OSL-DA-20 reader (DTU Nutech, Denmark) at the Paul Scherrer Institute. The reader is equipped with a 1.48 GBq $^{90}Sr/^{90}Sr$, but the dose rate is ~35 mGy/s because of larger source-to-sample distance. The samples were stimulated with blue LEDs (broad band centered at 470 nm, irradiance of 81 mW/cm^2 at the sample position) and the light was detected using an ET Enterprises PMD9107Q-AP-TTL photomultiplier tube (PMT). Hoya U-340 filters (Hoya Corporation, 7.5 mm thickness) were used in front of the PMT. The reader is equipped with a software-controlled Detection and Stimulation Head (DASH). The reader is also equipped with a Photon Timer attachment (Time-Correlated Single Photon Counter board, PicoQuant TimeHarp 260) for lifetime and time-resolved measurements. Each photon is time-tagged and the photon arrival time can be plotted for various bin widths to analyze the luminescence signal during and after the LED pulses.

The experiments in Section 6.1 were carried out using the same Risø TL/OSL-DA-20 reader (DTU Nutech, Denmark) at the Paul Scherrer Institute. All samples were readout using Green LED for 240 s. Immediately after irradiation, a reference irradiation of 300 s was delivered, and the sample was read out again for 240 s.

3.8 Gamma Analysis

Gamma analysis is a technique for quantitative evaluation of dose distributions. The commissioning a treatment planning system requires comparison of measured and calculated dose distributions. A composite analysis developed by Low et al. (1998), which simultaneously incorporates the dose difference and distance criteria. A distance criteria DTA (distance-to-agreement) is the distance between the measured data point and the nearest point in the same pixel of the calculated dose distribution. This analysis evaluates each point to provide a numerical index (γ) that serves gives a measure of disagreement of the point. The gamma value (Γ) for a measured point can be calculated by using the equation,

$$\Gamma(r_m, r_c) = \sqrt{\frac{r^2(r_m, r_c)}{\Delta d_M^2} + \frac{\delta^2(r_m, r_c)}{\Delta D_M^2}} \quad \textbf{(3-1)}$$

Where, $\Delta d_M^2$is the distance criteria, and $\Delta D_M^2$is the dose difference criteria $r^2(r_m, r_c)$is the distance and $\delta^2(r_m, r_c)$is the dose difference between the measured and calculated point in the distribution given by,

$$r(r_m, r_c) = |r_c - r_m| \quad \textbf{(3-2)}$$

$$\delta r(r_m, r_c) = D_c(r_c) - D_m(r_m) \quad \textbf{(3-3)}$$

The gamma quality index is then given by,

$$\gamma(r_m) = \min\{\Gamma(r_m, r_c)\} - \forall\{r_c\} \quad \textbf{(3-4)}$$

The pass-fail criteria then is:

$\gamma(r_m, r_c) \leq 1$, measured point passes

$\gamma(r_m, r_c) > 1$, measured point fails

As for the analysis, the resolution of the TPS image was ~1.25 mm and was interpolated to 1 mm resolution using the List Interpolation function in Mathematica. In the case of OSL

images the image was binned into 4 pixels × 4 pixels to convert the pixel size into 1.0 mm × 1.0 mm.

3.9 Implementation of the pixel-bleeding algorithm with regularization

In this work the pixel bleeding algorithm (Section 2.6) was used in various configurations and regularizations (Section 2.7). To avoid ambiguity, in Table 3-1. we define the nomenclature to be used in this work. For example, by "Tikhonov algorithm" we mean the pixel bleeding correction algorithm using Least Squares (LS) deconvolution based on the Tikhonov regularization, all points with equal weights and with unitary regularization matrix.

Table 3-1. Nomenclature for the algorithms used in this work.

Nomenclature in this work	**Weight in LS deconvolution**	**Function minimized**
(unweighted) LS-algorithm	$\sigma = 1$	$\|\|Ax - B\|\|^2$
Weighted LS-algorithm	$\sigma = y$	$\|\|Ax - B\|\|^2$
(unweighted) Tikhonov algorithm	$\sigma = 1$	$\|\|Ax - B\|\|^2 + \lambda^2\|\|Ix\|\|^2$
Weighted Tikhonov algorithm	$\sigma = y$	$\|\|Ax - B\|\|^2 + \lambda^2\|\|Ix\|\|^2$
(unweighted) Tikhonov-L1 algorithm	$\sigma = 1$	$\|\|Ax - B\|\|^2 + \lambda^2\|\|L_1x\|\|^2$
(unweighted) Tikhonov-L2 algorithm	$\sigma = 1$	$\|\|Ax - B\|\|^2 + \lambda^2\|\|L_2x\|\|^2$

CHAPTER IV

FEASIBILITY STUDY OF TIKHONOV REGULARIZATION APPLIED TO 2D OSL DOSIMETRY

In this chapter, the feasibility of applying the Tikhonov regularization to improve the directional dependence and the signal-to-noise ratio (SNR) in 2D OSL dosimetry obtained using laser-scanning readout was investigated. The Tikhonov regularization was incorporated into the pixel bleeding algorithm and applied to OSL data for 1D dose profiles simulated with various parameters (luminescence lifetime, ratio of F-center to F^+-center, and pixel dwell times), similar to what have been done to demonstrate the original pixel bleeding algorithm Yukihara and Ahmed (2015). Finally, the algorithm was tested with experimental 1D dose profiles.

4.1 1D Simulation

4.1.1 Simulation results

To test the algorithm outlined in Section 2.7, we applied it to simulated data with various parameters including the luminescence lifetime (τ), ratio of the slow to fast luminescence centers (*R*), system sensitivity (α). This is similar to what has been previously done by Yukihara and Ahmed (2015). A one-dimensional detector with 1000 pixel was simulated and scanned with different dwell times (Δt) in two opposite directions. The detector was of a unitary dose from pixel 200 and 500 but with different sensitivities of ($10^2 – 10^6$) counts/pixel, lifetimes in the (1-100) Δt range, and background of 0.1 counts/pixel was considered. Once the signals were

generated using the response function given by Eq. (2-11), random Poisson noise was added to the signal. The parameter combinations are used to generate different sets of simulated dose profiles as shown in Table 4-1.

The simulated data were then processed with both the LS- and the Tikhonov algorithms (Section 3.9). This was done without weights ($\sigma^2 = 1$) and using the signal as weights ($\sigma^2 = y$). After the corrected signal was recovered, a 2-point moving average was applied to remove some noise from the signal.

In addition to the simulated flat field dose profiles, Gaussian dose profiles were also simulated to perform some of the algorithm tests. One-dimensional detector with 1000 pixels with unitary peak dose of Gaussian beam with FWHM of 117 pixels was generated with the parameters used for the flat field dose profiles.

Table 4-1. Summary of the comparison between the results from the simulated data obtained using the LS-algorithm and the Tikhonov algorithm with weights ($\sigma^2 = 1$) and without weights ($\sigma^2 = y$) in the unitary dose region (201-500 pixels) and in background region (1-200 and 501-1000 pixels). *R* is ratio of F-center (F/F^+), α is system sensitivity and τ is the lifetime of the slow luminescence center, expressed in multiples of the pixel dwell time Δt. Std is the standard deviation of the signal in the region of unitary dose (Std dose) or in the region of no dose (Std bg). TKV indicates the use of the Tikhonov algorithm and LS indicates the use of the Least Squares algorithm.

Set	R	α	t (Dt)	Std dose TKV	Std bg (σ^2=1)	Std dose TKV	Std BG	Std dose LST	Std bg (σ^2
A-1	1	1E+06	1	2.9%	1.9%	2.9%	1.9%	2.9%	1.9%
A-2	1	1E+06	10	3.2%	2.1%	2.9%	1.9%	3.1%	1.9%
A-3	1	1E+06	100	7.5%	4.1%	2.9%	1.9%	7.7%	1.9%
B-1	1	1E+03	1	4.0%	1.8%	4.3%	1.9%	4.3%	1.9%
B-2	1	1E+03	10	9.0%	2.9%	9.0%	2.2%	31.0%	2.2%
B-3	1	1E+03	100	8.9%	5.5%	9.0%	3.8%	267.2%	3.9%
C-1	0.7	1E+03	1	3.8%	2.0%	3.8%	1.9%	3.8%	1.9%
C-2	0.7	1E+03	10	5.3%	1.9%	5.2%	1.9%	5.2%	1.9%
C-3	0.7	1E+03	100	5.5%	2.4%	4.9%	1.8%	4.9%	1.8%
D-1	0.3	1E+03	1	3.4%	1.9%	3.4%	1.9%	3.4%	1.9%
D-2	0.3	1E+03	10	3.6%	2.0%	3.7%	1.7%	3.7%	1.7%
D-3	0.3	1E+03	100	3.5%	1.9%	3.7%	1.9%	3.7%	1.9%
E-1	0.7	1E+02	1	7.9%	1.8%	8.4%	1.6%	8.4%	1.6%

E-2	0.7	1E+02	10	15%	2.4%	15.6%	1.7%	15.6%	1.7%
E-3	0.7	1E+02	100	13.6%	5.5%	14.5%	2.4%	14.5%	2.4%

4.1.2 Weighted and unweighted Tikhonov algorithms

The simulated signals from all the sets were processed either without weights in the LS-algorithm ($\sigma^2 = 1$) or using the signal as weights ($\sigma^2 = y$). Without weights all data points have the same importance in the algorithm, whereas using weights the statistical fluctuation in the data is allowed to increase in absolute terms with the square root of the number of counts, as expected for Poisson statistics. This means that regions in the background region, where few counts are recorded, are not allowed to vary as much as the regions where the signal has higher intensity.

Figure 4-1 compares the results obtained for the simulated signals of set E-3 (τ = 100 Δt, R = 0.7, and α =10^2 counts/pixel), where the graphs on the left side correspond to the results of the unweighted Tikhonov and the graphs on the right side correspond to the results of the weighted Tikhonov. Figure 4-1a and b show the simulated signal in opposite directions, where one can see the effect of pixel bleeding during readout. Figure 4-1c and d show the recovered dose profiles using the Tikhonov algorithm, and Figure 4-1e and shows the residuals.

The results in Figure 4-1 show that using weights in the algorithm reduces the noise in the background region (see Figure 4-1d), as expected. In the case of set E-3 the standard deviation in the background region decrease from 5.5 % to 2.4 % of the maximum signal. Nevertheless, no major difference was observed in the flat dose region (see Figure 4-1c and d). That points to an advantage in the use of weights in the deconvolution algorithm. Other sets showed some improvements with the use of weights as well; see for example sets A-3, B-2, B-3, C-3, E-2 and E-3 in Table 4-1.

Nevertheless, weighting the data increases the processing time by a factor 6-8 and, therefore, it should be demonstrated that it improves experimental data significantly to justify its use.

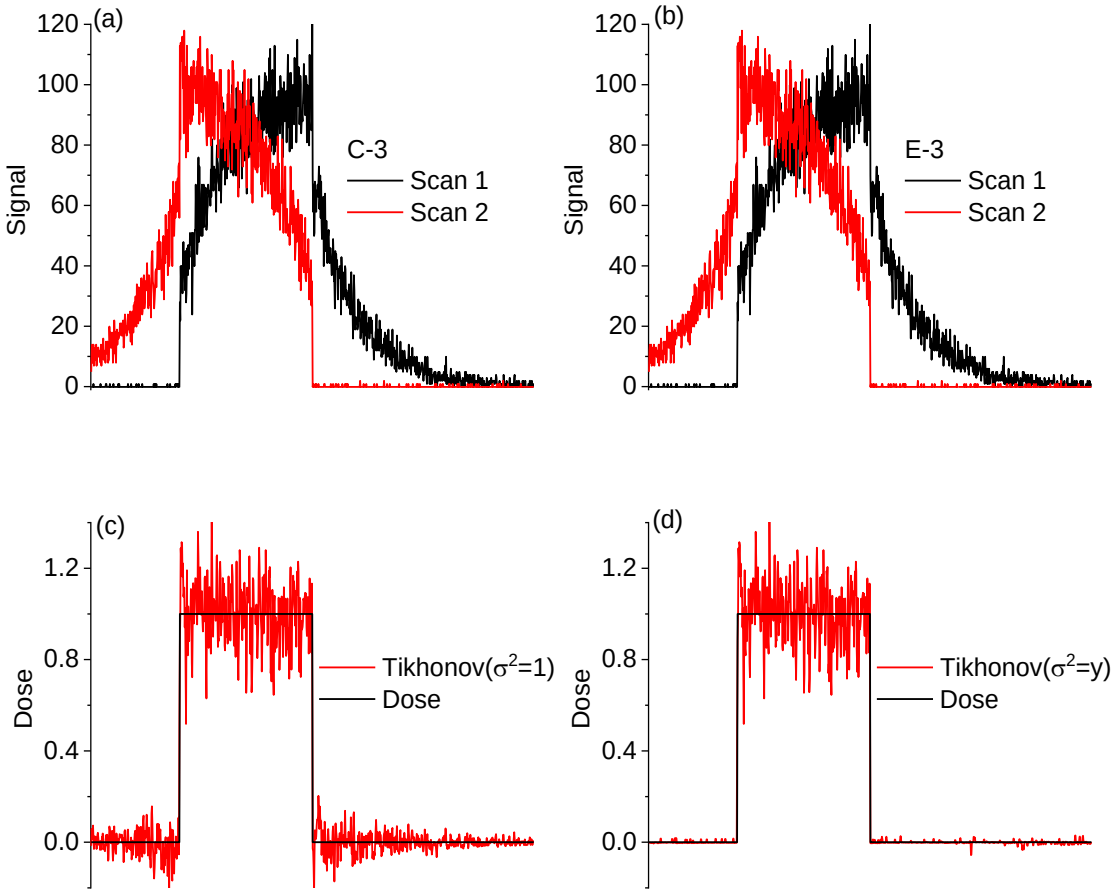

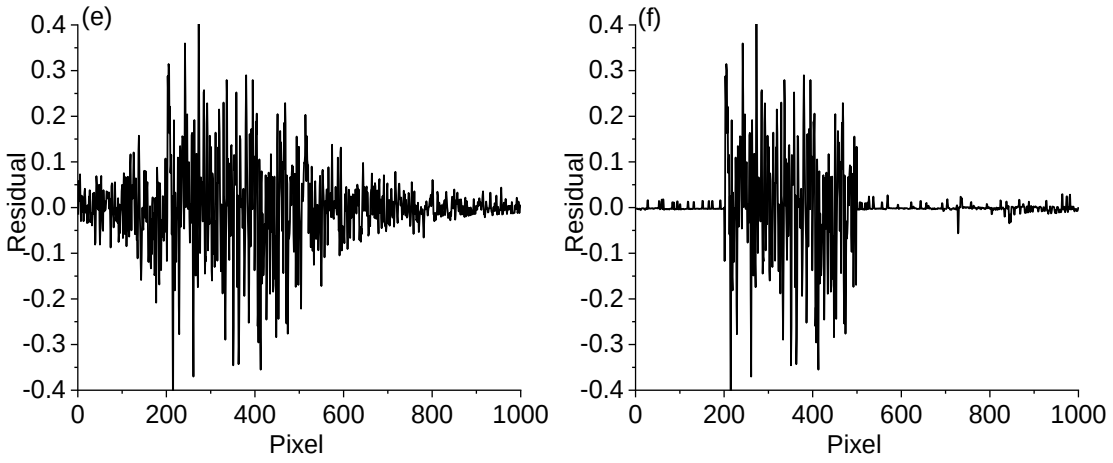

Figure 4-1. (a-b) 1-D simuation of OSL signal obtained from scanning in alternate directions from a flat field dose profile with lifetime τ = 100 Δt and R = 0.7 with intensity of 10^2 counts per pixel. Recovered dose profiles using the (c) (unweighted) Tihonov algorithm and (d) weighted Tikhonov algorithm. (e-f) Residuals dose profiles.

4.1.3 Tikhonov algorithm vs. LS-algorithm

The results from the simulated signals obtained using the Tikhonov algorithm and the LS-algorithm were compared for each simulation set in Table 4-1, in both cases using weights. The results can be seen by looking at the "Std" columns in Table 4-1, which shows the standard deviation of the corrected dose profiles in the dose and in the no dose (background) region, relative to the unitary dose in the flat region.

The results in Table 4-1 show that the Tikhonov algorithm improved the results for the datasets, A-3, B-2, and B-3, because the emission in these cases comes only from slow luminescence centers and, consequently, more noise is introduced by the pixel-bleeding correction algorithm in comparison to the others datasets. These sets are characterized by slow luminescence centers only (R = 1), long luminescence lifetimes (τ = 10 Δt or 100 Δt) and, in the case of set B, low sensitivity (α = 10^3).

The results can be better visualized in Figure 4-2, which compares the profiles recovered using the Tikhonov and the LS algorithms for sets A-3, B-2, and B-3. The first row of graphs

shows the simulated signal resulting from the scan in opposite directions, the second row shows the recovered dose profiles, and the third row shows the residuals.

In these simulation sets, the residuals are considerably smaller using the Tikhonov algorithm than using only the LS algorithm. For set B-3, the standard deviation decreased from 267% to 9% in the dose region.

Nevertheless, no improvements were observed for sets C-3, D-3 and E-3, which are more relevant to the experimental results of Al_2O_3:C and Al_2O_3:C,Mg, because the R values are more representative of Al_2O_3:C,Mg ($R \cong 0.3$) and Al_2O_3:C ($R \cong 0.7$).

Thus, our conclusion is that the Tikhonov algorithm in standard form (with $\boldsymbol{L}$ equal to the identity matrix $\boldsymbol{I}$) does not improve the results in general cases when compared to the LS-algorithm. Therefore, the other Tikhonov regularization matrices needs to be investigated.

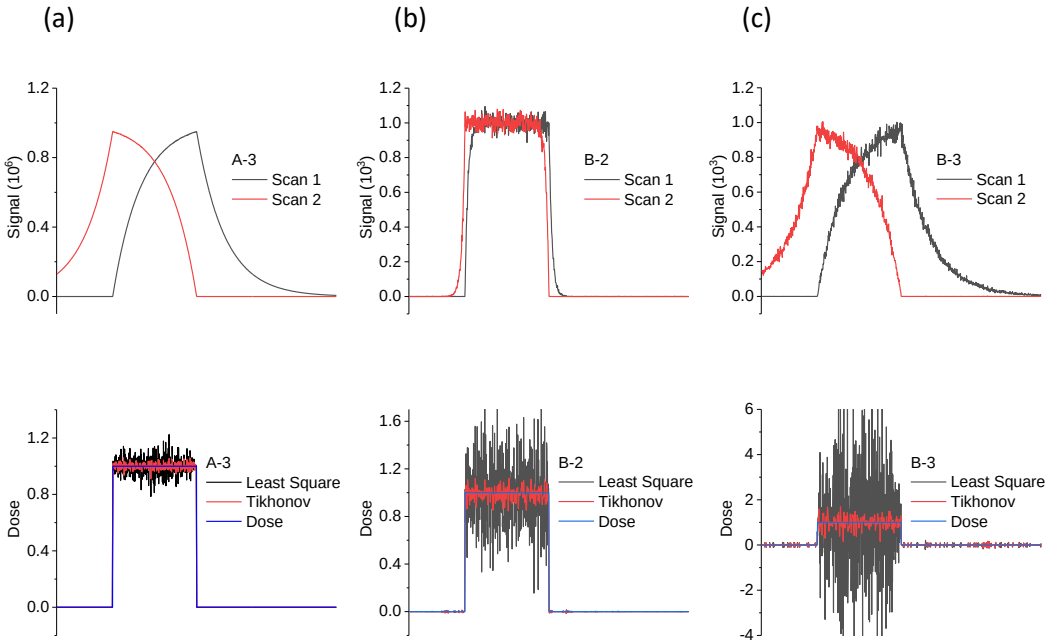

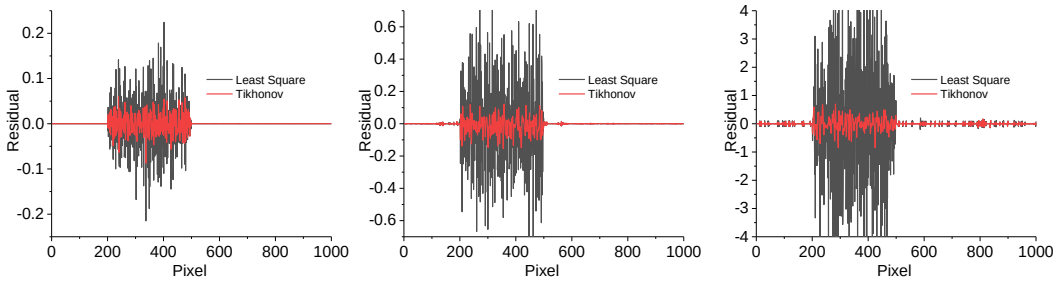

Figure 4-2. 1-D simulation of OSL signal obtained from scanning in alternate directions from a flat field dose profile, reconstructed dose profiles using the LS-algorithm and the Tikhonov algorithm, and residuals with lifetimes: (a) $\tau = 100\ \Delta t$ (set A-3) (b) $\tau = 10\ \Delta t$ (set B-2) (c) $\tau = 100\ \Delta t$ (set B-3).

4.1.4 Smoothing Regularization Matrices

As the Tikhonov in standard form did not show any improvements for sets C, D and E, the Tikhonov algorithm in general form ($\boldsymbol{L} \neq \boldsymbol{I}$) was tested with the simulated dose profile sets (see Section 2.7). We tested the two common choices for the regularization matrices **L1** and **L2** (Section 2.7)**,** which reduces the differences in the amplitude of the recovered signal. To understand the effects of the two matrices, they were applied to a simulated flat field and Gaussian dose profile. The parameters are the same used in set C-3. The unweighted Tikhonov-L1 and –L2 algorithms were applied to the flat field dose profile (Set E-3) with regularization parameter $\lambda = 1$ and to Gaussian dose profiles with increasing λ from 1 to 50.

Figure 4-3 shows the recovered dose profiles from the simulated flat field dose profiles (Set E-3) using the LS-algorithm, Tikhonov-L1, Tikhonov-L2 and Tikhonov ($\boldsymbol{L} = \boldsymbol{I}$) algorithm with regularization parameter $\lambda = 1$. With regularization matrix as the identity matrix the noise in the signal decreases, but the amplitude decreases as well and, therefore, the identity matrix is not a good choice for regularization for our application. On the other hand, the Tikhonov-L1 and Tikhonov-L2 algorithms show similar performance in noise reduction while maintaining the amplitude of the signal. This is due to the presence of the off-diagonal elements.

Figure 4-4 shows the recovered dose profiles from the simulated Gaussian dose profiles using the (a) Tikhonov-L1 and (b) Tikhonov-L2 algorithm. We can see that both L1 and L2 regularization matrices reduce the noise in the profiles more and more with increasing λ. With the L1 regularization, however, as λ increases the dose profile becomes distorted. The peak intensity decreases and the FWHM increases due to the over smoothing. This increases the residuals, as seen in Figure 4-4c.

The regularization matrix L2, however, improves the signal without distorting the profiles and, therefore, is an interesting choice for future implementation of the Tikhonov method.

To compare the noise in the recovered dose profiles using both L1 and L2 regularizations, we applied the regularization to the simulated dose profile for different λ values and measured the standard deviation of the residuals. Figure 4-4e shows the comparison of the standard deviation of the residuals of the dose profiles for Tikhnov-L1 and Tikhnov-L2 algorithm. We can see that for both algorithm the standard deviation decreases to similar minimum level with increasing λ, increasing for higher λ values due to over-smoothing. The acceptable λ range, however, is much wider for the L2-algorithm than for the L1-algorithm. Thus, for pixel bleeding correction of experimental data, Tikhonov-L2 algorithm should be better as it gives a better range for smoothing the solution.

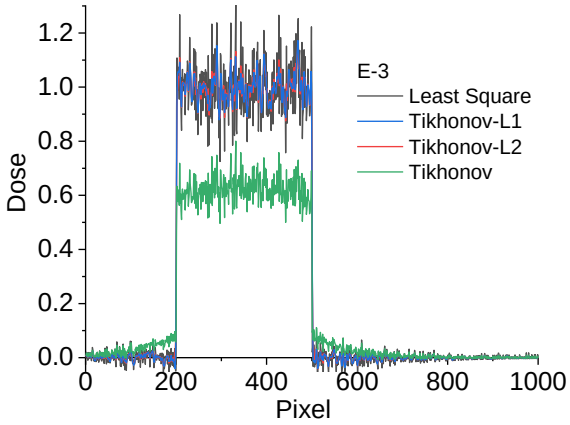

Figure 4-3. Recovered dose profiles from a simulated dose profiles, of parameters from Set E-3, using the LS-algorithm and Tikhonov-L1, Tikhonov-L2 and Tikhonov algorithms (unweighted).

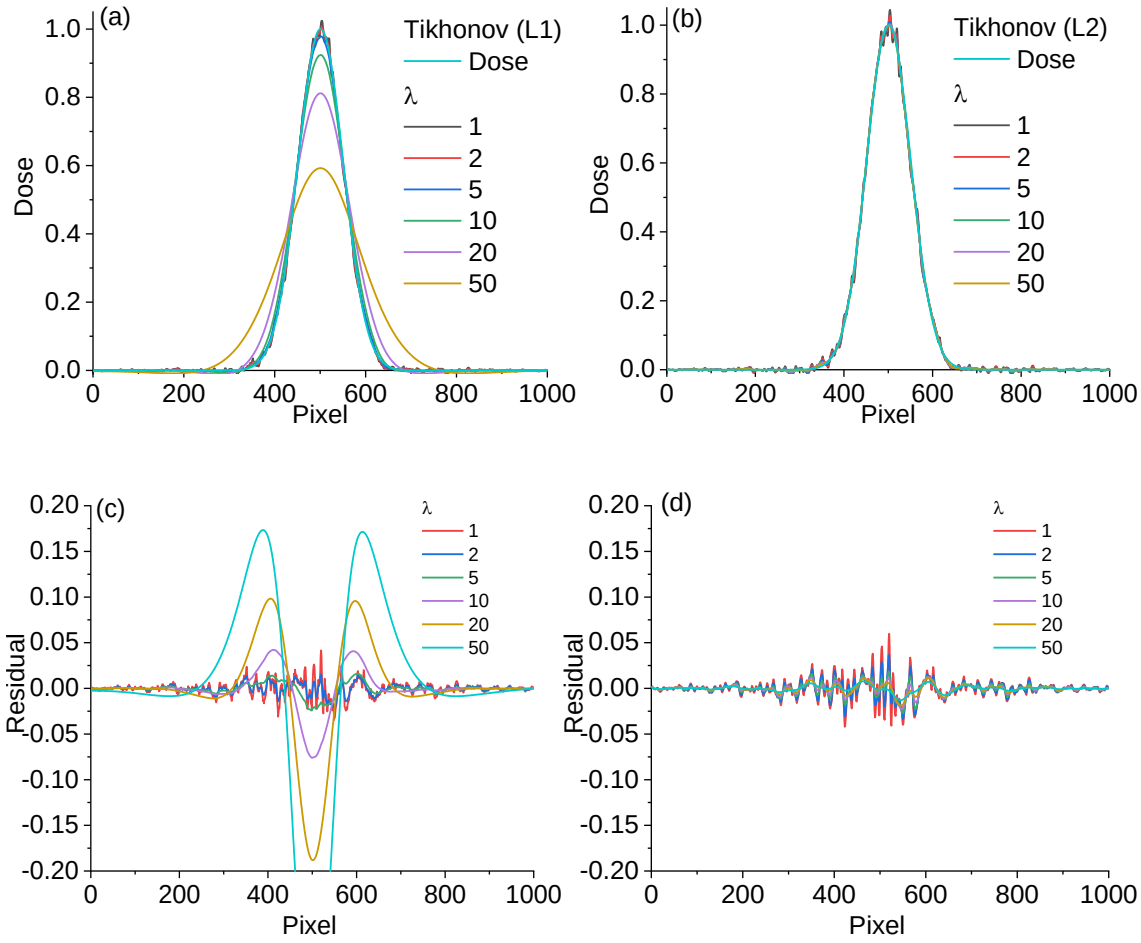

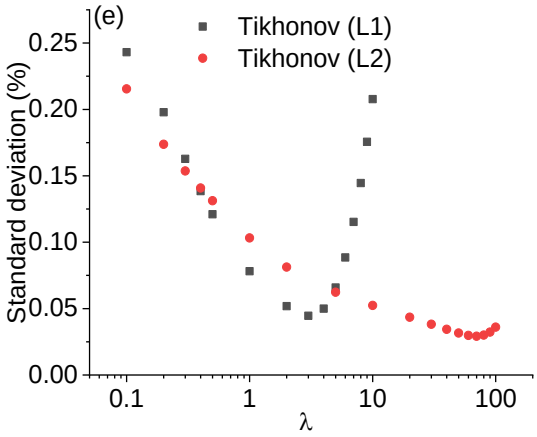

Figure 4-4. (a-b) Gaussian dose profiles, simulated with parameters from Set D-3, recovered using unweighted Tikhonov-L1 and Tikhonov-L2 algorithm. (c-d) Residual of the recovered dose profiles (e) Comparison of standard deviation of the residuals (1-1000 pixel) of the dose profiles obtained for different λ values using Tikhonov-L1 and Tikhonov-L2 algorithm.

The Tikhonov-L2 algorithm was also applied to a flat and Gaussian dose profiles using the simulation parameter sets C-3, D-3 and E-3, which are more relevant to the experimental data. It should be noted that the same λ value was used for all the data sets of both flat field and Gaussian dose profiles. The results were then compared to the profiles recovered using the LS algorithm.

In Figure 4-5, the top graphs (a-c) show the recovered dose profiles and the bottom graphs (d-f) show the residuals of the simulated flat field profiles for sets C-3, D-3 and E-3. The noise in set D-3 is the smallest, as it has the smallest *R* value of 0.3, which means higher contribution from the fast luminescence center to the emission. The dose profile for set E-3 has the most noise, as the sensitivity α for that set is 10^2 counts/pixel. Also, the residuals are lower for the dose profiles recovered using the Tikhonov-L2 algorithm in comparison to those obtained using the LS-algorithm. Calculating the standard deviation in the dose region (200-500 pixel) shows improvement with the Tikhonov-L2 regularization where the standard deviations

are 2.5%, 1.5% and 9% of the mean value. Whereas, the LS-algorithm has standard deviations of 5%, 3% and 14% of the mean value for sets C-3, D-3 and E-3 respectively.

Figure 4-5d-f shows the recovered dose profiles for the Gaussian profiles in the top graphs and the residuals in the bottom graphs. Like flat field dose profiles, the noise is highest in set E-3 and the lowest in set D-3. One can see from the residual graphs that the noise is lower using the Tikhonov-L2 algorithm than using the LS-algorithm in all scenarios.

The results from both the flat field and Gaussian simulated data shows that the uncertainties in the dose region are lower in profiles recovered using the unweighted Tikhonov-L2 algorithm than those obtained using the LS-algorithm.

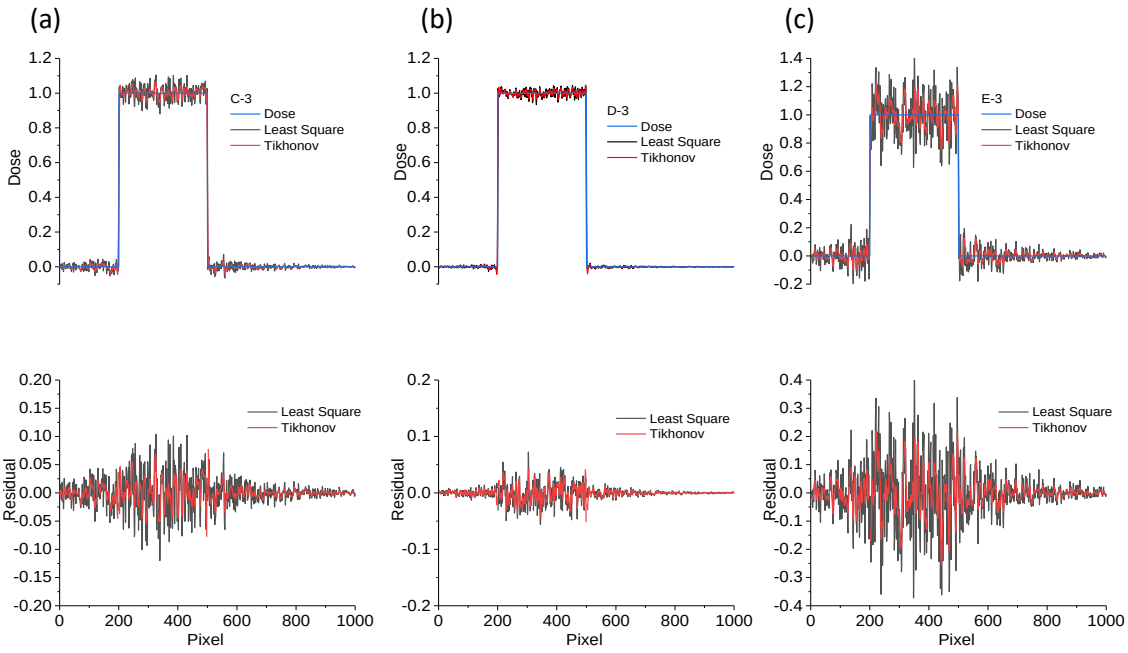

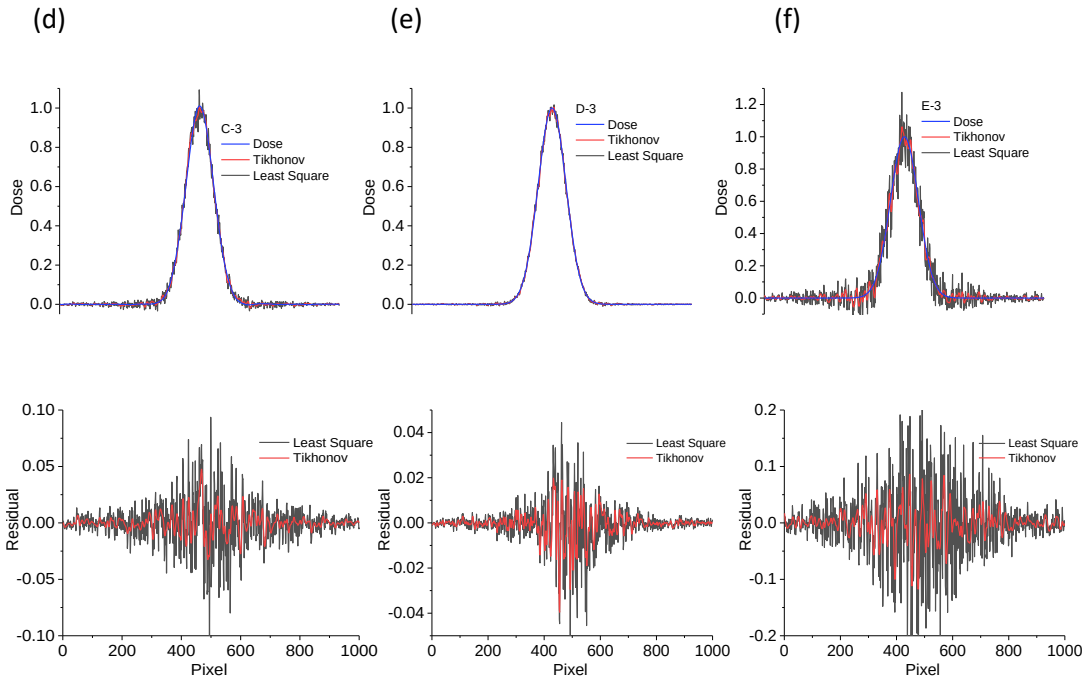

Figure 4-5. Recovered dose profiles from a simulated dose profiles using the LS-algorithm and Tikhonov-L2 algorithm (non-weighted), and residuals for sets C-3, D-3, E-3 respectively with (a-c) flat field dose profiles and (d-f) Gaussian dose profiles.

4.2 Results using experimental data

To test the Tikhonov algorithm (Section 3.9), we applied it to experimental data (1D profiles) from clinical irradiations described in Section 3.5. The data were first corrected for phosphorescence, pixel shift and position dependence. Then the pixel bleeding algorithm was applied to the signal profiles. We compared the noise in the image regions with no film in the background region of the films using the recovered signals from weighted and unweighted Tikhonov to test if weighting is necessary for the analysis at the expense of analysis time. The data were corrected using unweighted LS-algorithm and the Tikhonov algorithm. In addition, for the flat field irradiations we compared the noise in the signal for different doses and for the small field irradiation we compared the noise in the penumbra region.

4.2.1 Weighted Tikhonov

The study using simulated data indicates that the weighted Tikhonov improves the noise in the region of zero dose in the films (Section 4.1). However, the necessity for such improvement needs to be tested with experimental data, as weighting increase the analysis time by 6-8 times. Additionally, the “no-dose” region can be split into two categories: the region where no film is present and the un-irradiated region in the film. Thus, weighted and unweighted Tikhonov algorithms were tested on films irradiated with small fields and flat fields. In the small field irradiation, the film was irradiated with a cone size of 5 mm, whereas in the flat field irradiation a film of 5 cm × 5 cm was used using the setup mentioned in Section 3.5.

Figure 4-6a shows the signal profiles recovered using the weighted and unweighted Tikhonov algorithms, and the LS-algorithm. The signal corrected using the LS-algorithm is only used for reference. As can be seen the noise level is similar in the no dose region in both dose profiles recovered using weighted and unweighted Tikhonov algorithms. This is because the choice of regularization λ parameter in the regularization algorithm reduces the noise in the no dose region as well, and weights may not be necessary.

Figure 4-6b shows the signals recovered from a small 5 cm × 5 cm film irradiated with a flat field with a total dose of 1 Gy. Again, the signal profile obtained using the LS-algorithm is for reference only. In the figure, one can see that the noise in the no film region is less for weighted Tikhonov than unweighted Tikhonov. Nevertheless, when the noise in the no film region (30-150 pixels, 400-550 pixels) is analyzed, one finds that both signal profiles have similar noise. Weighted Tikhonov had 5% noise whereas unweighted Tikhonov has 8%, relative to the given dose.

Thus, in both cases we found that Tikhonov with weights does not provide any significant improvements and only increases the analysis time, as opposed to what was shown using the simulated data (Section 4.2.1). This is because the regularization matrix used in the simulations was the Identity matrix, which did not improve the noise in the signal, whereas the L2 regularization matrix is used in the current test, which reduces the noise in the signal not only in the dose region but also in the background region.

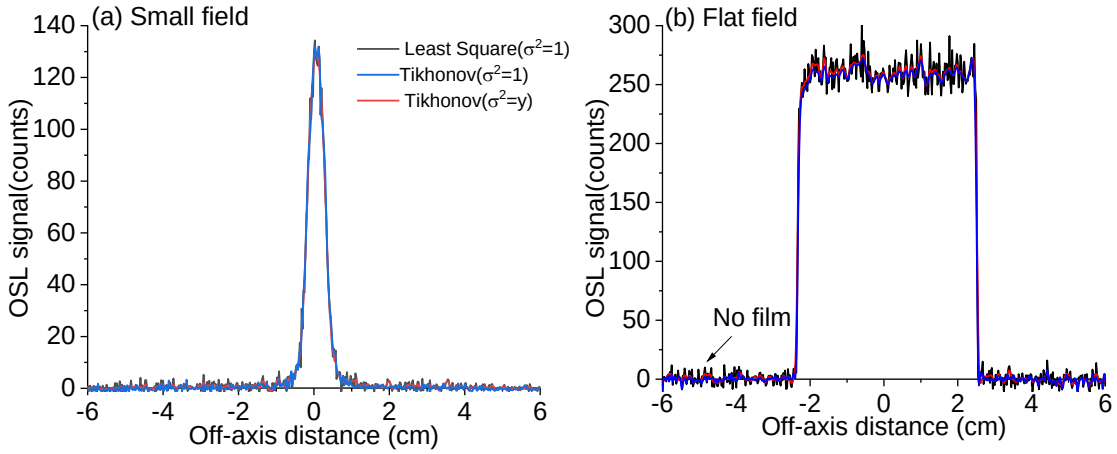

Figure 4-6. Signal profiles recovered using weighted and unweighted Tikhonov algorithm, and the LS-algorithm of a (a) small field of 5 mm cone beam irradiation on a 10 cm × 10 cm film and (b) flat field size of 15 cm × 15 cm irradiation on a 5 cm × 5 cm film.

4.2.2 Flat field irradiations

It was shown using simulated data (Section 4.1.3) that the Tikhonov algorithm improves the signal noise in the dose profiles in comparison to the LS-algorithm. Nevertheless, this result needs to be tested with experimental data. Thus, line profiles of 10 cm × 10 cm films irradiated with total doses of 0.01 Gy, 0.1 Gy, 1 Gy, and 10 Gy were corrected using the unweighted Tikhonov-L2 algorithm and the LS-algorithm.

Figure 4-7 compares the recovered signals using both algorithm for all doses. In all cases the noise in the signal was significantly reduced using the Tikhonov-L2 algorithm. In addition,

the noise in the no film region is also reduced. The noise in the signal (80 – 450 pixel) for all the doses was calculated as shown in Table 4-2. It was found that the signal from the lowest dose had the most improvement in noise compared to the others. The noise was reduced by ~3 times using the Tikhonov-L2 algorithm.

Thus, Tikhonov-L2 algorithm can be used to reduce the noise in films irradiated with flat field doses.

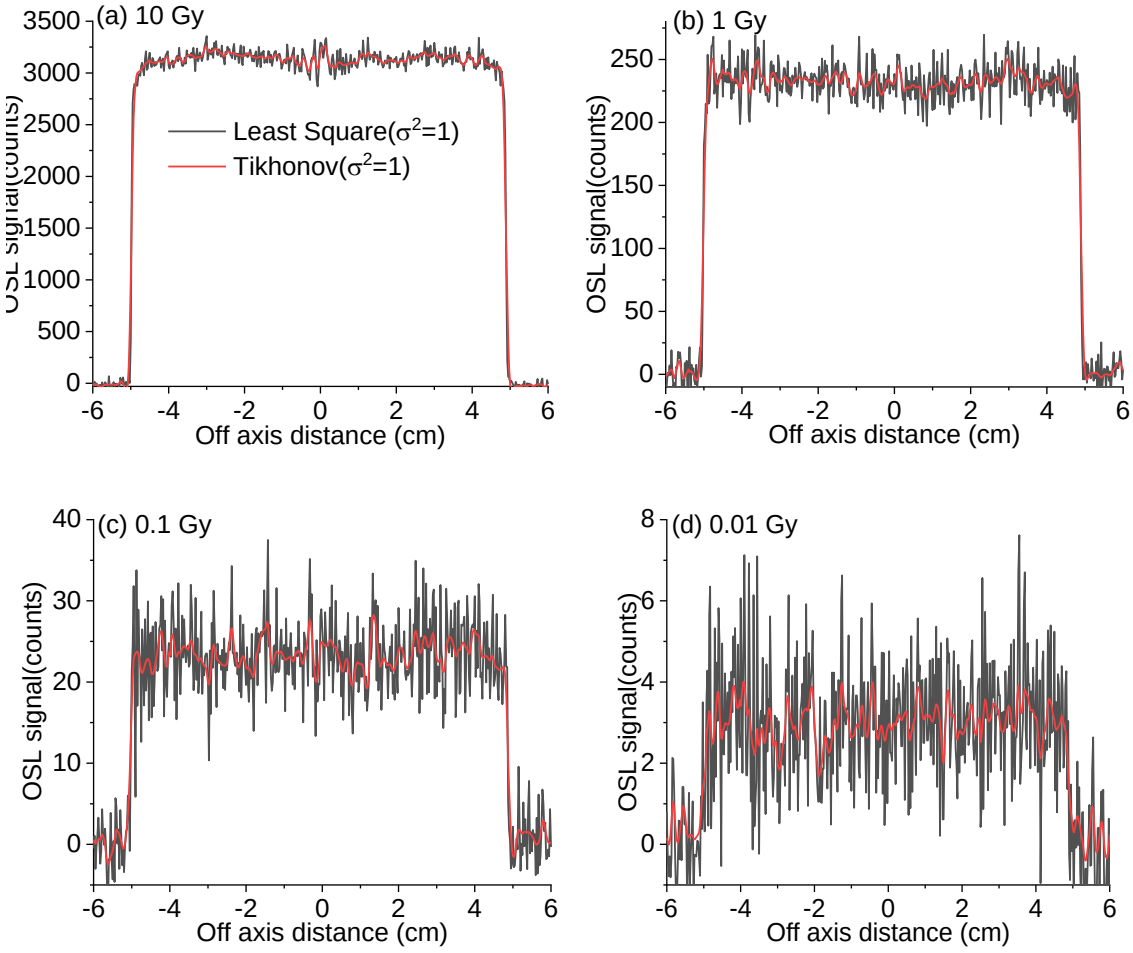

Figure 4-7. Signal profiles from films irradiated with 6 MV linac with (a) 10 Gy, (b) 1 Gy, (c) 0.1 Gy and (d) 0.01 Gy recovered using the Tikhonov-L2 algorithm and the LS-algorithm.

Table 4-2. Comparison between the standard deviation of the signal of the recovered signal profiles in the dose region (pixels 80-450) which was recovered using the Tikhonov-L2 algorithm and the LS-algorithm.

Dose (Gy)	Std dose TKV-L2	Std dose LST
0.01	15%	47%
0.1	7%	18%
1	2.5%	5.8%
10	1.4%	2.4%

4.2.3 Small field irradiations

The Tikhonov algorithm was further tested with films irradiated with small fields using the Accuray CyberKnife (Section 3.5.3). Raw signal profiles from four different films irradiated with cone sizes of 5 mm, 7.5 mm, 10 mm, and 60 mm were corrected using the Tikhonov algorithm and the LS-algorithm. Figure 4-8 shows the corrected signal profiles for all the cone sizes.

As can be seen, the noise in the peak signal for all the cone sizes is less for profiles corrected with Tikhonov algorithm compared to the LS-algorithm. In addition, the noise in the penumbra region of the distribution is also lower when corrected using Tikhonov-L2 algorithm. Thus, the Tikhonov-L2 algorithm is better suited then the LS-algorithm for correction in small field dosimetry as well.

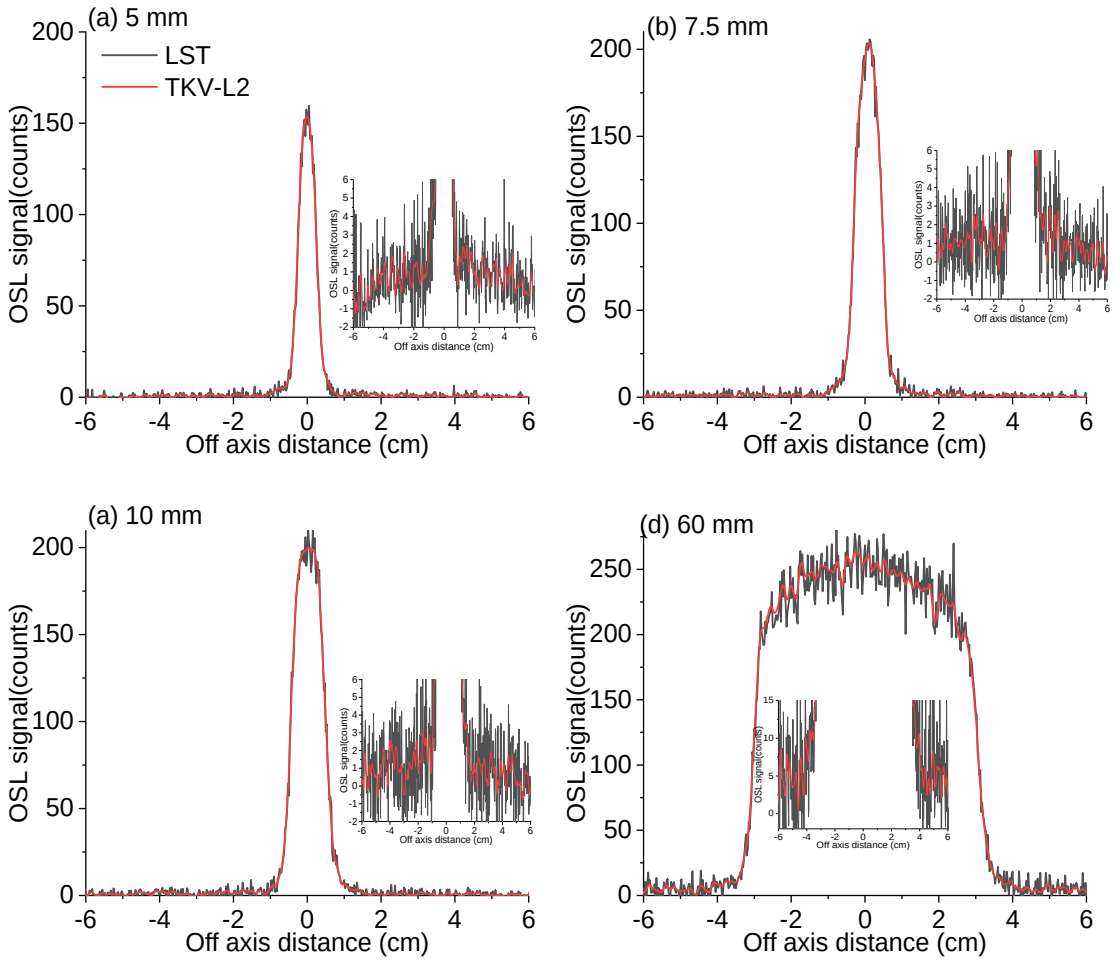

Figure 4-8. Signal profiles from films irradiated with Accuray CyberKnife with cone sizes of (a) 5 mm (b) 7.5 mm (c) 10 mm and (d) 60 mm recovered using the Tikhonov-L2 algorithm and the LS-algorithm.

CHAPTER V

IMPLEMENTATION OF THE TIKHONOV REGULARIZATION TO 2D OSL DOSIMETRY

In the previous section, we discussed the feasibility of implementing the Tikhonov regularization in the pixel bleeding algorithm. 1D simulation and experimental results show that Tikhonov algorithm improves the dose profiles by minimizing the additional noise due to the pixel bleeding algorithm in the reconstructed signal. In this Section, we show the application of Tikhonov algorithm to the full 2D image and test its effect on the spatial resolution and directional dependence in the OSL images. We applied the Tikhonov algorithm to the experimental data obtained using the 6 MV linac and the Accuray CyberKnife (Section 3.5.3) and compare it to the images filtered using noise filters. Finally, we test the dosimetric performance of the Tikhonov algorithm by calculating the output factor in 6 MV X-rays beams and compare them to ionization chamber data. In addition, we also evaluated the performance of Al_2O_3:C,Mg films for CyberKnife dosimetry.

5.1 Influence of regularization parameter (λ) in OSL image

The choice of regularization parameter λ (see Eq. (2-18) affects the level of smoothing in the image and directly affects the image noise. In addition, the OSL image reconstruction algorithm corrects the pixel bleeding in pairs of rows (x-axis) until the whole image is reconstructed. Thus, with the introduction of the Tikhonov algorithm, the noise is also minimized only on the x-axis. This may lead to over smoothing of the data in the x-axis

compared to the y-axis, which is not affected by pixel bleeding. Therefore, it is important to characterize the noise level in both x and y direction of the OSL signal profiles for different λ values.

Furthermore, like any other noise filters, the Tikhonov algorithm may also influence the spatial resolution in the image. Thus, it is important to characterize the influence of λ on the spatial resolution of OSL images.

5.1.1 Image noise

First, we investigated the effect of the regularization parameter λ in the OSL image noise. Raw OSL images from both 10 cm × 10 cm Al_2O_3:C and Al_2O_3:C,Mg films irradiated with doses of 0.01 Gy, 0.1 Gy, 1 Gy and 10 Gy with 6 MV X-ray were recovered using Tikhonov-L2 algorithm and λ values 0.1, 1 and 10.

Figure 5-1 shows OSL images from 10 cm × 10 cm Al_2O_3:C,Mg films reconstructed using the LS-algorithm and the Tikhonov-L2 algorithm with increasing regularization parameter. As can be seen, the images get smoother with increasing λ parameter. Similar results were observed for Al_2O_3:C films.

Figure 5-2 shows the standard deviation calculated at the center of the OSL images of (a) Al_2O_3:C,Mg and (b) Al_2O_3:C over the region of interest (ROI) 1 cm × 1 cm. Application of the Tikhonov-L2 algorithm ($\lambda = 10$) decreases the standard deviation by >3 times in Al_2O_3:C, and >2 times in Al_2O_3:C,Mg. Al_2O_3:C films show better improvement with the application of Tikhonov-L2 algorithm because its images have more noise compared to Al_2O_3:C,Mg images, due to the higher concentration of F^+-center in Al_2O_3:C,Mg.

In conclusion, the results show that implementation of Tikhonov-L2 algorithm improves the SNR in the images with increasing values of regularization parameter λ. For both film types, films irradiated with low doses have significant improvement in noise compared to films irradiated with higher doses with the application of Tikhonov-L2 algorithm.

(a) $\lambda = 0.1$ (b) $\lambda = 1$

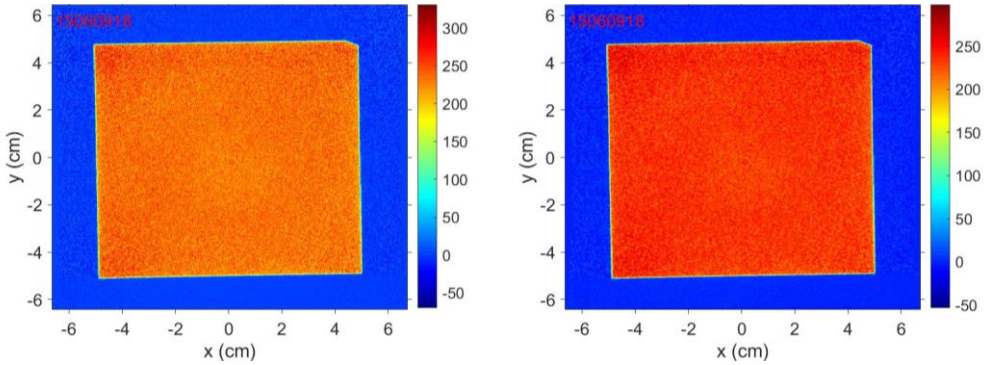

(c) $\lambda = 10$

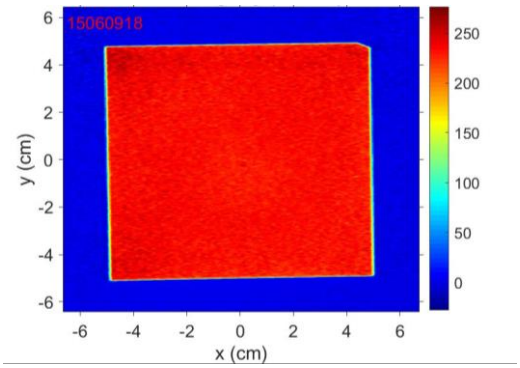

Figure 5-1. OSL images from 10 cm × 10 cm Al_2O_3:C,Mg films irradiated with a total dose 1 Gy using 6 MV X-rays and recovered using the LS-algorithm and the Tikhonov-L2 algorithm (a) $\lambda = 0.1$, (b) $\lambda = 1$, and (c) $\lambda = 10$.

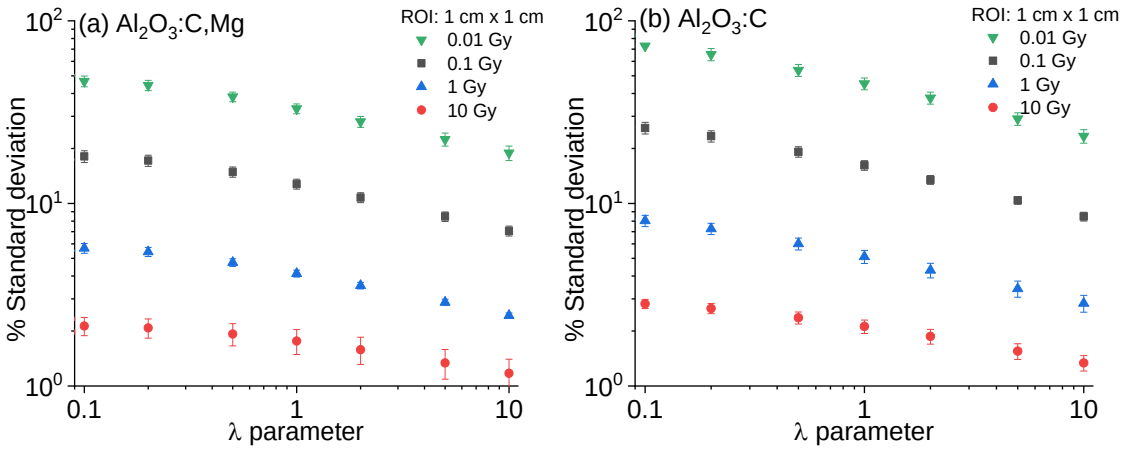

Figure 5-2. Standard deviation per pixel calculated over a 1 cm × 1 cm ROI within the OSL images of (a) Al_2O_3:C,Mg and (b) Al_2O_3:C films recovered using different regularization parameter values. The error bars indicate the standard deviation calculated over 5 different 1 cm × 1 cm regions in the OSL image.

5.1.2 Directional dependence of image noise

Next, the effect of the regularization parameter λ in the directional dependence of the OSL image was studied by analyzing the noise in the signal profiles in x and y direction of the OSL images of both Al_2O_3:C and Al_2O_3:C,Mg from Section 5.1.1.

Figure 5-3 shows two overlapping signal profiles (average of 1 mm), at the center of OSL images in both x and y directions, recovered using λ values 0.1,1 and 10 for films irradiated with a dose of 0.01 Gy, 0.1 Gy, and 1 Gy. The noise in the signal profiles decreases with the application of Tikhonov-L2 algorithm with increasing λ. With higher values of the regularization parameter, however, the directional dependence was reversed, i.e. the noise in the y-axis became larger than that in the x-axis. This is due to over smoothing in the x-direction. Thus, we need to find the best λ parameter that resolves the directional dependence with the similar noise level in either axis in the image.

Figure 5-4 shows the comparison of the standard deviation of signal profiles in x and y-axes of the OSL images of Al_2O_3:C and Al_2O_3:C,Mg films shown in Figure 5-3. In both films the standard deviation of the signal profiles decreases with increasing λ parameter for x-axis. In the y-axis, however, the standard deviation decreases only up to when $\lambda = 1$. This is because the pixel bleeding algorithm is applied only in the scanning direction (x-axis). Thus, the best regularization parameter that can be used in Tikhonov-L2 algorithm for the two film types is $\lambda = 1$.

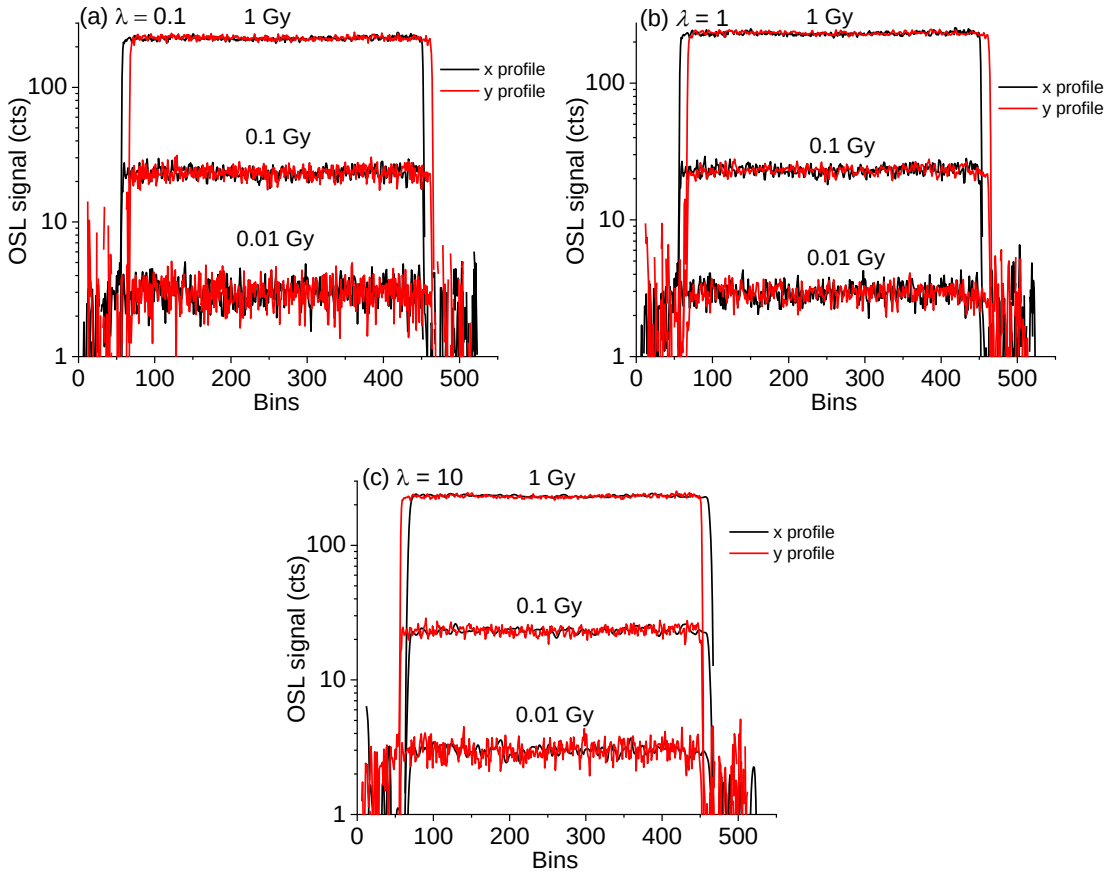

Figure 5-3. Signal profiles (average of profiles spanning 1 mm) in both x and y directions of OSL images, from Al_2O_3:C,Mg films, recovered using the Tikhonov-L2 algorithm with (a) $\lambda = 0.1$ (b) $\lambda = 1$ and (c) $\lambda = 10$ for films irradiated with a total dose of 0.01 Gy, 0.1 Gy, and 1 Gy.

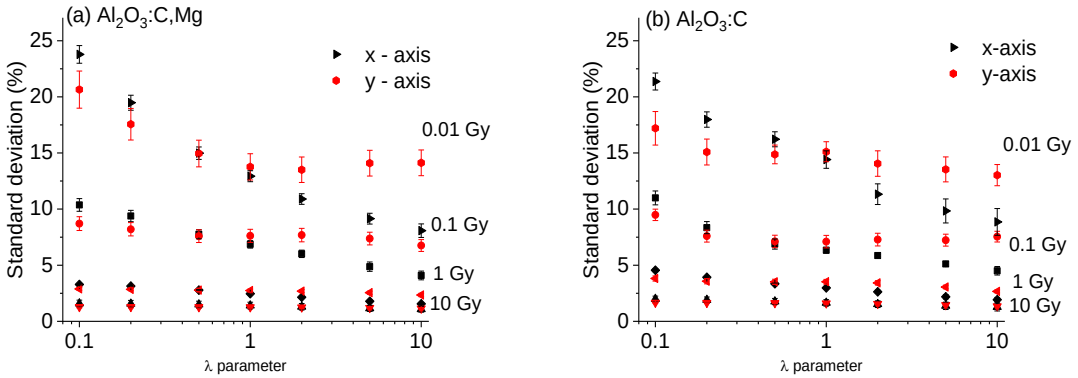

Figure 5-4. Standard deviation per pixel, over the dose region, from the signal profiles in x and y direction, recovered using the Tikhonov-L2 algorithm with different λ parameters from (a) Al_2O_3:C,Mg, and (b) Al_2O_3:C films irradiated with 0.01 Gy, 0.1 Gy, 1 Gy and 10 Gy. The error bars indicate standard deviation of the mean over 5 different signal profiles.

5.1.3 Spatial resolution

To test the effect of the Tikhonov-L2 algorithm on the resolution of the OSL images, we used the image from a piece of Al_2O_3:C,Mg film exposed to a 30 kVp X-ray beam with one corner blocked using a 1.0 cm aluminum block. Figure 5-5 shows the image of the film where one can see the blocked region by the block in the image.

Figure 5-6 shows the signal profiles calculated at the center of the unirradiated region of the OSL images recovered using different λ parameters in both x and y directions. The signal profiles were normalized to the mean signal at the irradiated region over ROI 1 cm × 1 cm. As can be seen in Figure 5-6a, the spatial resolution decreases with increasing λ values. The spatial resolution of the image was calculated by measuring the spatial width of the edges with response decreasing from 90% to 10%. The spatial width increased from (0.93 ± 0.01) mm with $\lambda = 1$ to (1.38 ± 0.02) mm with $\lambda = 10$. The spatial width in y-direction was unaffected and was found to be (0.92 ± 0.01) mm for all λ values. The values following ± represents the standard deviation of the mean width calculated over 50 consecutive signal profiles in the image.

The results showed that the application of Tikhonov-L2 algorithm in the pixel bleeding algorithm affects the spatial resolution of the OSL images in the x-axis. However, with regularization parameter $\lambda < 2$, the spatial resolution is < 1 mm.

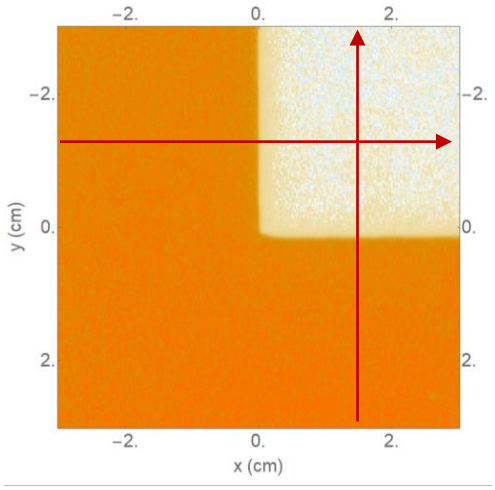

Figure 5-5. OSL image from the 6 cm × 6 cm Al_2O_3:C,Mg film exposed to 30 kVp X-ray beam with one corner blocked using a 3 cm × 3 cm × 1 cm aluminum block recovered using Tikhonov-L2 algorithm.

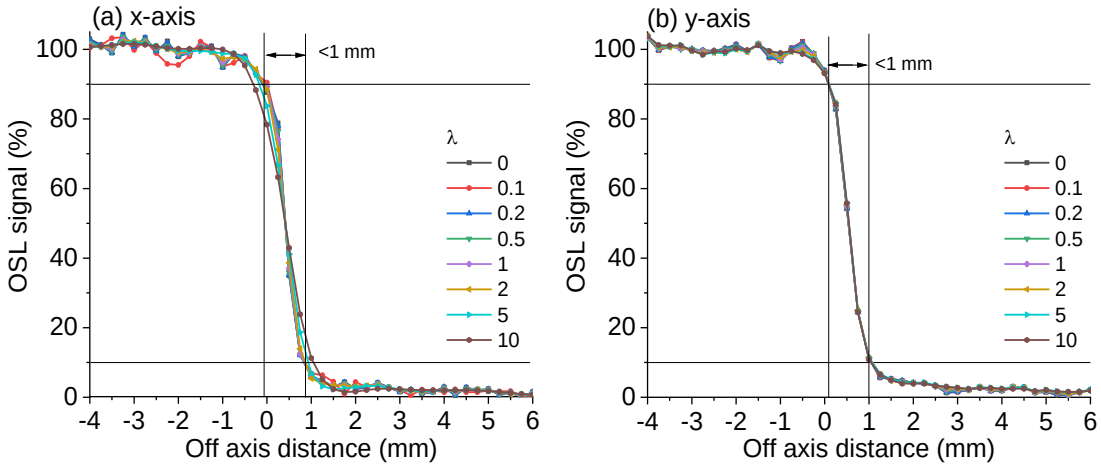

Figure 5-6. Comparison of spatial resolution in (a) x-axis and (b) y-axis using the edge response method from Al_2O_3:C,Mg image recovered using the LS-algorithm ($\lambda = 0$) and the Tikhonov -L2 algorithm with increasing λ parameter.

5.2 Tikhonov versus LS-algorithm

5.2.1 Image noise

This test was done to compare the noise in the OSL images recovered using the LS- and the Tikhonov-L2 algorithms without any additional noise filters. For this 10 cm × 10 cm Al_2O_3:C and Al_2O_3:C,Mg films irradiated with doses 0.01 Gy - 10 Gy using 6 MV X-rays were recovered using the LS- and Tikhonov-L2 algorithms (λ = 1). To better compare the noise in the images recovered using both algorithms, the standard deviation at the center of the images for all doses was calculated.

Figure 5-7 shows the OSL images from 10 cm × 10 cm Al_2O_3:C films irradiated with 1 Gy and reconstructed using the LS- and the Tikhonov-L2 algorithms. As can be seen in the image, the noise is significantly reduced with the Tikhonov-L2 algorithm. Al_2O_3:C,Mg images (not shown) also showed improved noise reduction in the signal with the application of Tikhonov-L2 algorithm.

Figure 5-8 shows the standard deviation calculated at the center of the OSL images of Al_2O_3:C and Al_2O_3:C,Mg films irradiated with 0.01 Gy – 10 Gy over the ROI 1 cm × 1 cm. The OSL images recovered using the Tikhonov-L2 algorithm have significantly lower noise for all investigated doses for both film types compared to the LS-algorithm. The standard deviation was found to be lower by ~ 1.5 times in Al_2O_3:C,Mg films and ~ 1.7 times in Al_2O_3:C films for doses up to 1 Gy with the application of Tikhonov-L2 algorithm. Al_2O_3:C films are improved more by the use of the Tikhonov-L2 algorithm because of the larger noise introduced in the signal by the pixel bleeding algorithm compared to the Al_2O_3:C,Mg films, due to the higher F/F^+-center ratio in Al_2O_3:C than in Al_2O_3:C,Mg. In addition, the noise in the OSL films irradiated with doses higher than 1 Gy already has significantly lower noise than in those irradiate with low doses.

In conclusion, the Tikhonov-L2 algorithm can reduce the noise introduced in the images by the pixel bleeding algorithm.

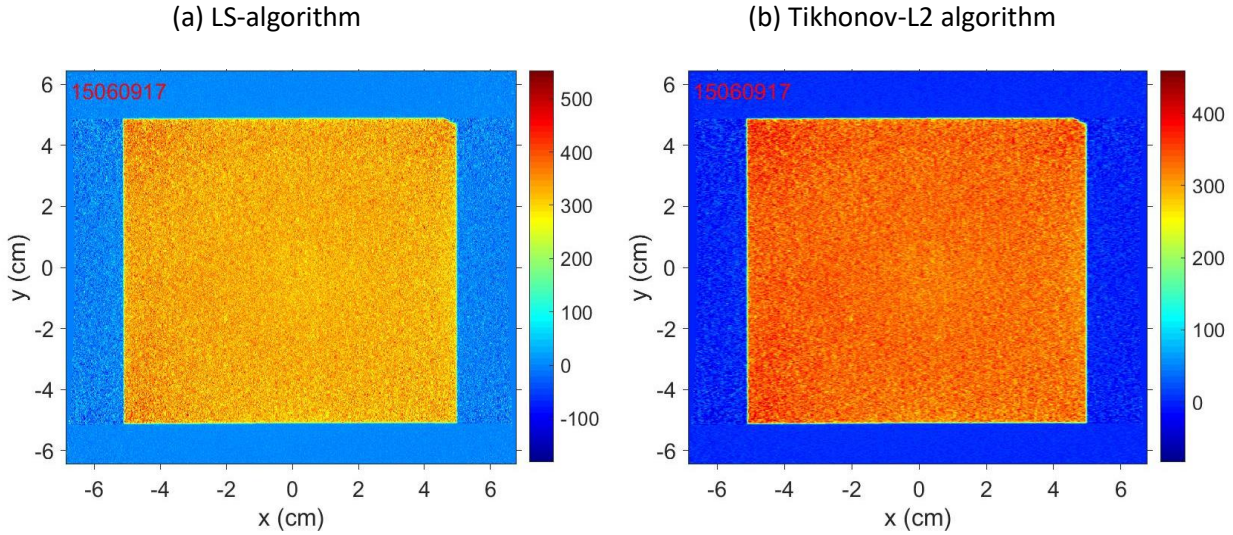

Figure 5-7. OSL images from 10 cm × 10 cm Al_2O_3:C films irradiated with a total dose of 1 Gy using 6 MV X-rays and recovered using (a) LS- algorithm and (b) Tikhonov-L2 algorithm.

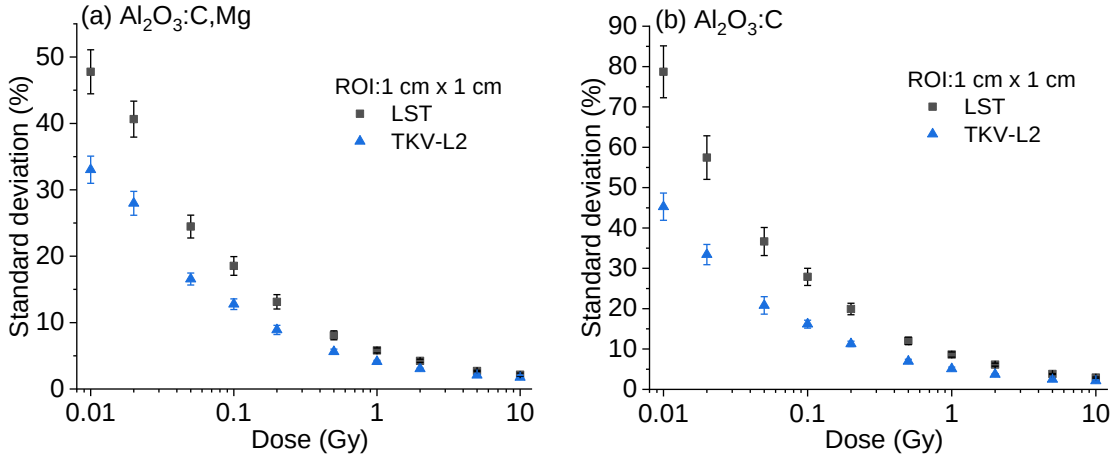

Figure 5-8. Standard deviation per pixel calculated over ROI 1 cm × 1 cm of OSL images of (a) Al_2O_3:C,Mg and (b) Al_2O_3:C films recovered using the LS- and the Tikhonov-L2 algorithms with and without noise filters. The error bars indicate the standard deviation calculated over 5 different 1 cm × 1 cm regions in the OSL image.

5.2.2 Directional dependence of image noise

This test was done to compare the directional dependence of OSL images recovered using the LS- and the Tikhonov-L2 algorithms. For this Al_2O_3:C,Mg, and Al_2O_3:C films irradiated with flat field (15 cm × 15 cm) doses of 0.01 Gy, 0.1 Gy, and 1 Gy were recovered using the LS- and the Tikhonov-L2 algorithms (λ = 1). In addition, Al_2O_3:C,Mg irradiated with small field sizes of 5 mm, 7.5 mm and 10 mm with a total dose of 2 Gy were reconstructed using the LS- and the Tikhonov-L2 algorithms (λ = 1). Then the noise in the signal profiles of the images from both flat field and small field irradiations were compared in both directions.

Figure 5-9a and b shows two overlapping signal profiles (average of 3 cm), at the center of OSL images in both x and y directions for films irradiated with a dose of 0.01 Gy, 0.1 Gy, and 1 Gy recovered using the LS- and the Tikhonov-L2 algorithms. As can be seen, there is more noise in the scanning direction (x-axis) than in the sub-scan direction (y-axis) for images recovered using the LS-algorithm for both film types. In fact, this directional dependence is larger in Al_2O_3:C film images. Nevertheless, the noise in the signal profiles recovered using Tikhonov-L2 algorithm is similar in both directions. This is obvious as the regularization is applied to the fast scan direction.

Figure 5-10a,b shows the signal profiles (average of 2 mm) in x and y direction, at the center of OSL images irradiated with small field sizes of 5 mm, 7.5 mm and 10 mm recovered using the LS-and the Tikhonov-L2 algorithms. When the noise in the signal in both x and y directions are compared, the directional dependence can be observed in signal profiles of images recovered using the LS-algorithm (Figure 5-10a). This effect would have been more prominent in Al_2O_3:C films if they were to be irradiated in similar conditions. This effect,

however, is resolved with the application of Tikhonov-L2 algorithm, as shown in Figure 5-10b, which shows that noise levels in both x and y directions are comparable.

Therefore, it can be concluded that the directional dependence of image noise can be resolved with the application of Tikhonov-L2 algorithm.

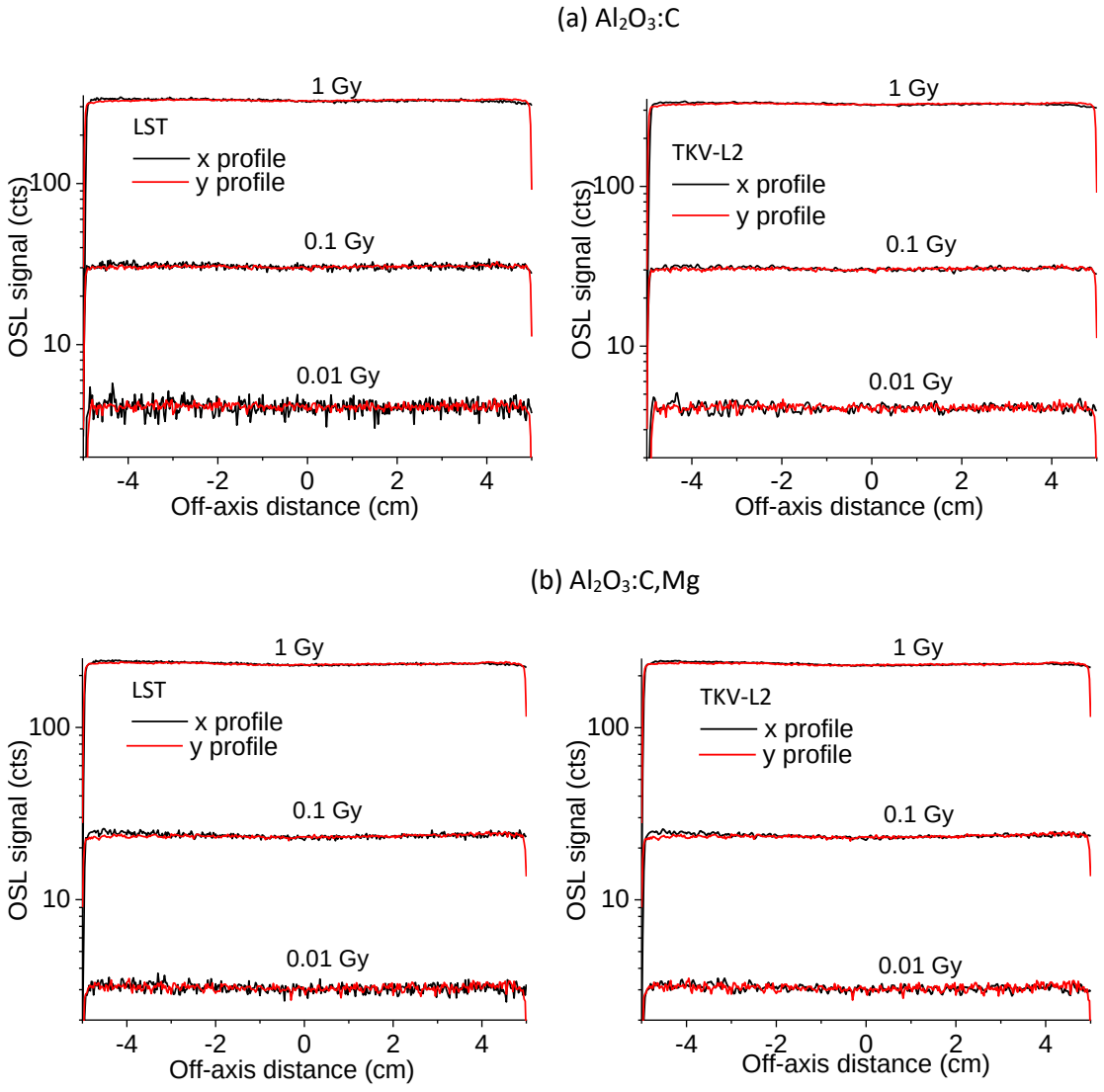

Figure 5-9. Signal profiles (average of 120 consecutive profiles spanning 3 cm) in both x and y directions of OSL images, of (a) Al_2O_3:C and (b) Al_2O_3:C,Mg films, recovered using the LS-and the Tikhonov-L2 algorithms for films irradiated with a total dose of 0.01 Gy, 0.1 Gy, and 1 Gy.

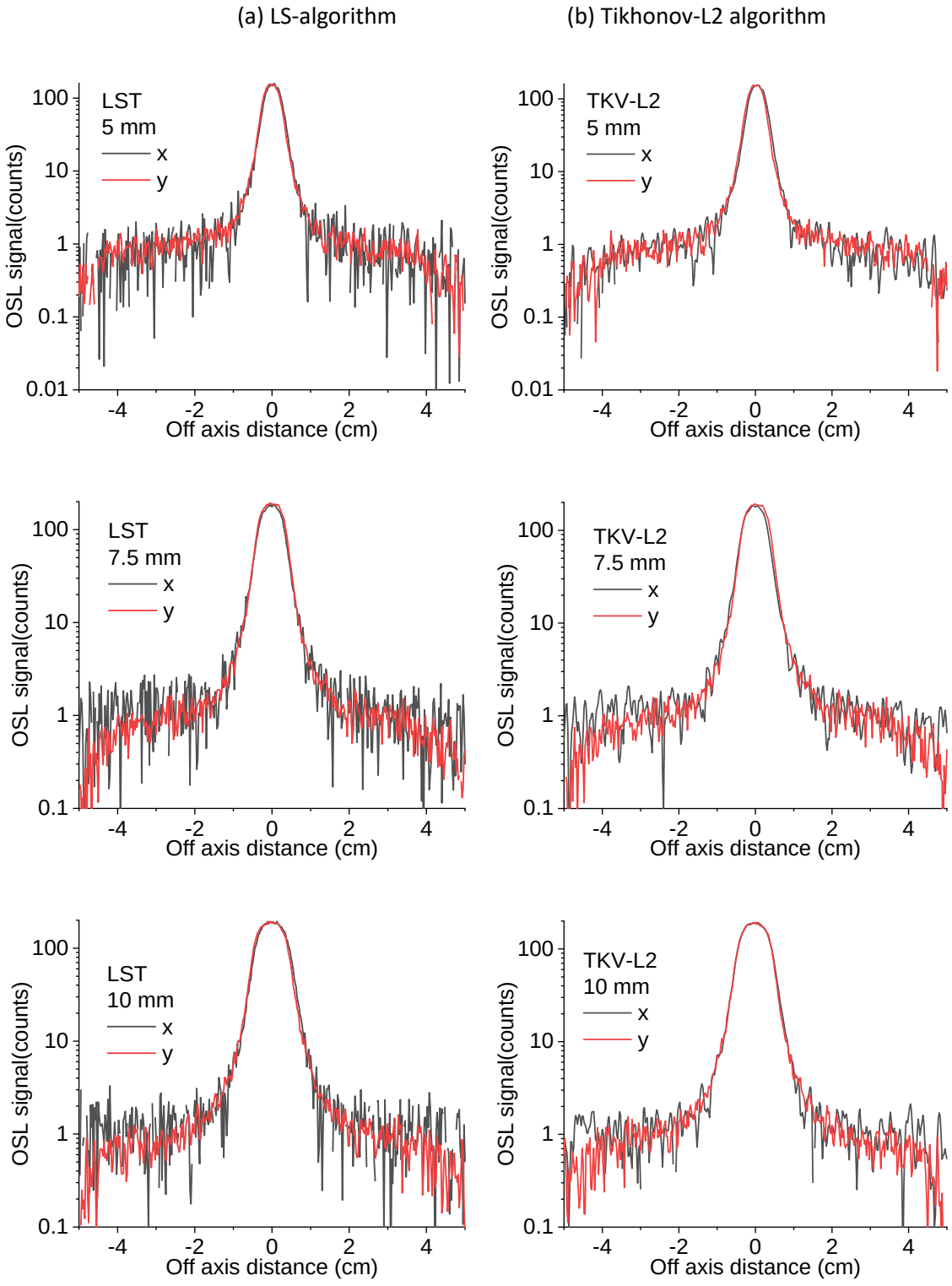

Figure 5-10. Signal profiles (average of 8 consecutive profiles spanning 2 mm) in both x and y directions of OSL images, from Al_2O_3:C,Mg films, recovered using (a) LS-algorithm and (b) Tikhonov-L2 algorithm

for films irradiated with a small field sizes of 5 mm, 7.5 mm, and 10 mm and total delivered dose of 2 Gy.

5.3 Comparison with noise filters

5.3.1 Image noise

This test was done to compare the image noise with the application of noise filter in the images recovered using the LS- and the Tikhonov-L2 algorithms. It was shown by Ahmed (2016) that a Wiener filter (Wolfram Research, 2015) with parameter size of 5 pixels × 5 pixels offers optimum noise reduction while preserving the modulation transfer function (MTF) in the OSL images when compared to other filters: Mean filter, Median filter, and Total Variation filter, all of which are built-in function in *Mathematica* (Wolfram Research, 2015). For this test, the image from Al_2O_3:C,Mg, and Al_2O_3:C films irradiated with different doses using a 6 MV linac were reconstructed using the LS- and the Tikhonov-L2 algorithms ($\lambda = 1$). The reconstructed images were smoothed using a 5 pixels × 5 pixels Wiener filter. The noise in the filtered images was analyzed by calculating the standard deviation at the center of the images for all doses.

Figure 5-11 shows the standard deviation calculated at the center of the OSL images of Al_2O_3:C and Al_2O_3:C,Mg films irradiated with 0.01 Gy – 10 Gy over the ROI 1 cm × 1 cm. With the application of Wiener filter, the image noise is similar within ~1% for both films using both algorithms for all doses. The error bars indicate the standard deviation of the mean signal over the three ROI's. This test shows that the image noise is comparable when an additional noise filter is applied after the image reconstruction with either the LS- or the Tikhonov-L2 algorithms. It is important, however, to note that the Tikhonov-L2 algorithm is not and was never meant to replace noise filters, but rather to reduce the additional noise due to the algorithm in the scanning direction (x-axis). Nevertheless, image noise is not the only parameter in accessing

noise in the image as it does not quantify the directional dependence in the image. This is investigated in the next Section.

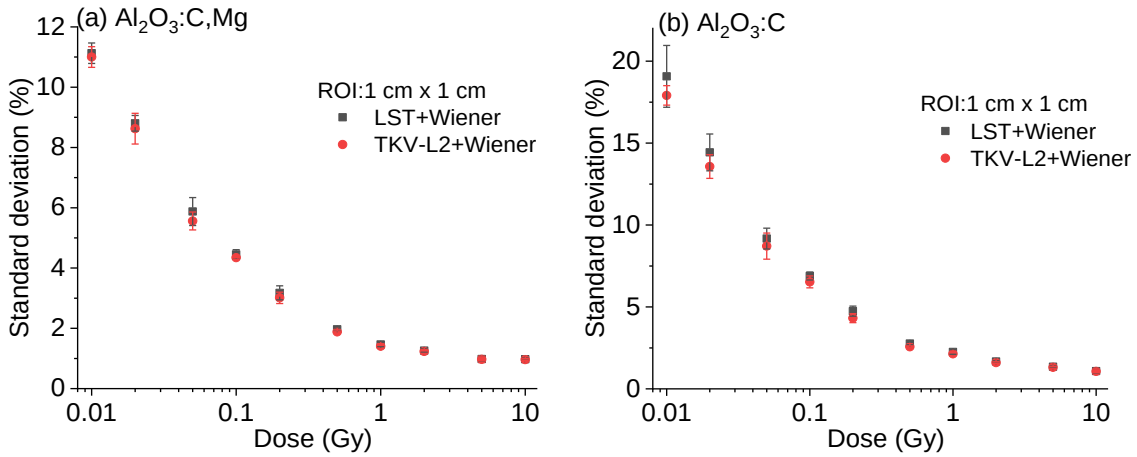

Figure 5-11. Standard deviation per pixel calculated over ROI (1 cm × 1 cm) of OSL images of (a) Al_2O_3:C,Mg and (b) Al_2O_3:C films recovered using the LS- and Tikhonov-L2 algorithms with and without noise filters. The error bars indicate the standard deviation calculated over 3 different ROI in the OSL image.

5.3.2 Directional dependence of image noise

This test was done to compare the directional dependence of OSL images recovered using the LS- and the Tikhonov-L2 algorithms with the application of noise filter. For this, the image from Al_2O_3:C,Mg films irradiated with small field sizes of 5 mm, 7.5 mm and 10 mm with a total dose of 2 Gy were reconstructed using the LS- and the Tikhonov-L2 algorithms (λ = 1). The recovered images were then smoothed using 5 pixels × 5 pixels Wiener filter.

Figure 5-12 shows the signal profiles (average of 2 mm) in x and y direction, at the center of OSL images irradiated with small field sizes of 5 mm, 7.5 mm and 10 mm recovered using the LS- and the Tikhonov-L2 algorithms. When the noise in the signal in both x and y directions are compared, the directional dependence can be observed in signal profiles of images recovered using the LS-algorithm (Figure 5-12a). This is because the Wiener filter is applied to the whole image and does not account for the directional dependence. This effect,

however, is resolved in images recovered using Tikhonov-L2 algorithm, as shown in Figure 5-12b, which also shows that the noise levels in both x and y directions are comparable. This is more prominent for low doses, as shown in the case of small fields, where the tail of the penumbra has low dose and more noise, and the advantage of the Tikhonov-L2 algorithms can be observed.

(a) LS-algorithm

(b) Tikhonov-L2 algorithm

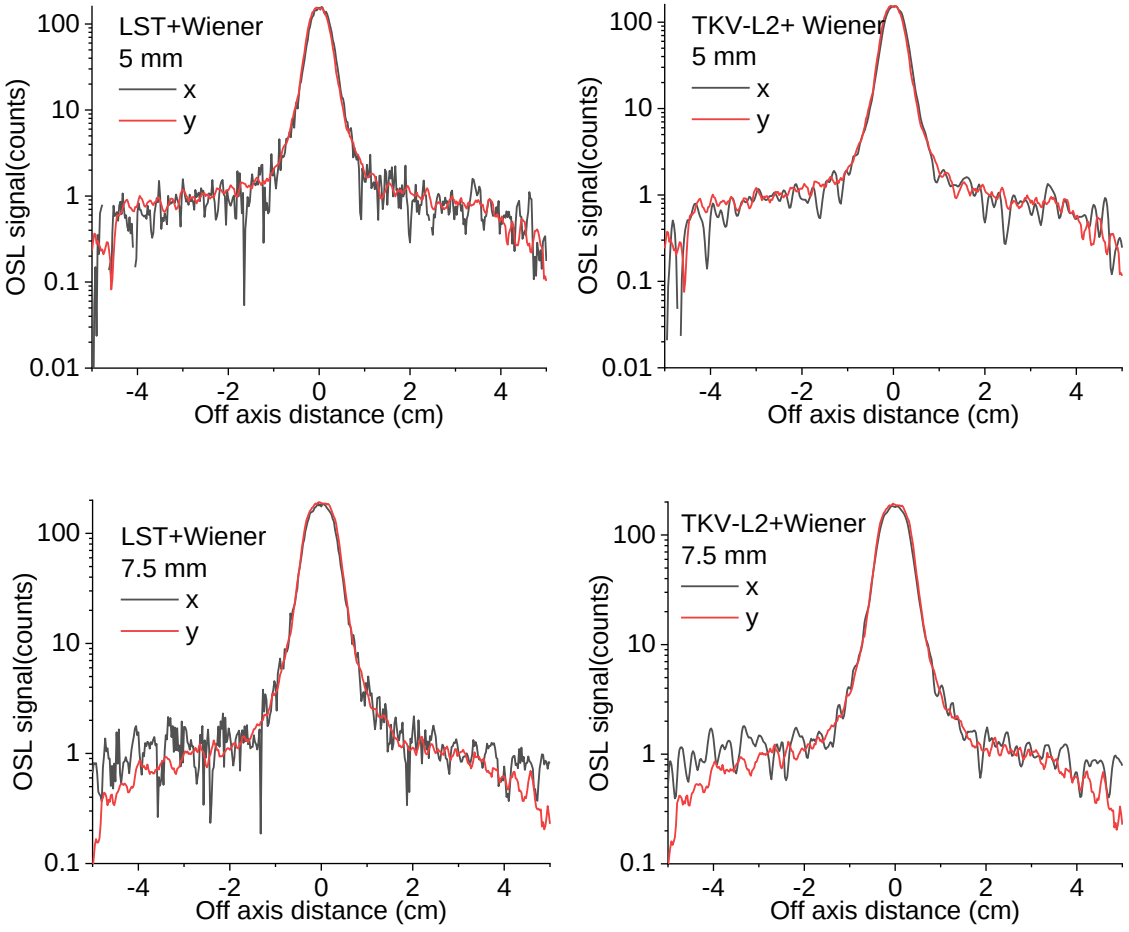

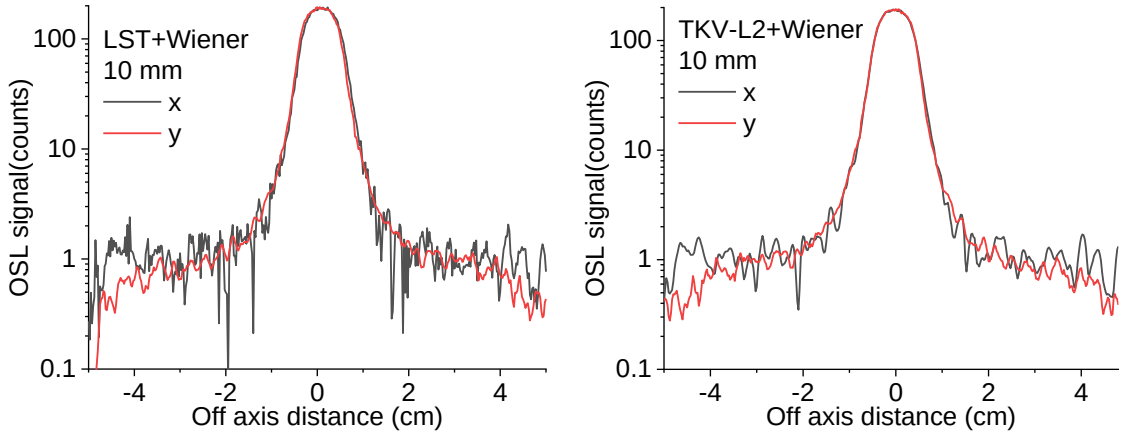

Figure 5-12. Signal profiles (average of 8 consecutive profiles spanning 2 mm) in both x and y directions of OSL images, from Al_2O_3:C,Mg films, recovered using (a) LS-algorithm and (b) Tikhonov-L2 algorithm for films irradiated with a small field sizes of 5 mm, 7.5 mm, and 10 mm and total delivered dose of 2 Gy. The images were further filtered using 5 pixels × 5 pixels Wiener filter.

5.3.3 Spatial resolution

To test the effect of the Wiener filter in the resolution of the OSL images, we used the image from a piece of Al_2O_3:C,Mg film which was exposed 30 KeV X-ray bean with one corner blocked using 1.0 cm aluminum block as shown in Figure 5-5. The OSL image recovered using LS- and Tikhonov-L2 algorithms and further smoothed using a 5 pixels × 5 pixels Wiener filter.

Figure 5-13 shows the signal profiles (average of 1 mm) in x and y directions at the center of the reconstructed OSL image recovered using the LS- and Tikhonov-L2 algorithms. The signal profiles were normalized to the mean signal at the irradiated region over ROI 1 cm × 1 cm. The spatial resolution was found to be < 1 mm in both directions after the application of Wiener filter in the images recovered using both the LS- and the Tikhonov-L2 algorithms.

This test further confirms that the application of Tikhonov-L2 algorithm can be used to resolve the directional dependence and Wiener filter can be applied to further minimize the noise in the OSL images.

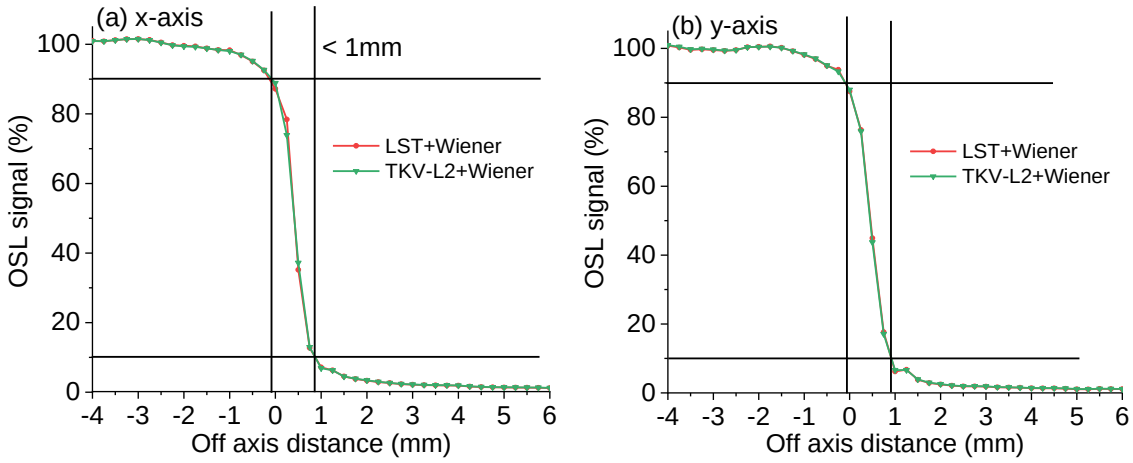

Figure 5-13. Comparison of spatial resolution in (a) x-axis and (b) y-axis using edge response method from Al_2O_3:C,Mg image recovered using LS- and the Tikhonov-L2 algorithm and smoothed using a Wiener filter (5 pixels × 5 pixels).

5.4 6 MV linac irradiations

This study was done to test the dosimetric implications of Tikhonov-L2 algorithm in the image reconstruction algorithm for OSL images. Calibration curves calculated from the OSL images, for both films types Al_2O_3:C and Al_2O_3:C,Mg, was recovered using the LS- and the Tikhonov-L2 algorithms and compared. Then, the calibration curved was used to calculate the output factors for different field sizes and compared to the ionization chamber data along with the associated uncertainties.

5.4.1 Dose Response

We compared the dose response for Al_2O_3:C and Al_2O_3:C,Mg films irradiated using 6 MV X-rays with 15 cm × 15 cm flat field for doses from 0.01 Gy to 10 Gy. The images from both film types were recovered using the LS- and the Tikhonov-L2 algorithms. The images were further smoothed using a 5 pixels × 5 pixels Wiener filter.

Figure 5-14 shows the calibration curve obtained using the average signal over a central ROI 3 cm × 3 cm area (120 pixels × 120 pixels). The difference between the mean values calculated from images recovered using the two methods for both film types was <0.5% for all doses and thus, the same calibration function was used for fitting. This test shows that the application of Tikhonov-L2 algorithm in the image reconstruction does not affect the dose response of the OSL films and only minimizes uncertainties. Next, the data was then fitted using a saturating exponential similar to what was used by Ahmed (2016),

$$y = a_0 x + a_1(1 - e^{-a_2 x}) \quad \textbf{(5-1)}$$

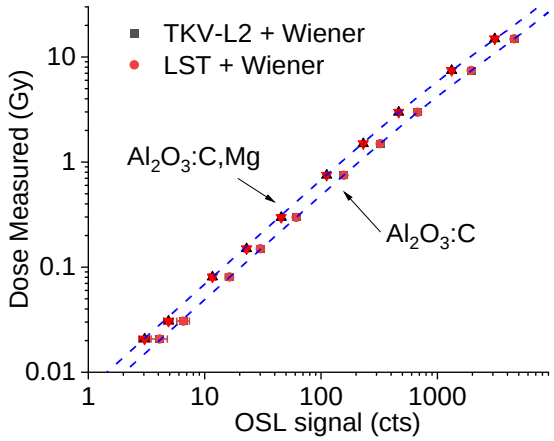

Figure 5-14. Dose response from 10.0 cm × 10.0 cm films of Al_2O_3:C and Al_2O_3:C,Mg, using 6 MV photon beam at d_{max} with 15 cm × 15 cm flat field at 100 cm SSD. The images were recovered using the LS- and Tikhonov-L2 algorithms and filtered using Wiener filter (5 pixels × 5 pixels). Each data point 3.0 cm × 3.0 cm (~120 pixels × 120 pixels) around the central axis and the error bars represent the standard deviation per pixel over the ROI.

Table 5-1. Fitted parameters of the dose response functions for the OSL films shown in Figure 5-14.

Parameters	Al_2O_3:C	Al_2O_3:C,Mg
a_0	(2.66 ± 0.02) × 10^{-3} Gy/count	(3.48 ± 0.05) × 10^{-3} Gy/count
a_1	(2.80 ± 0.03) Gy	(4.7 ± 0.2) Gy
a_2	(1241 ± 24) count	(1340 ± 80) count

5.4.2 Response to field size

To test the dosimetric performance of Tikhonov-L2 algorithm, we calculated the output factors for different field sizes and compared them to ionization chamber measurements. For these images from 10.0 cm × 10.0 cm Al_2O_3:C and Al_2O_3:C,Mg films irradiated using 6 MV photon beam at d_{max} with different field sizes at 100 cm SSD were reconstructed using both LS- and Tikhonov-L2 algorithms. The images were further smoothed using 5 pixels × 5 pixels Wiener filter. Figure 5-15 shows the calculated dose maps for Al_2O_3:C for different field sizes.

(a) 8 cm × 8 cm (b) 6 cm × 6 cm

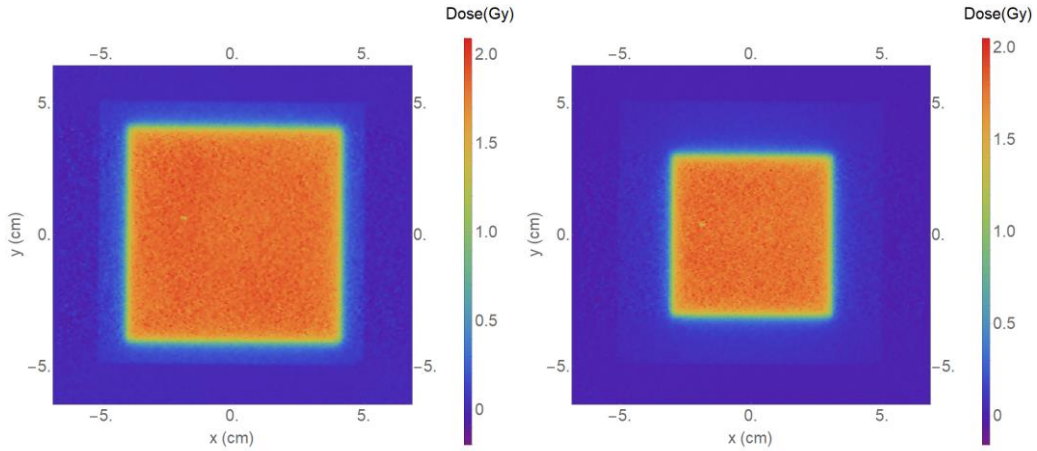

(c) 4 cm × 4 cm

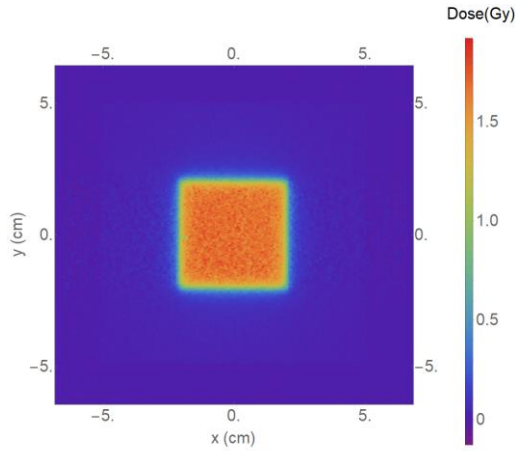

Figure 5-15. Dose maps calculated for 10 cm × 10 cm Al_2O_3:C films irradiated with 6 MV photon flat field of field sizes (a) 8 cm × 8 cm, (b) 6 cm × 6 cm, and (c) 4 cm × 4 cm.

Figure 5-16 shows the dose profiles measured by Al_2O_3:C film by calculating the average doses over strips of 1.0 mm (average of 4 profiles) and 1.0 cm (average of 40 profiles) in x and y direction from the images in Figure 5-15. As can be seen, the noise levels in the signal profiles recovered using the two methods are similar in both x and y axes irrespective of the 1 mm or 1 cm averaging of signal profiles.

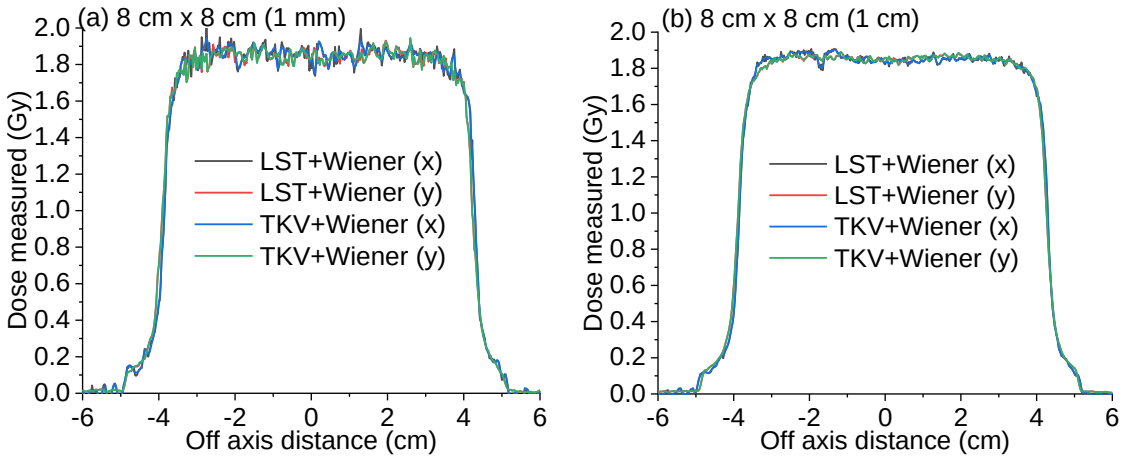

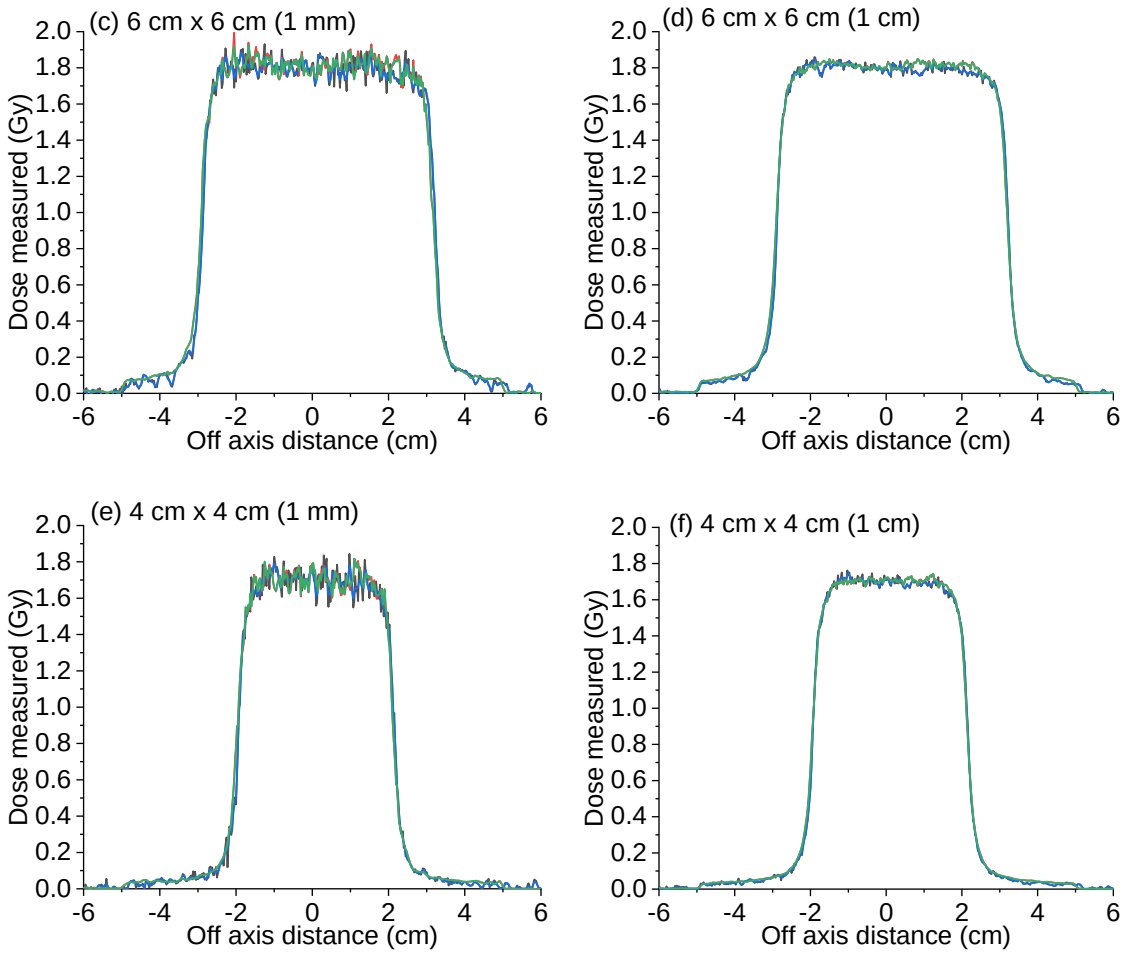

Figure 5-16. Dose profiles of 1.0 mm and 1.0 cm width measured using Al_2O_3:C films irradiated with different field sizes of (a-b) 8 cm × 8 cm, (c-d) 6 cm × 6 cm, and (e-f) 4 cm × 4 cm reconstructed using LS-algorithm and Tikhonv-L2 algorithm.

For a better assessment of the dose and noise in the image recovered using the two methods, the average dose for each film over the central 1.0 mm × 1.0 mm ROI (4 pixels × 4 pixels) and 1.0 cm × 1.0 cm ROI (40 pixels × 40 pixels) for all field sizes were calculated. Table 5-2 summarizes the average doses and output factors (dose normalized to dose at 8 cm × 8 cm) for each film reconstructed using the two methods. The doses measured in the two ROIs at the center of images of Al_2O_3:C and Al_2O_3:C,Mg films have an average error of 1% in comparison to dose measured from the ionization chamber. The output factor measured by the Al_2O_3:C film

agreed with the IC within 0.3%, but for Al_2O_3:C,Mg films the agreement was within 1.1%. The results are similar to what was shown by Ahmed (2016).

The dose difference between the LS-algorithm and the Tikhonov-L2 algorithms for the two film types is <0.1%. In addition, the associated uncertainties over the ROI for both film types are lower in the images recovered using Tikhonov-L2 algorithm than the LS-algorithm. This study demonstrates that the dosimetric performance of the OSL films is not affected by the application of Tikhonov-L2 algorithm.

Table 5-2. Measured doses and output factors (relative to 8 cm × 8 cm field size) for the 6 MV photon (Siemens Oncor) flat field with different field sizes by ionization chamber (IC), Al_2O_3:C, Al_2O_3:C,Mg films reconstructed using the LS- and the Tikhonov-L2 algorithms. The dose was calculated over a 1.0 mm × 1.0 mm (ROI 4 pixels × 4 pixels) at the center of the films. The uncertainty in the measured doses indicates the standard deviation per pixel at the ROI. The values were normalized to the value at 8 cm × 8 cm to calculate output factors and the associated uncertainties indicate the propagated uncertainty.

Quantity	Field area (cm × cm)	IC	LST (1 mm) Al_2O_3:C	TKV (1 mm) Al_2O_3:C	LST (1 cm) Al_2O_3:C,Mg	TKV (1 cm) Al_2O_3:C,Mg
M (Gy)	8 × 8	1.87 ± 0.01	1.84 ± 0.06	1.84 ± 0.04	1.88 ± 0.03	1.88 ± 0.03
	6 × 6	1.82 ± 0.01	1.80 ± 0.07	1.80 ± 0.05	1.81 ± 0.05	1.81 ± 0.03
	4 × 4	1.76 ± 0.01	1.73 ± 0.09	1.73 ± 0.05	1.78 ± 0.06	1.77 ± 0.04
ΔD/D (%)			1%	1%	1%	1%
Output Factor	8 × 8	1	1	1	1	1
	6 × 6	0.97 ± 0.01	0.97 ± 0.09	0.97 ± 0.06	0.96± 0.06	0.96± 0.04
	4 × 4	0.94 ± 0.01	0.94 ± 0.11	0.94 ± 0.06	0.94 ± 0.08	0.94± 0.04
ΔOF/OF (%)			0.2%	0.3%	1.1%	1.1%

5.5 CyberKnife irradiations

The beam commissioning for a CyberKnife system requires input data which is specific to the dosimetric algorithm used for the treatment planning. Monte Carlo and Ray-Tracing are two commonly used algorithms which requires the following core set of data for beam characterization,

- Tissue Phantom Ratios (TPR) which is defined as the ratio of the dose at a given point in phantom to the dose at the same point at a fixes reference depth, usually 5 cm. This is a rough measure of the energy spectrum.
- Off-Central Ray Ratios (OCR), which is the measure of dose distribution as a function of off-axis distance, normalized to the central axis.
- Output Factors (OF's), which is the measure of radiation output change as a function of field size (cone size). All output factors are normalized to the fixed cone of 60 mm.

To show the application of OSL films in small field dosimetry along with the implementation of the Tikhonov-L2 algorithm in the image reconstruction algorithm, all the images in these tests were reconstructed using the Tikhonov-L2 algorithm. The images were then further smoothed using 5 pixels × 5 pixels Wiener filter.

5.5.1 Film calibration

The calibration curve was obtained by irradiating 10.0 cm × 10.0 cm Al_2O_3:C,Mg films using a linac (Section 3.5.2) with 6 MV X-rays at a depth of 10.0 cm with a field size of 10 cm × 10 cm and SSD of 100 cm. For linearity check, an ionization chamber (Exradin chamber, model A19) was placed at 16 cm water equivalent depth during all film irradiations. Three films were irradiated individually for each dose.

Figure 5-17 shows the calibration curve for Al_2O_3:C,Mg films. Each data point is an average of three film measurements calculated over the over 2.0 cm × 2.0 cm (~80 pixels × 80 pixels) around the central axis. The error bars represent the standard deviation of the mean between the three film measurements. The data were fitted using a saturating exponential given by,

$$y = a(1 - e^{-bx}) \quad \textbf{(5-2)}$$

The fitted parameters for the dose response curves are shown in Table 5-3.

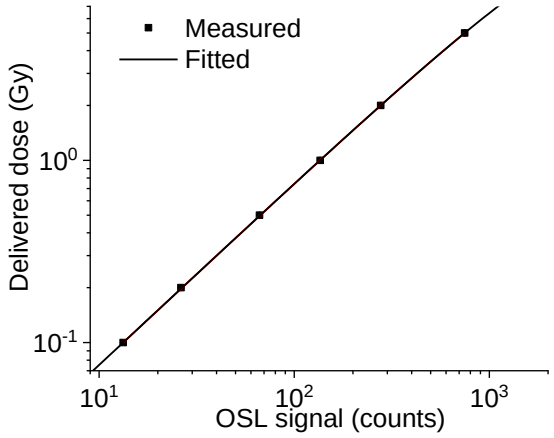

Figure 5-17. Calibration curve obtained with irradiation in linac (Section 3.5.2) at a depth of 5.0 cm with field size 10 cm × 10 cm and SSD: 100 cm using 10.0 cm × 10.0 cm Al_2O_3:C,Mg films. Each data point is the average of three film measurements calculated over 2.0 cm × 2.0 cm (~80 pixels × 80 pixels) around the central axis. The error bars indicate the standard deviation of the mean of the three film measurements.

Table 5-3. Fitted parameters of the dose response functions for the OSL films shown in Figure 6-9.

Parameters	Al_2O_3:C,Mg
a	(22.9116 ± 0.368) Gy
b	(3.29 ± 0.05) × 10^{-4} Gy/count

5.5.2 Off-Central Ray Ratios (OCR)

To obtain the OCR values, 10 cm × 10 cm Al_2O_3:C,Mg films were irradiated using the Accuray CyberKnife (Section 3.5.3) at a depth of 1.5 cm in a solid water phantom and source to axis distance (SAD) of 800 mm with different cone sizes of 5.0 mm, 7.5 mm, 10 mm with a total delivered dose of 5.0 Gy. Three films were irradiated for each cone size and one film was irradiated with 60 mm for reference. The measurements were repeated using a stereotactic diode (PTW 60017, 0.03 mm^3 active volume, 1.2 mm diameter) in a water tank.

Figure 5-18 shows the 3D representation of the 2D dose measured by the Al_2O_3:C,Mg films. As can be seen, the dose decreases with decreasing cone size. Figure 5-19 shows the

lateral dose profiles in x and y direction of the OSL films compared to the profiles measured using a diode. The dose was normalized to the average signal over 1.0 mm ROI (4 pixels × 4 pixels) at the center. Each OSL signal profiles are an average of 1 mm (4 consecutive profiles) at the central axis. The signal profiles measured using the OSL films are wider than the one measured with the diode. This was observed in the lateral dose profiles measured at a depth of 10 cm as well (not shown).

Table 5-4 shows 80% - 20% penumbra distances measured using diode and OSL films. The uncertainties in the OSL films are measured from the x and y profiles from the 3 films for each cone size. The OSL films agree well with diode within uncertainties for cone size of 5.0 mm and 7.5 mm. The discrepancies for the 10 mm cone and 60 mm cone are, however, not clear.

Therefore, in order to better understand the discrepancies in the measurements between the OSL films and diode additional measurements using an additional detector like Gafchromic films would be helpful.

(a) 5 mm

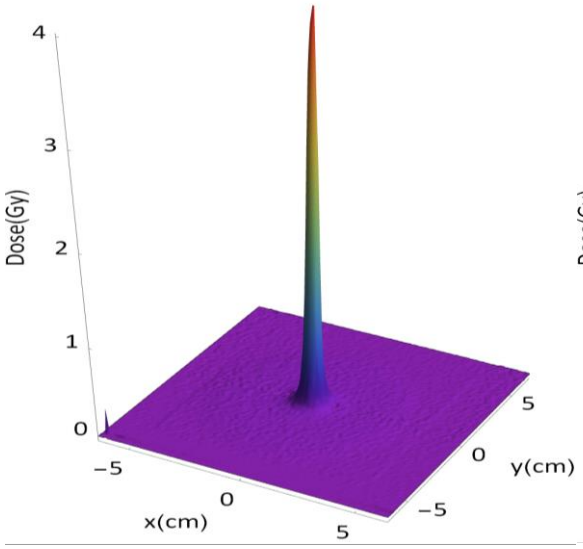

(b) 7.5 mm

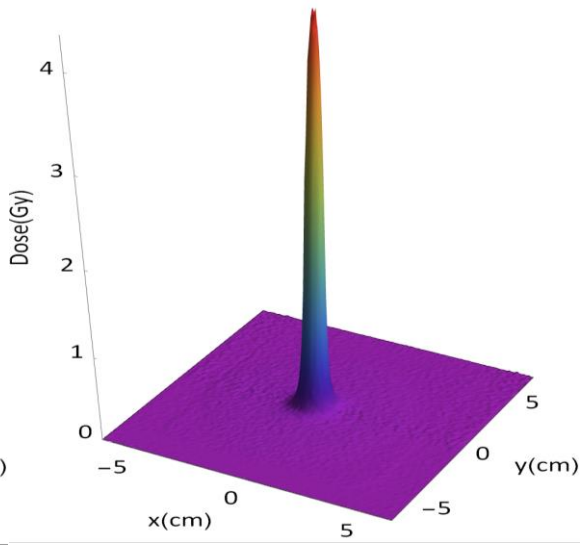

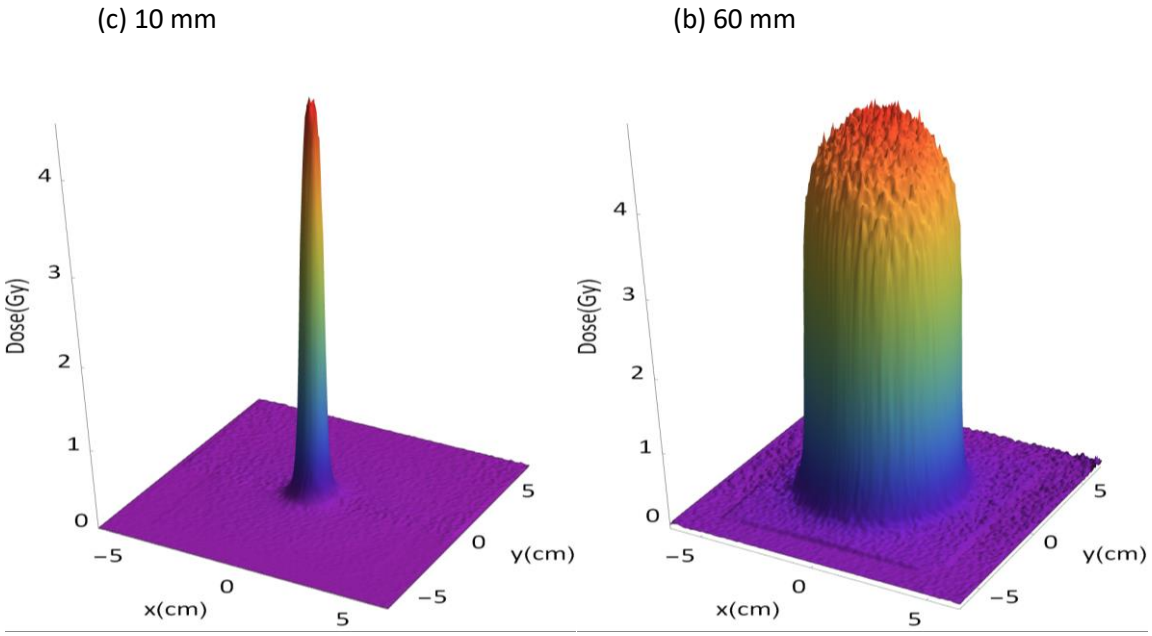

Figure 5-18. Dose maps of a 6 MV CyberKnife with cone size of (a) 5 mm (b) 7.5 mm (c) 10 mm and (d) 60 mm measured using 10 cm × 10 cm Al_2O_3:C,Mg films.

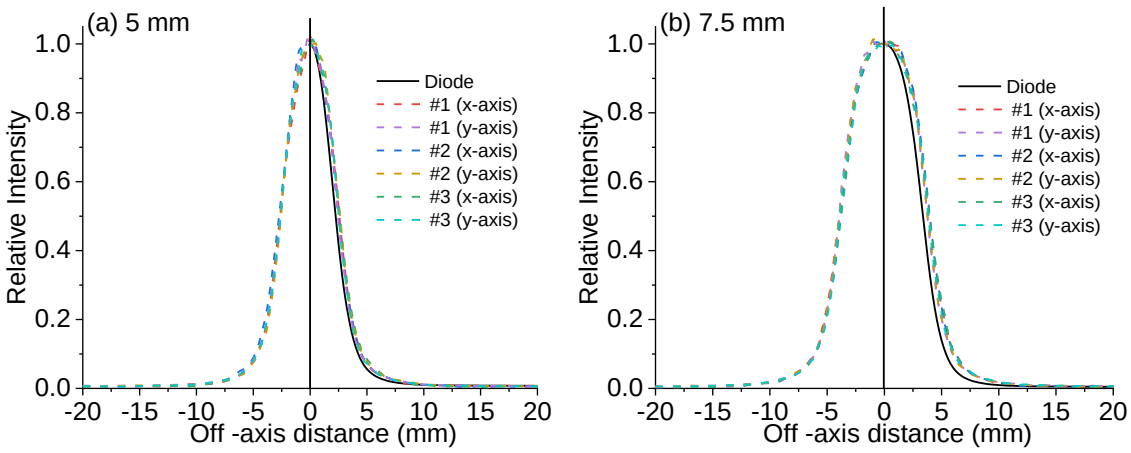

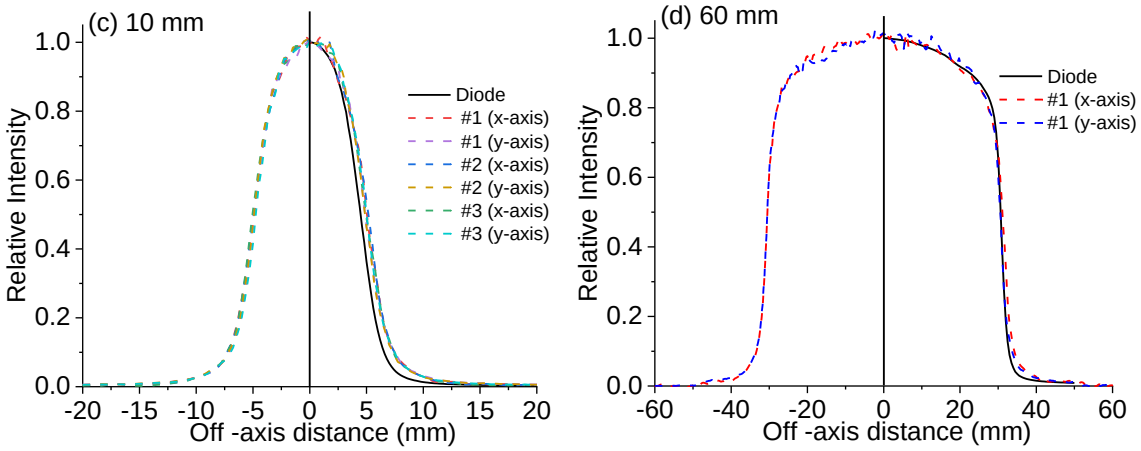

Figure 5-19. The lateral dose profiles measured using Al_2O_3:C,Mg films compared to those measured with a diode for (a) 5.0 mm, (b) 7.5 mm, (c) 10 mm and (d) 60 mm cone sizes. The OSL profiles shown are an average of 1 mm (4 consecutive profiles) at the central axis normalized to the mean signal over ROI 1 mm × 1 mm at the center.

Table 5-4. comparison of 80% - 20% penumbra measured with OSL films and diode. The uncertainties for the OSL films are the standard deviation between the x and y profiles from 3 films for each cone size.

Cone diameter (mm)	80% - 20% penumbra (mm)	
	Diode	OSL film
5	2.09 ± 0.1	2.10 ± 0.04
7.5	2.21 ± 0.1	2.28 ± 0.08
10	2.57 ± 0.1	2.74 ± 0.03
60	3.47 ± 0.1	4.46 ± 0.03

5.5.3 Output factor

The output factors were measured using the images from Section 5.5.2. Figure 5-20a shows the dose profiles of 1.0 mm in x and y direction measured at the center of the Al_2O_3:C,Mg films for cone sizes of 5.0 mm, 7.5 mm, 10 mm and 60 mm. As can be seen, the dose profiles are symmetrical, and the peak dose decreases with increasing field size. Figure 5-20b shows the dose profiles for different cone sizes and Figure 5-20b the output factors relative to the 60 mm cone size.

To calculate the output factors, the peak dose over the ROI 1 mm (4 pixels × 4 pixels) for each cone size was normalized to the 60 mm cone. The large difference in the output factor for 5.0 mm cone compared to other cone sizes which are not known. The output factors for the cone sizes >5.0 mm agree relatively well with the diode measurements. The overestimation of the output factor by the OSL films is still not clear and requires further investigations.

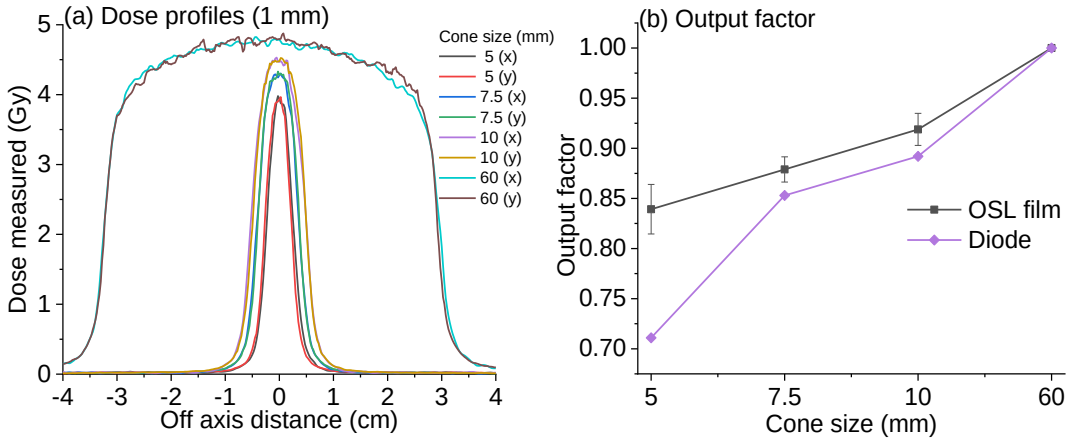

Figure 5-20. (a) Dose profiles of 1.0 mm measured at the center of the Al_2O_3:C,Mg films for cone sizes of 5.0 mm, 7.5 mm, 10 mm and 60 mm (b) Output factor relative to the 60 mm cone. The error bars represent the standard deviation of mean between the 3 film measurements.

5.5.4 Tissue Phantom Ratios (TPR)

To measure the TPR, 10 cm × 10 cm Al_2O_3:C,Mg films were irradiated using Accuray CyberKnife (Section 3.5.3) at 800 mm SAD at different depths with a total delivered dose of 2 Gy. Three films were irradiated at each depth for statistics. The films were placed at the same SAD and solid water phantoms were added in the top to increase the depth. The peak dose at each depth was then normalized to the depth of maximum dose of 1.5 cm to obtain the TPR.

Figure 5-21 shows the TPR measured using Al_2O_3:C,Mg films and compared to diode measurements. Each OSL data point is an average of 1.0 mm (4 pixels × 4 pixels) at the center of the film. The error bars represent the standard deviation of mean between the 3 film

measurements. As can be seen, the OSL measurements agree very well with the diode measurements within 1% at depths >10 mm.

The discrepancies in TPR below 10 mm may be due to position uncertainties of the detectors as the dose increases rapidly in that region as CPE does not exist in this region.

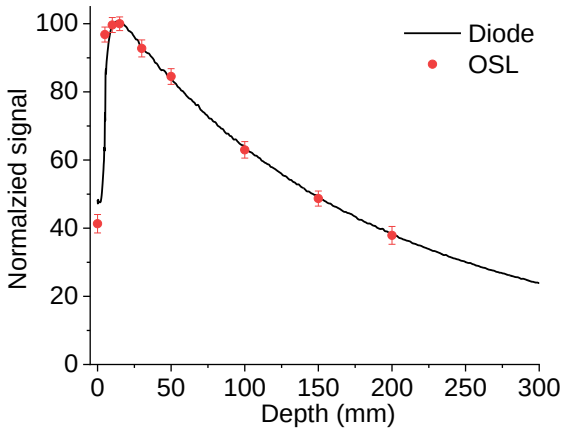

Figure 5-21. Accuray CyberKnife TPR measurements using Al_2O_3:C,Mg films and diode. Each OSL data point is an average of 1.0 mm (4 pixels × 4 pixels) at the center of the film. The error bars represent the standard deviation of mean between the 3 film measurements.

CHAPTER VI

TESTS OF 2D OSL DOSIMETRY IN MRI GUIDED RADIOTHERAPY

In this chapter, we investigate the application of OSL dosimetry in MRgRT. We performed tests using OSL detectors to test the angle dependence of irradiation and transmission. In addition to point measurements, we also investigated the application of OSL films for 2D dosimetry in MRgRT. We investigated the response of the OSL films in magnetic field by obtaining a dose response curve. We irradiated two treatment plans on OSL films and compared them to the data from treatment plan software (TPS). For this a custom gamma analysis algorithm was written in Mathematica. The algorithm was verified by irradiating a plan on a commercial MapCheck detector and comparing the gamma values obtained by its software and our algorithm.

6.1 Point detectors measurements

6.1.1 Dose response

The calibration curve of Mipox detectors was obtained in the Risø TL/OSL-DA-20 reader (Section 3.7). Al_2O_3:C (Mipox) samples (7 mm disc) were irradiated in Risø with irradiation times of 30 s, 60 s, 110 s, 170 s, 230 s and 300 s (3 samples for each irradiation) and readout. Figure 6-1 shows the response of the Mipox samples in Risø. The signal was then fitted using Equation (5-2). Table 6-1 shows the fitted parameters.

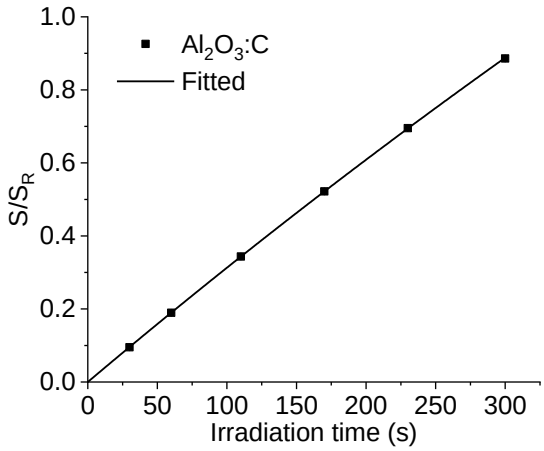

Figure 6-1. Calibration curve of Mipox, obtained using the Risø TL/OSL-DA-20 reader.

Table 6-1. Fitted parameters of the dose response functions for the OSL films shown in Figure 6-9.

Parameters	Al_2O_3:C
a	(5.66418 ± 0.267) Gy
b	(56.844 ± 2.8419) × 10^{-4} Gy/count

The response of Al_2O_3:C (Mipox) detectors in the magnetic field was determined by irradiating 6 sets of Mipox detectors (5 detectors in each set) in the MR linac with a static magnetic field of 0.35 T using a field size of 10.5 cm × 10.5 cm at 1.5 cm depth with doses from 0.5 Gy to 10 Gy as shown in Figure 6-2. Then, the samples were then read out using Risø. The responses of the detectors were then used to calibrate the dose rate of the Risø source. Figure 6-3 shows the dose delivered as a function of time of irradiation calculated using the calibration function (see Table 6-1). The data points were fitted with a linear function of which the slope was found to be 0.485. Thus, the dose rate of the Risø source is 48.5 mGy/s.

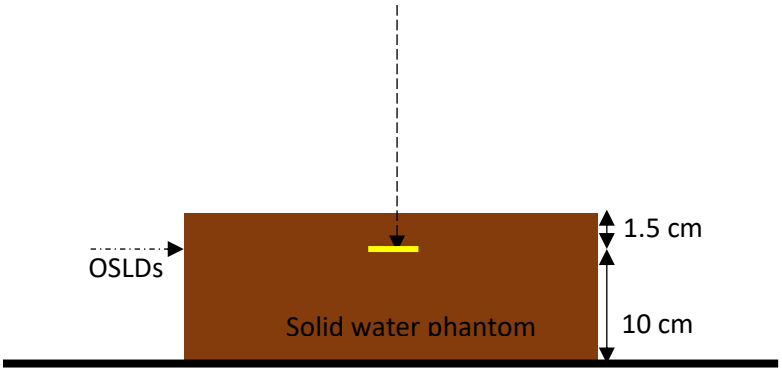

Figure 6-2. Dose response setup.

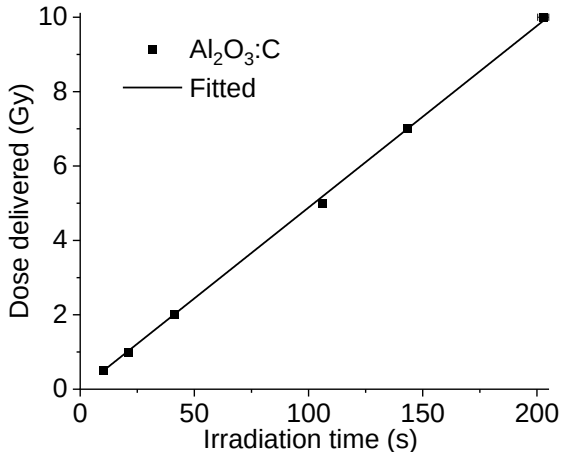

Figure 6-3. Calibration of Risø source. Each data point is the average of 5 samples, and the error bars represent the standard deviation of the mean of the samples.

6.1.2 Transmission measurements

Transmission measurements were conducted to determine the attenuation due to the Mipox detectors in magnetic field. For this, a package containing five Mipox detectors were placed at a depth of 0.5 cm and an additional package was placed at 1.5 cm depth as shown in Figure 6-4. The samples were irradiated with a total delivered dose of 2 Gy.

The dose measured by the detectors at 1.5 cm depth was (1.99 ± 0.03) Gy. The value after ± represents the standard deviation of the mean of the 5 detectors. The results show a

good agreement, within 1%, to the dose delivered and the dose measured by the Mipox detectors at 1.5 depth. This shows that the Mipox detectors, even though not water equivalent, do not introduce uncertainties to the absorbed dose and according to White et al. (2016) if the uncertainties are <1% no additional correction is required. The lower dose of the Mipox detector at depth 0.5 cm is due to the detector being at the build up region.

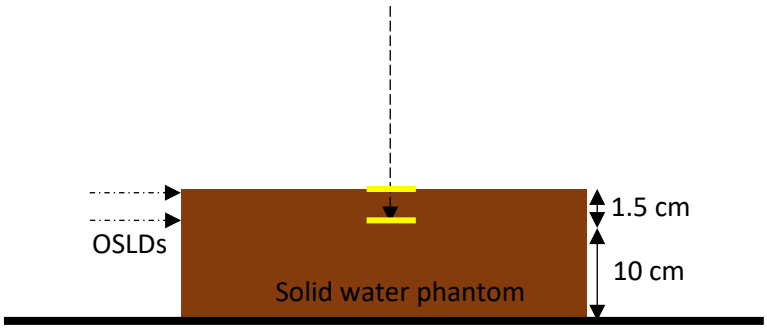

Figure 6-4. Transmission measurements setup.

6.1.3 Angular dependence

This test was performed to measure the response of Mipox samples at 90° and -90° angle of irradiation. For this test two packages of Mipox samples, each package containing 5 detectors, were irradiated at 1.5 cm depth with a total delivered dose of 2 Gy with samples at 90° and -90° as shown in Figure 6-5 and Figure 6-6.

Table 6-2 shows results from the Mipox detectors. The dose measured is the mean dose calculated from the 5 detectors from each package. The dose measured from the Mipox detectors for both orientations agrees within 1%, so no influence of magnetic field is observed.

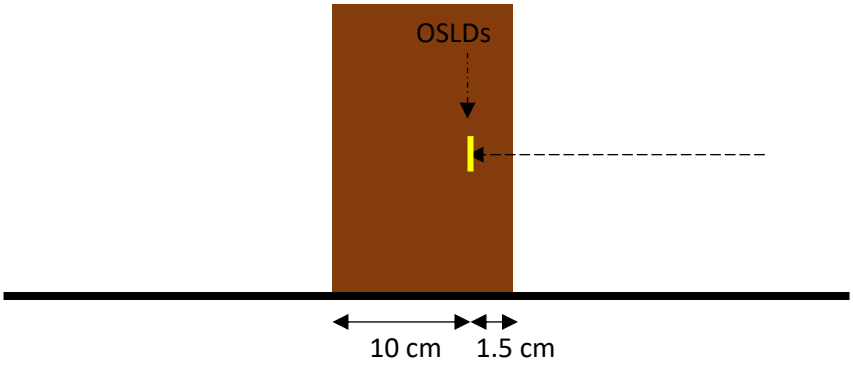

Figure 6-5 Angular dependence measurement setup in solid water phantom at +90° irradiation angle.

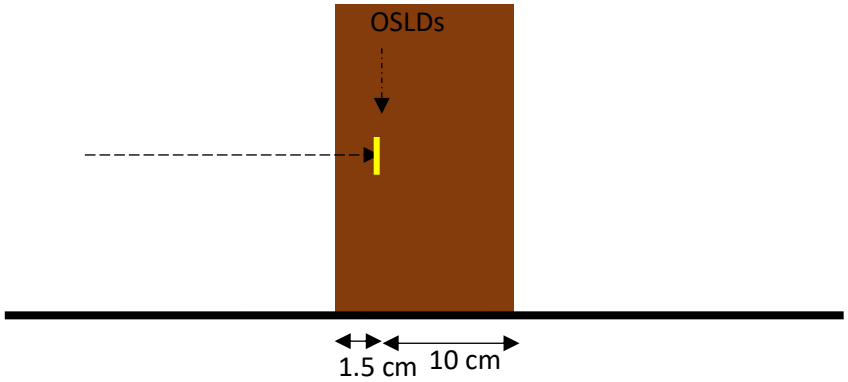

Figure 6-6. Angular dependence measurement setup in solid water phantom at -90° irradiation angle.

Table 6-3. OSL response at 90° and -90° irradiation angle.

Package	Dose delivered (Gy)	Angle (deg)	Depth (cm)	Dose measured (Gy)	%Diff
1	2	90	1.5	2.00 ± 0.03	0.2
2	2	-90	1.5	2.01 ± 0.03	0.4

To test additional irradiation angles, 5 packages of Mipox detectors were irradiated individually in a cylindrical phantom each with different irradiation angles of 0°, 45°, 90°, 270°, 315° as shown in Figure 6-7.

Figure 6-8 shows the response of the Mipox detectors to different irradiation angles. The dose increases by around 3% for a 90° irradiation and further increases to ~4% at 270°. These discrepancies may be due to the setup geometry. Nevertheless, the variation in the measured dose for different angle of irradiation was ~1.4%.

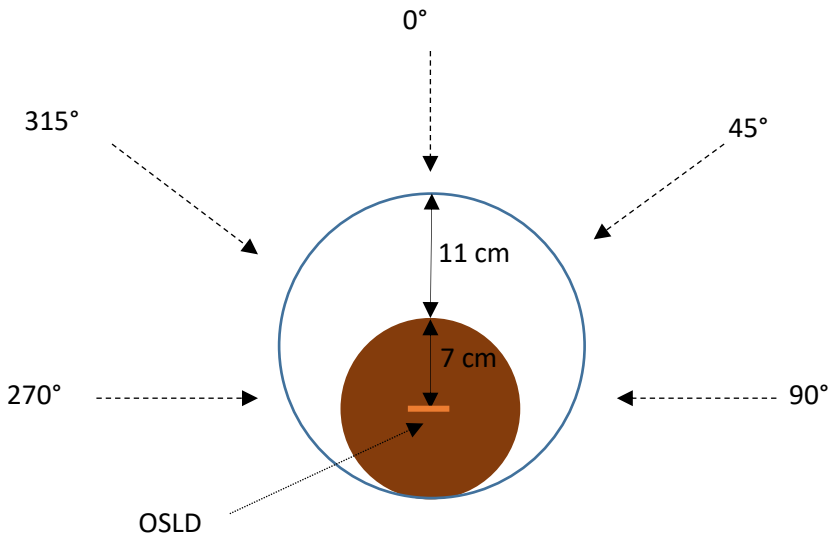

Figure 6-7. Angular dependence measurement setup in a cylindrical phantom.

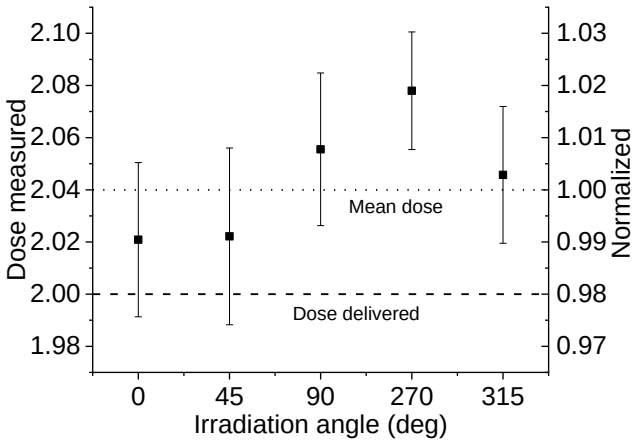

Figure 6-8. Angular reponse of Mipox detectors in 0.35 T magnetic field. Each data point is the average of five samples and the error bars represent the standard devaiation of the mean of the five samples.

6.2 Film measurements

6.2.1 Dose response

We determined the dose response for Al_2O_3:C and Al_2O_3:C,Mg films using the MR linac with static magnetic field of 0.35 T and ^{60}Co as the radiation source. The films were irradiated with 10.5 cm × 10.5 cm flat field at a depth of 5.0 cm for doses from 0.1 Gy to 10 Gy. After readout the images were then reconstructed using the Tikhonov-L2 algorithm.

To compare the image uniformity for two films at different doses, we calculated the signal profiles (average of 1 cm) at the center of the image in both x and y axes. The dose response curve was calculated using the average signal over a central region of interest (ROI) 2.0 cm × 2.0 cm (80 pixels × 80 pixels). Figure 6-9a and b show two overlapping signal profiles for each dose calculated in perpendicular directions (x and y directions). As can be seen the x and y-profiles overlap at any dose level.

The fitted parameters for the dose response curves of all three films are shown in Table 6-4. Al_2O_3:C film has about 40% higher response than the Al_2O_3:C,Mg film. In addition, Al_2O_3:C,Mg films has ~50% better signal-to-noise ratio (SNR = S/3σ) than Al_2O_3:C films. The SNR for both the films irradiated with 2 Gy, the SNR for Al_2O_3:C film was 9 and for Al_2O_3:C,Mg film was 18. This is due to less correction required for pixel bleeding correction for Al_2O_3:C,Mg film than Al_2O_3:C.

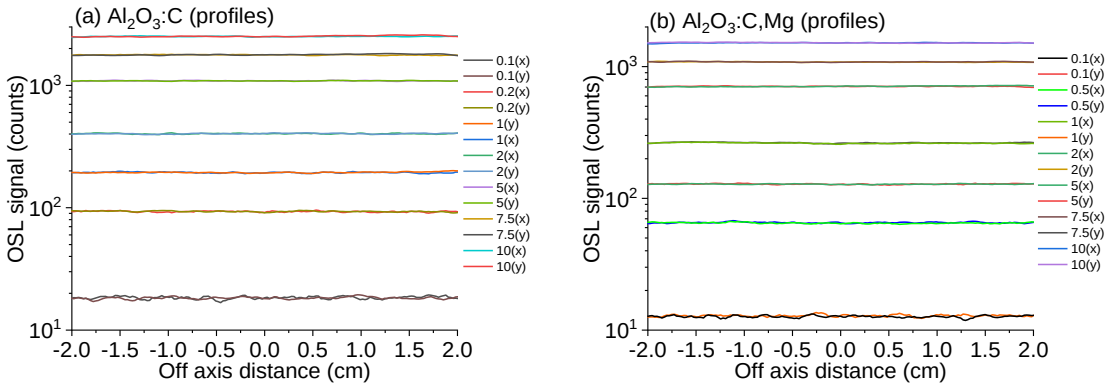

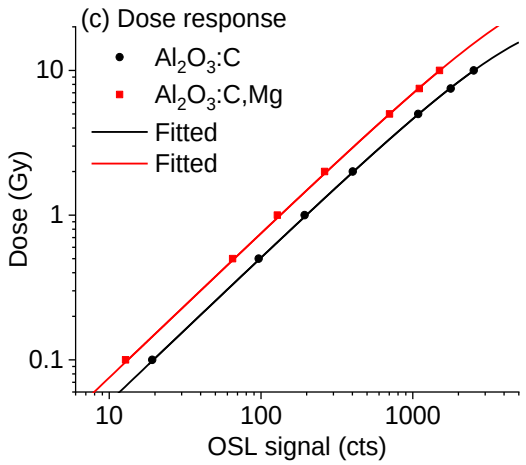

Figure 6-9. Dose response using MR lianc with static magnetic field of 0.35 T (depth: 5.0 cm, field size: 10.5 cm × 10.5 cm, SSD: 100 cm) for 5.0 cm × 5.0 cm films of Al_2O_3:C and Al_2O_3:C,Mg. (a-b) Signal profiles (average of 40 rows spanning 1.0 cm) in both x and y-directions for all doses; (c) dose response curve obtained using the OSL films where each data point is the average of two films signal calculated over 2.0 cm × 2.0 cm (~80 pixels × 80 pixels) around the central axis.

Table 6-4. Fitted parameters of the dose response functions for the OSL films shown in Figure 6-9.

Parameters	Al_2O_3:C	Al_2O_3:C,Mg
a	(23.53 ± 1.09) Gy	(42.63 ± 5.44) Gy
b	(2.18 ± 0.12) × 10^{-4} Gy/count	(1.77 ± 0.25) × 10^{-4} Gy/count

6.2.2 Gamma analysis of treatment plans

For this test 10.0 cm × 10.0 cm films of Al_2O_3:C and Al_2O_3:C,Mg films were irradiated with two different treatment plans using the MR linac with a static magnetic field of 0.35 T at a depth of 5.0 cm.

Figure 6-10 and Figure 6-12 shows the dose maps of the IMRT plans from the TPS and the Al_2O_3:C and Al_2O_3:C,Mg films. As can be seen, the OSL images look identical to the IMRT treatment plans. The gamma analysis algorithm was applied to both the treatment plans and the results are shown in Figure 6-11 and Figure 6-13.

Figure 6-11a and Figure 6-13a show the OSL images from Al_2O_3:C and Al_2O_3:C,Mg films irradiated with the two treatment plans along with the regions that fail the gamma analysis

criteria of 3% and 3 mm. As can be seen, the regions with high dose pass the gamma analysis, whereas the region that fails the criteria are low dose regions with gradient. We believe that at low dose regions, the noise is higher, which causes the points to fail. Figure 6-11b and Figure 6-13b shows the dose profiles at the center of the Al_2O_3:C and Al_2O_3:C,Mg films and IMRT plans. The OSL dose profiles from both materials agree very well to the IMRT plan.

Table 6-5 shows the summary of the gamma analysis of the two treatment plans using OSL films. The results show that using a gamma criteria of 3% - 3 mm and 2% - 2 mm passing rate of 98% and 95% respectively for both film types irradiated with IMRT plan I. However, for IMRT plan II the gamma criteria of 3% - 3 mm show a passing rate of ~ 96% and gamma criteria of 2% - 2 mm show a passing rate of only ~ 88%. This difference in the passing rate of two plans with tighter gamma criteria is probably due to the noise in the images. The IMRT plan II is irradiated with a lower dose and with a larger dose gradient. As the gamma criteria are increased the lower dose regions in the images, which is around the edges, begins to fail as these are low dose regions with higher uncertainties. In addition, these uncertainties can be attributed to calibration uncertainties and image noise. This noise in the image, however, can be lowered with scanning the films multiple times at the expense of readout times and with a better calibration function using multiple films calibration uncertainties can be reduced.

Nevertheless, the gamma analysis studies show that OSL films show good agreement with the TPS data. Thus, OSL films show no response to magnetic field and can be potentially used as a 2D dosimeter in MRgRT.

(a) IMRT plan

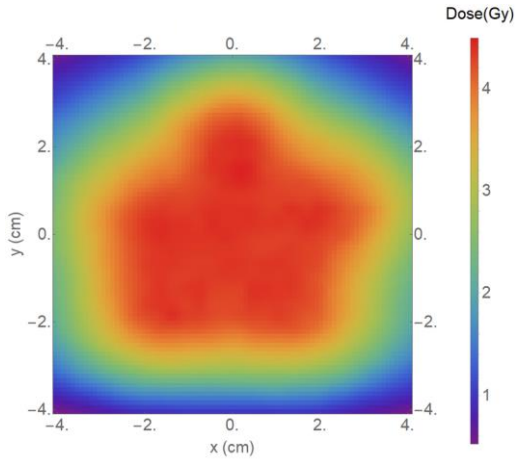

(b) Al_2O_3:C

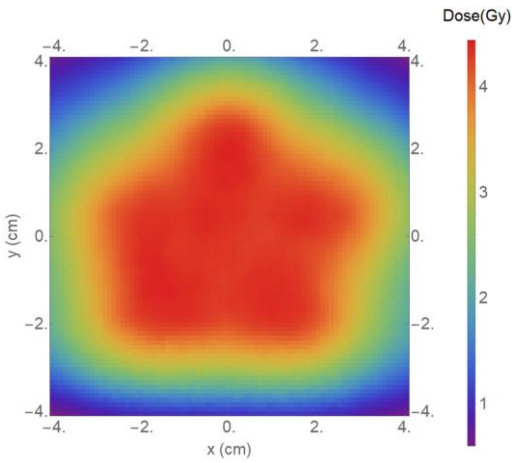

(c) Al_2O_3:C,Mg

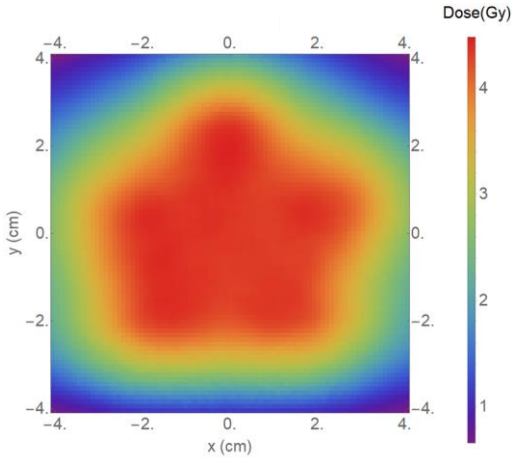

Figure 6-10. (a) Images of the IMRT plan. OSL images from (b) Al_2O_3:C and (b) Al_2O_3:C,Mg films irradiated with the IMRT treatment plan.

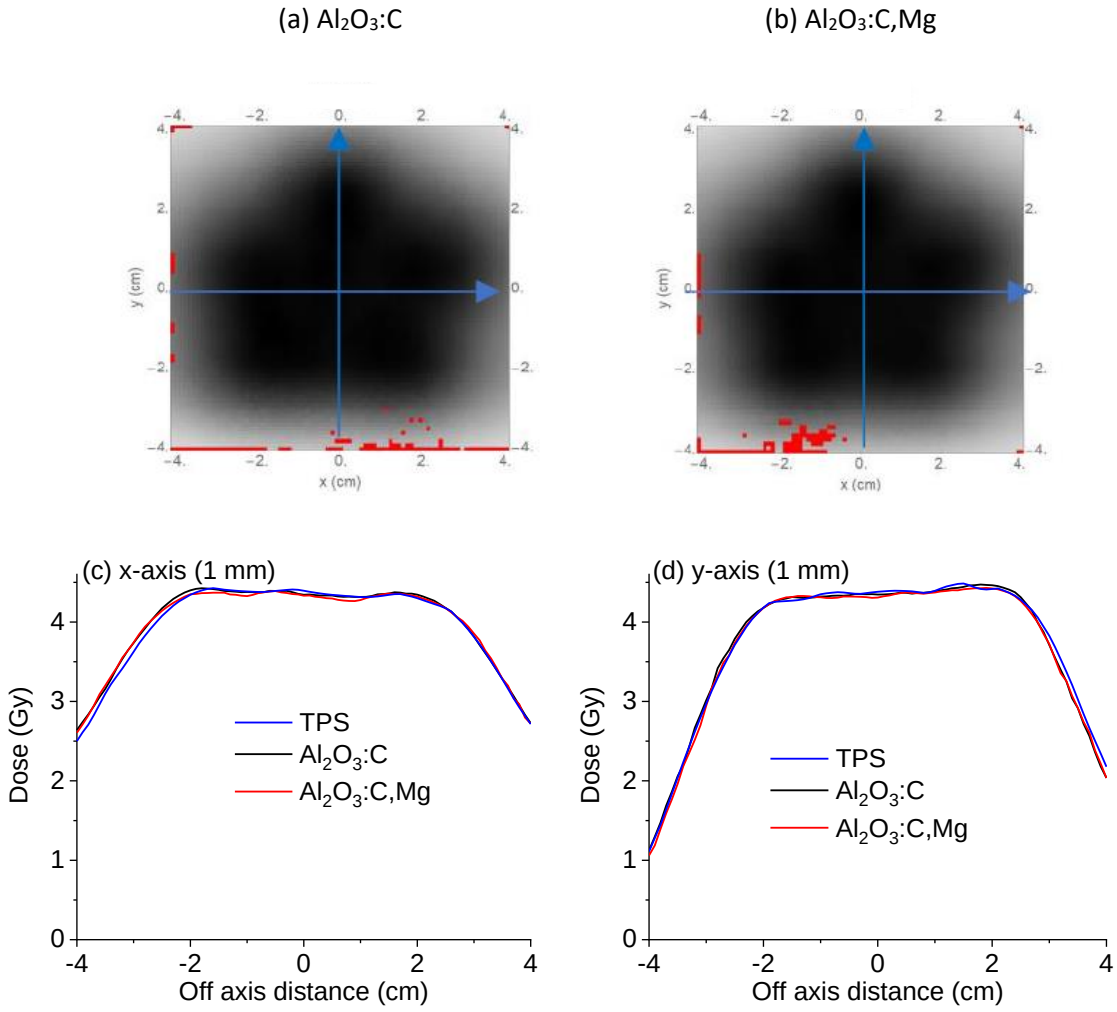

Figure 6-11. Gamma analysis results of the IMRT treatment plan irradiated on (a) Al_2O_3:C and (b) Al_2O_3:C,Mg films obtained using 3% - 3 mm criteria. Red pixel indicates pixel with points failing the gamma criteria. Comparison of central dose profiles of images of IMRT plan with Al_2O_3:C and Al_2O_3:C,Mg films (a) x-axis and (b) y-axis.

(a) IMRT plan

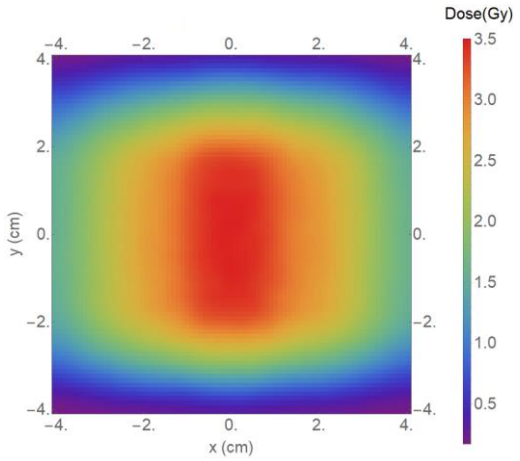

(b) Al_2O_3:C

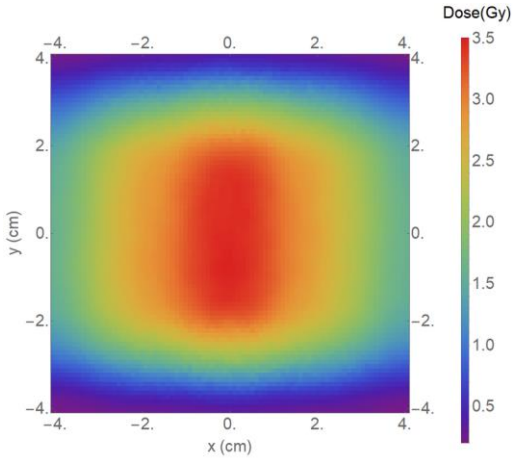

(c) Al_2O_3:C,Mg

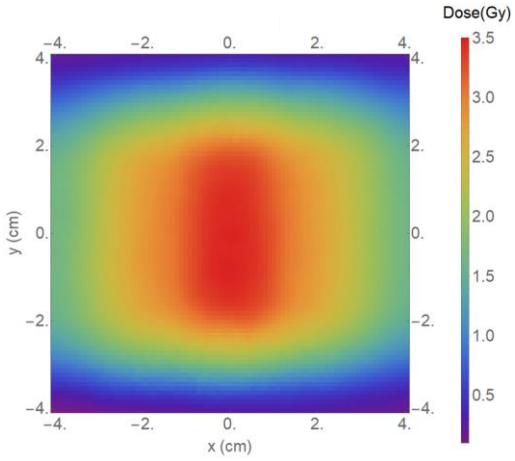

Figure 6-12. (a) Images of the IMRT plan. OSL images from (b) Al_2O_3:C and (c) Al_2O_3:C,Mg films irradiated with the IMRT treatment plan.

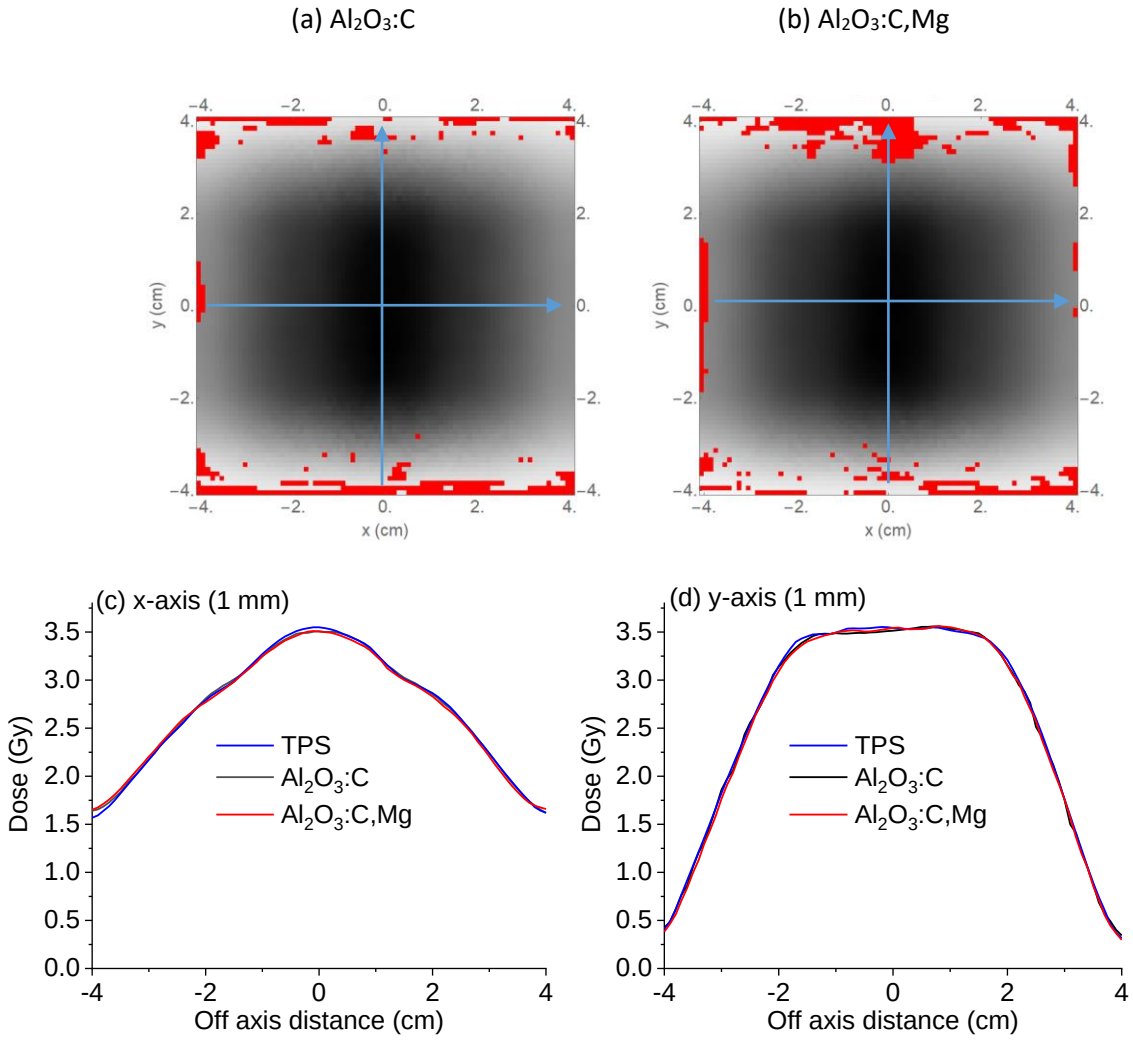

Figure 6-13. Gamma analysis results of the IMRT treatment plan irradiated on (a) Al_2O_3:C and (b) Al_2O_3:C,Mg films obtained using 3% - 3 mm criteria. Red pixel indicates pixel with points failing the gamma criteria. Comparison of central dose profiles of images of IMRT plan with Al_2O_3:C and Al_2O_3:C,Mg films in (a) x-axis and (b) y-axis.

Table 6-5. Summary of gamma anlysis of the two treatment plans using Al_2O_3:C and Al_2O_3:C,Mg films.

	Plan I		Plan II	
Material	**3% - 3 mm**	**2% - 2 mm**	**3% - 3 mm**	**2% - 2 mm**
Al_2O_3:C	98%	95%	96%	88%
Al_2O_3:C,Mg	98%	95%	93%	80%

CHAPTER VII

FEASIBILITY STUDIES OF 2D OSL DOSIMETRY USING MgB_4O_7

This chapter demonstrates the feasibility of 2D dosimetry using films prepared using MgB_4O_7:Ce,Li and identify current limitations. We investigated the performance of the films in 2D dosimetry using the 2D OSL system and compare them to the results from Al_2O_3:C and Al_2O_3:C,Mg films including dose response, sensitization and dark fading. In addition to dosimetric performance, we investigated the basic luminescence properties of MBO including luminescence lifetimes, phosphorescence, bleaching and readout parameters.

7.1 Comparison of raw images of MgB_4O_7:Ce,Li and Al_2O_3 films

10 cm × 10 cm MBO, Al_2O_3:C and Al_2O_3:C,Mg films were irradiated in air using the 90 kVp X-ray source with a total delivered dose of ~0.76 Gy. All the films were read out using the 2D OSL system (see Section 3.6) with the same readout conditions and with scanning speed of 327 μs bin^{-1}.

Figure 7-1 shows the raw (uncorrected) images from MBO, Al_2O_3:C and Al_2O_3:C,Mg films. In the images, the effect of PMT light collection efficiency can be observed. In addition, pixel bleeding is observed in both Al_2O_3:C (Figure 7-1b) and Al_2O_3:C,Mg (Figure 7-1b) films due to the slow luminescence lifetime of F-center (~ 35 ms). The pixel bleeding is less in Al_2O_3:C,Mg film due to larger relative concentration of F^+ centers compared to Al_2O_3:C. In contrast to Al_2O_3 films, the MBO image essentially shows no pixel bleeding (Figure 7-1a).

Figure 7-2a show the signal profiles (average of 10 rows) in the scan direction (x-axis) normalized to the average signal at center calculated over ROI (5 mm × 5 mm). The Al_2O_3 films show slow rise at the beginning (~pixel 110) and a decay end of the film (~pixel 900). The relative contribution of pixel bleeding can be observed at the end of the film. MBO however, shows both a fast rise at the beginning of the film and a sharp drop at the end of the film, which demonstrates the improved imaging performance due to the fast luminescence center of Ce^{3+}.

Figure 7-2b shows the signal profiles (average of 10 columns) in the sub-scan direction (y-axis) normalized to the average signal at center calculated over ROI (5 mm × 5 mm). There is no pixel bleeding present, but there is signal is present at the end of the film (~pixel 900), which is probably due to phosphorescence associated with shallow traps. This can possibly be corrected using the image reconstruction algorithm. Ahmed (2016) have already showed that both Al_2O_3 films have slow luminescence life time components of ~60 s.

(a) MBO

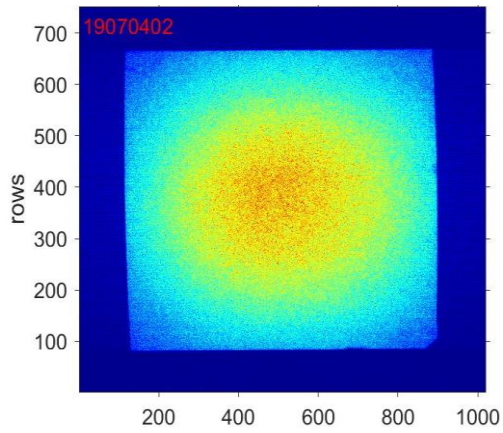

(b) Al_2O_3:C

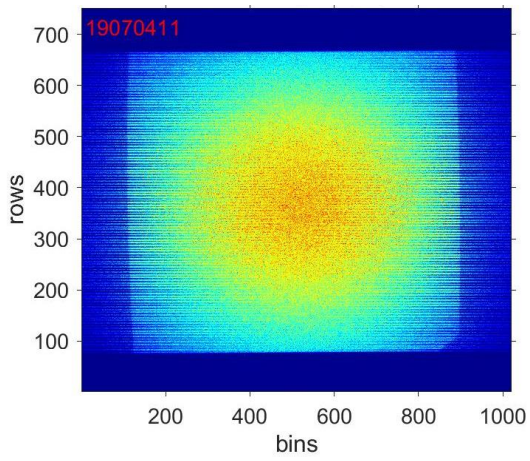

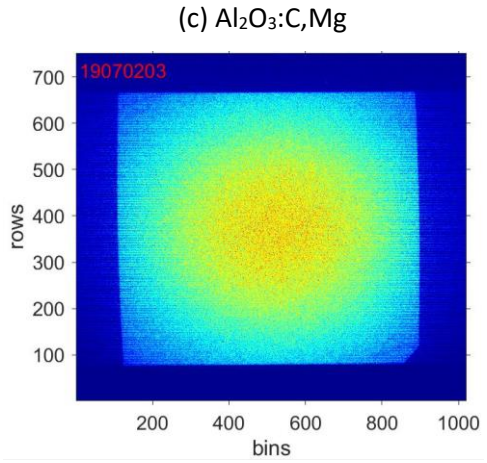

Figure 7-1. Raw OSL images from 10 cm × 10 cm OSL films (a) MBO (b) Al_2O_3:C (c) Al_2O_3:C,Mg irradiated using 90 kVp x-ray source in air with ~0.76 Gy total dose.

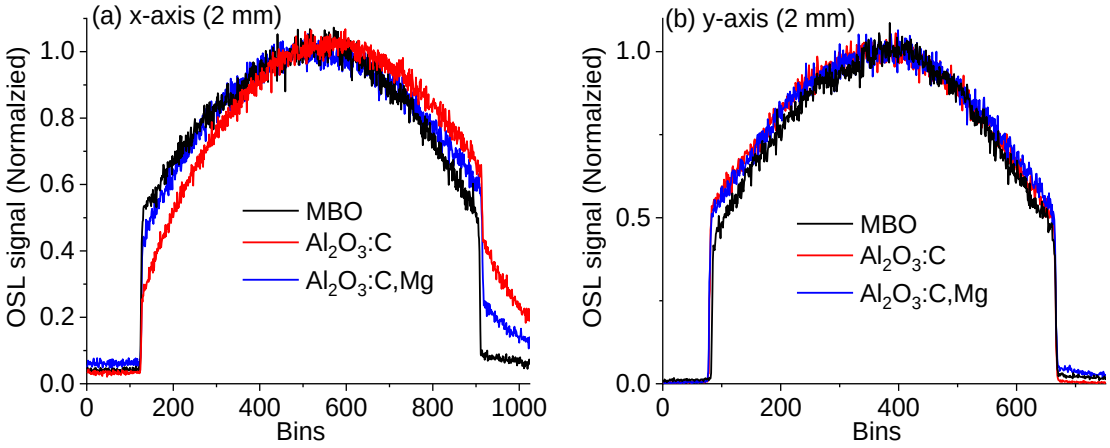

Figure 7-2. (a-b) OSL signal profiles (average of 10 even rows spanning ~2 mm) in both x and y-directions normalized to the mean signal calculated over ROI (5 mm × 5 mm) at the center of the image.

7.2 Basic luminescence properties of MBO

To understand the performance of the MgB_4O_7:Ce,Li films, some of its luminescence properties such as OSL signal depletion, luminescence lifetime components and phosphorescence signals, were investigated.

7.2.1 OSL signal depletion

This test was done to characterize the OSL signal depletion of the MBO films after each readout. This test gives an idea about the remaining signal which can be either used to re-read the film or scan it multiple times to improve the image SNR. For this test, MBO, Al_2O_3:C and Al_2O_3:C,Mg films were irradiated in air using the 90 kVp x-ray source with a with total exposure of ~ 0.76 Gy and readout nine times in sequence, without irradiation, using the 2D OSL system. The images were reconstructed using the Least Squares image reconstruction algorithm (see Section 7.4 for MBO correction).

Figure 7-3 shows the comparison of OSL signal (ROI 1 cm × 1 cm) as a function of number of readout for MBO, Al_2O_3:C and Al_2O_3:C,Mg films. The signal depletion for all the three film types was found to be ~25 – 30% per scan. Thus, there is plenty of additional signal remaining in the film after the first read out which can be either read out again in the future or accumulated with multiple readouts to improve the image SNR. In addition, the results show that MBO is bleached more slowly than the Al_2O_3 films using the green laser. This can be improved by using shorter wavelengths or higher stimulation intensities.

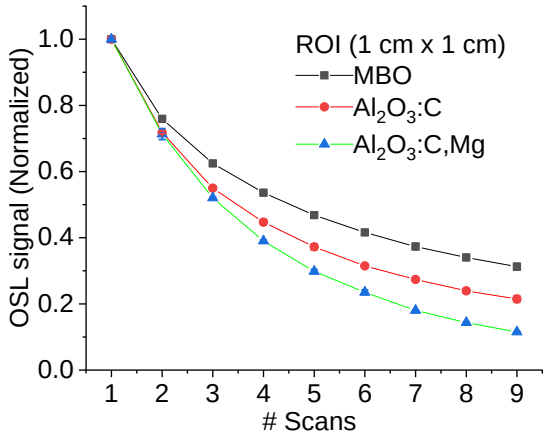

Figure 7-3. Signal depletion (ROI 1 cm × 1 cm) with 9 consecutive scans of MBO, Al_2O_3:C and Al_2O_3:C, Mg films with 100% laser power normalized to first scan. Each data point is average of measurements of 3

films of each type. The error bars represent the standard deviation between the 3 measurements. The depletion was then fitted with a double exponential.

To compare signal depletion with shorter wavelengths, two sets each set with 3 MBO samples (7mm discs) were irradiated with ~2.1 Gy in Risø. The first set was readout using blue LED and the second set was readout using green LED.

Figure 7-4 shows the OSL signal, normalized to its initial signal, measured with both blue and green LEDs. As can be seen the rate of signal depletion is much faster with blue stimulation. This means that with fewer readouts we can collect more signal improving the signal-to-noise ratio in the image.

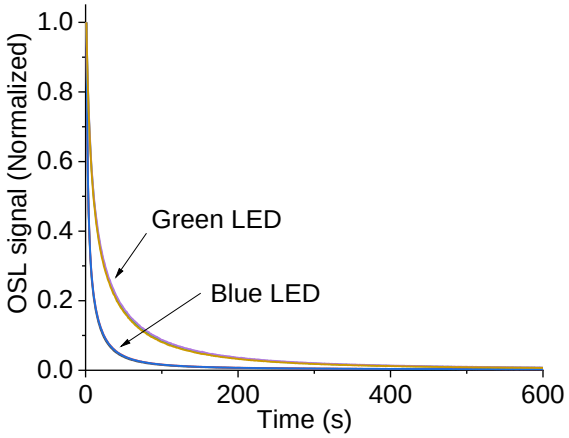

Figure 7-4. OSL signal from MgB_4O_7:Ce,Li samples (7 mm discs) irradiated with 2.1 Gy and read out immediately after irradiation using blue and green LED.

7.2.2 Reusability

To test the reusability of the MBO film a 7 cm × 7 cm MgB_4O_7:Ce,Li film previously irradiated with dose of ~ 10 Gy was bleached overnight in the bleaching unit (Section 3.2) and read using the 2D OSL system.

Figure 7-5a show the raw image of the bleached MBO film. The film in the central part of the scan area is clearly visible. A better assessment of the background signal can be made by analyzing the signal profiles. Figure 7-5b shows the dose profiles (average of 300 rows spanning

5 cm) in both x and y direction from the MBO image which was calculated using the calibration curve presented later in Section 7.5.1. The average film background was found to be only 0.02 counts bin^{-1}, which is equivalent to less than 0.5 mGy.

To more precisely demonstrate the possibility of bleaching the MBO films, MBO samples (7 mm discs) were irradiated with doses between 0.69 Gy, 2.07 Gy, 6.9 Gy and 20.7 Gy (three samples for each dose) in the Risø reader. The samples were then readout and bleached overnight in the bleaching unit. This sequence was repeated five times for reproducibility.

Figure 7-6 shows the OSL signal from bleached MgB_4O_7:Ce,Li samples after the fifth irradiation compared to the OSL response of 3 samples irradiated with 0.69 Gy (beta). As can be seen, all MBO samples with previous dose history can be bleached. The background equivalent dose is <0.5 mGy, if we consider the initial intensity of the OSL curve.

In either case, using MBO for 2D dosimetry or point measurements, the background equivalent dose is less than 0.5 mGy, which is negligible compared to the typical doses used in radiation therapy.

(a) Bleached image (b) Signal profiles

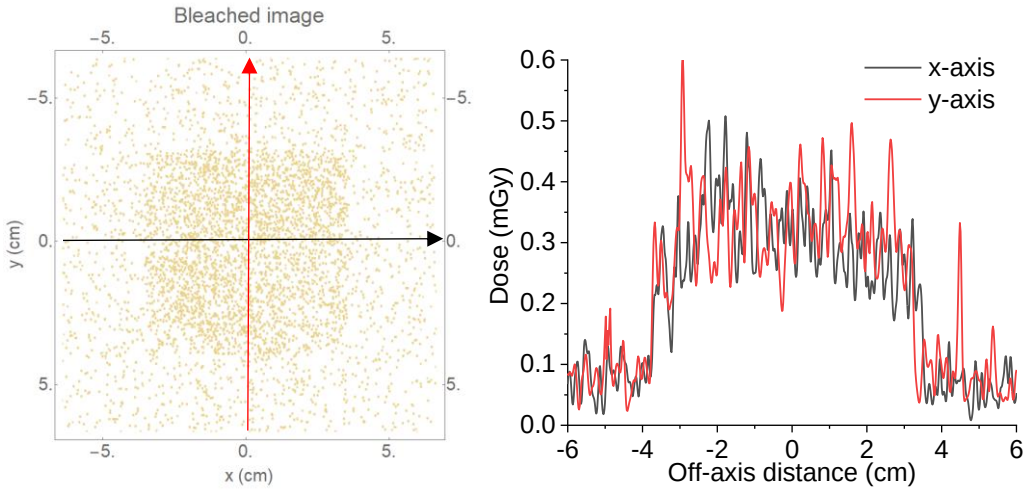

Figure 7-5. (a) Raw OSL image from a bleached 7 cm × 7 cm MBO film previously irradiated with dose of ~ 10 Gy. The image was processed using 5 pixels × 5 pixels Wiener filter to reduce noise.(b) Signal profiles (average of 300 rows spanning 5 cm) in both x and y direction from the MBO image in (a).

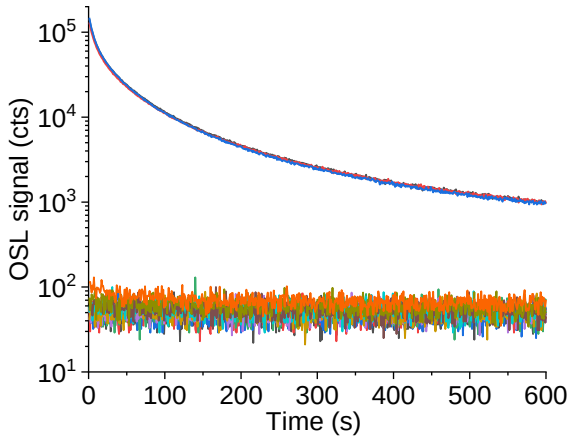

Figure 7-6. OSL signal from bleached samples previously irradiated with doses from 0.69 Gy, 2.07 Gy, 6.9 Gy and 20.7 Gy (beta) compared to the response of 3 samples irradiated with 0.69 Gy (beta). The samples were repeatedly irradiated and bleached 5 times and the bleached signal shown here is after the last run.

7.2.3 Luminescence lifetime components

The luminescence lifetime components of MBO was characterized using Time-Correlated Single Photon Counting (TCSPC) (Section 3.7). For this test MBO, Al_2O_3:C and

Al_2O_3:C,Mg samples were irradiated with ~0.35 Gy. The luminescence was measured using various long and short stimulation pulses. For short stimulation, the luminescence was measured for 200 s using 1 μs and 10 μs blue LED pulses every 50 μs and 500 μs. For long stimulation, the luminescence was measured for 200 s using 0.1 ms and 1 ms blue LED pulses every 5 ms and 100 ms. The data were analyzed using the PTanalyse software (DTU Nutech, Risø Campus, Denmark) with 0.512 μs, 1.024 μs, 8.192 μs and 1310 μs bin widths.

Figure 7-7 shows the OSL response of the samples at same stimulation time scale. The LED response is also included, as the LED also had a slow decay which affects the luminescence lifetime of the samples. In all cases, all the materials show fast response due to presence of fast luminescence centers, Ce^{3+} in the case of MBO and F^+-centers in the case of Al_2O_3. Figure 7-7 shows that after the LED pulse Al_2O_3:C has a 35 ms decay component associated with the F-centers, and Al_2O_3:C,Mg has an additional (2.4 ms) component due to shallow traps below room temperature. The additional high offset is due to shallow traps above room temperature (Denis et al., 2011a). In the case of MBO, the short lifetime components immediately after LED is off is due to shallow traps below room temperature and luminescence components in ~0.5 – 100 ms and the offset due to shallow traps above room temperature.

The results demonstrate that MBO is a better candidate for 2D dosimetry using laser scanning in terms of luminescence lifetimes. The contribution from shallow traps can possibly be corrected by the pixel bleeding algorithm. The lifetimes calculated for different acquisition parameter varied and thus, the lifetime components of MBO films could not be determined. This indicates that the shallow traps exhibit distribution of activation energies.

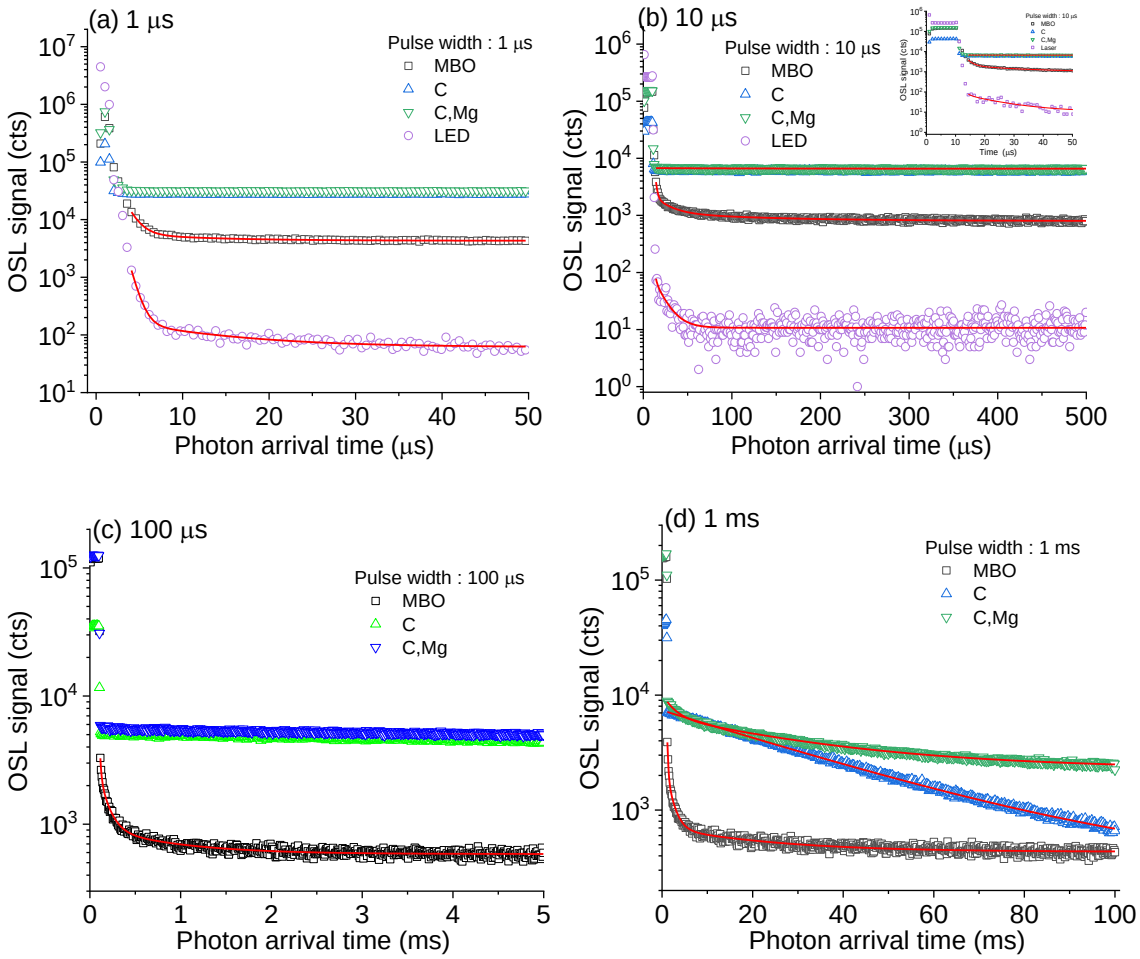

Figure 7-7. OSL response of Al_2O_3 and MgB_4O_7 films to (a) 1 μs, (b) 10 μs, (c) 100 μs, and (d) 1 ms LED pulse as a function of photo arrival time measured using Time-Correlated Single Photon Counting (TCSPC).

In addition to the Risø measurements, the phosphorescence lifetimes were measured at room temperature using the lifetime setup (see Section 3.2) which uses a green laser. This test was done to obtain relevant luminescence lifetimes of MBO films that can be used in the phosphorescence bleeding algorithm. Three film samples of each film type (7 mm diameter) were irradiated with ~ 20 Gy beta dose. The data acquisition was performed in time scale of 327.68 μs integration time to measure the phosphorescence signal from 0 – 1.7 s, and accumulating 2000 scans (2000 laser pulses).

The phosphorescence signal was found to have two components with lifetimes of ~ 4.5 ms and ~93 ms, plus a constant background probably due to a component with longer lifetime (Figure 7-8). The signals were fitted with a double exponential function of type:

$$I = y_0 + \sum_{i=1}^{2} A_i \exp\left(-\frac{t}{\tau_i}\right) \qquad \textbf{(7-1)}$$

where τ_i's are the measured lifetimes.

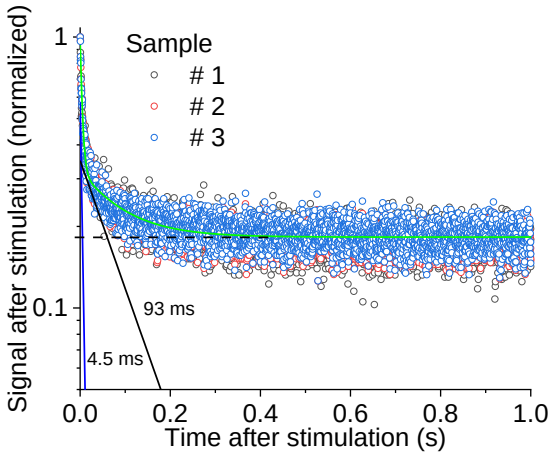

Figure 7-8. Phosphorescence lifetime measurement from three MgB_4O_7:Ce,Li samples (7 mm discs). The measurements were performed using the lifetime setup. Three samples, irradiated with ~10 Gy beta dose, were used for each measurement. The signal was measured with 327.68 µs integration time and ~2000 scans were accumulated.

7.2.4 Phosphorescence signal

In addition to the photo transferred phosphorescence signal, there is also a phosphorescence signal immediately after irradiation emitted at room temperature. To characterize it, five sets each with three 7 mm MBO samples were irradiated with different doses in the Risø reader and read out (LED off) immediately after irradiation. The phosphorescence signal was measured for an hour post irradiation for each sample. Three samples were irradiated with same dose for statistics.

Figure 7-9a show the phosphorescence signal from the MBO samples irradiated with different doses. It was found that MBO samples have shallow traps emissions at room temperature and is proportional to the dose delivered. This signal decrease exponentially with time.

Figure 7-9b shows the relative phosphorescence intensity after irradiation, normalized to the initial OSL intensity during readout. The error bars indicate the standard deviation between the three samples used for each dose. The phosphorescence signal from the MBO samples decreases to <1% in within 15 minutes post irradiation for all the doses delivered. The phosphorescence signal is ~10%, for the samples irradiated with 500 s beta dose, compared to the initial intensity of the OSL signal following readout.

The results indicate that the phosphorescence signal post irradiation depletes to <1% of the initial OSL signal after readout within 15 minutes. Thus, MBO samples can be read out 15 minutes after irradiation.

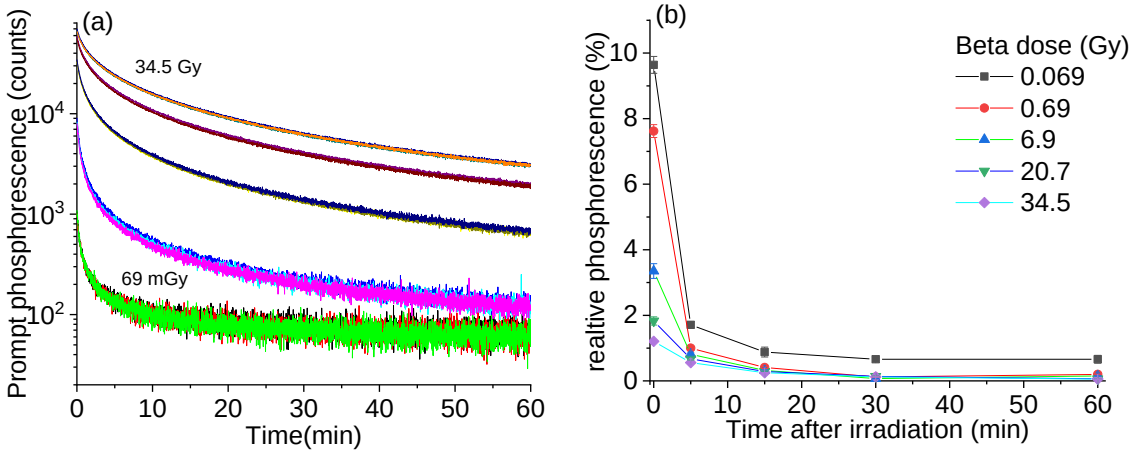

Figure 7-9. (a) Phosphorescence signal from MBO samples immediately after irradiation with beta doses of 0.069 Gy – 34.5 Gy. (b) Phosphorescence signal, measured at different times post-irradiation, relative to the initial OSL intensity. Each data point is average of the 3 samples and the error bars represent the standard deviation between the 3 samples.

7.3 Influence of scan speed

The 2D OSL system was built and optimized for Al_2O_3:C and Al_2O_3:C,Mg with the scan speed or pixel dwell time of 327 μs bin^{-1}. However, the scan speed can be increased in the case of MBO. In addition, with faster scanning speeds the contribution pf phosphorescence single from the shallow traps in MBO can be minimized or eliminated, and thus no additional image correction would be needed.

For this test, five 3 cm × 3 cm MBO films pieces were irradiated with a total dose of ~ 55 Gy in the 90 kVp x-ray source and read individually in the 2D OSL system with scanning speeds of 20 μs, 40 μs, 81 μs, 163 μs, and 327 μs. Figure 7-10a shows the signal profiles (average of 2 mm at center) from the images obtained with different scanning speeds. As can be seen the OSL signal from the film decreases with decreasing scanning speed, but so does the phosphorescence signal. This loss of signal can be compensated by accumulating signal from multiples scans of same film without increasing readout time. Therefore, to test this method, the same films were also scanned multiple times with same scanning speeds for speeds below 327 μs.

Figure 7-10b shows signal profiles from the MBO films scanned with different speeds multiple times added to obtain same integration time per pixel as with scanning speed of 327 μs. When the signal from multiple scans were summed the background phosphorescence signal decreases by ~80% and the pixel bleeding decreases by 60% when scanned with 20 μs scanning speed compared to 327 μs. As can be seen the signal with lower scanning speeds is comparable to that of 327 μs but, with less relative contribution from the phosphorescence signal.

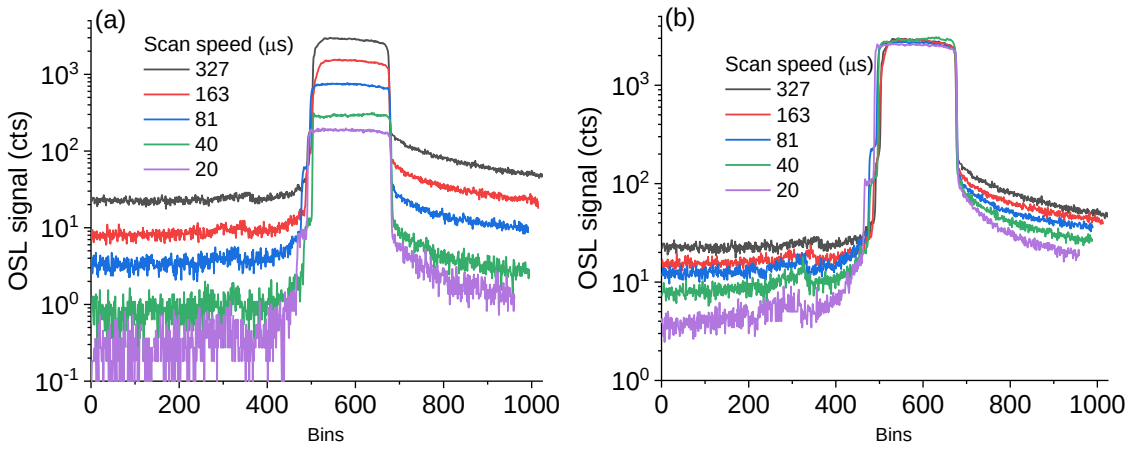

Figure 7-10. (a) OSL signal profiles from 5 pieces of 3 cm × 3 cm MBO film irradiated with a total dose of ~ 55 Gy scanned with scanning speeds of 20 μs, 40 μs, 81 μs, 163 μs, and 327 μs. Each signal profile is an average of 2 mm. The signal profiles are from raw images before any correction. (b) OSL signal profiles after accumulating signals from multiple scans of the same films scanned with scanning speeds of 20 μs, 40 μs, 81 μs, 163 μs, and 327 μs.

7.4 Image corrections

In addition to the system corrections, which are the same used in the image reconstruction algorithm of Al_2O_3 films, MBO also requires pixel bleeding correction because of the contribution from the two phosphorescence components 5 ms and 80 ms.

7.4.1 Background phosphorescence

The background phosphorescence, observed in the MBO images (see Section 7.1), is the signal present in the OSL image before the laser hits the film. It is originated from the slow phosphorescence of previously scanned rows. This contribution can be corrected by analyzing the signal measured at the beginning of each row, where no film present. Its intensity depends on the scanning speed, but in the current conditions it is characterized at scanning speed of 327 μs. For this test 3 pieces of MBO films with same width of 2 cm but increasing lengths of 3 cm,

6 cm and 9 cm were irradiated with 90 kVp x-ray source in air with ~0.67 Gy total dose. The films were then read out individually in the 2D OSL system.

Figure 7-11a shows a series of images of MBO film with lengths 3, 6 and 9 cm. Figure 7-11b shows signal profiles (average of 50 rows in one direction only, spanning 100 rows) at the center of each of the images. The signal at the beginning of the film is the phosphorescence signal which increase with increasing film size which is due to the lifetime of phosphorescence signal being longer than the time spent in one row. The signal at the end of the film is phosphorescence bleeding due to slow luminescecne lifetimes components of the film (see Section 7.2.3).

To understand the nature of the background phosphorescence signal, the signal was normalized to the mean signal at the beginning of each film as shown in Figure 7-11c. As can be seen the background phosphorescence stays constant with time.

Thus, for image correction of MBO film we can use Eq.(7-2), where $s_{i,j}$ and $s'_{i,j}$ refer to signal at (i,j) pixel after and before correction, respectively, Δt refers to dwell time and τ is lifetime which in case of MBO is ~infinity for Δt = 327.68 µs. This is equation is similar to the one used in image construction algorithm for Al_2O_3 films but with different lifetimes.

$$s_{i,j} = s'_{i,j} - \left(\frac{\sum_{j=1}^{N} s'_{i,j}}{\sum_{j=1}^{N} e^{-j\Delta t/\tau}}\right) e^{-j\Delta t/\tau} \qquad \textbf{(7-2)}$$

(a)

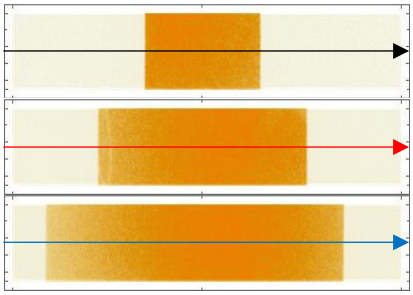

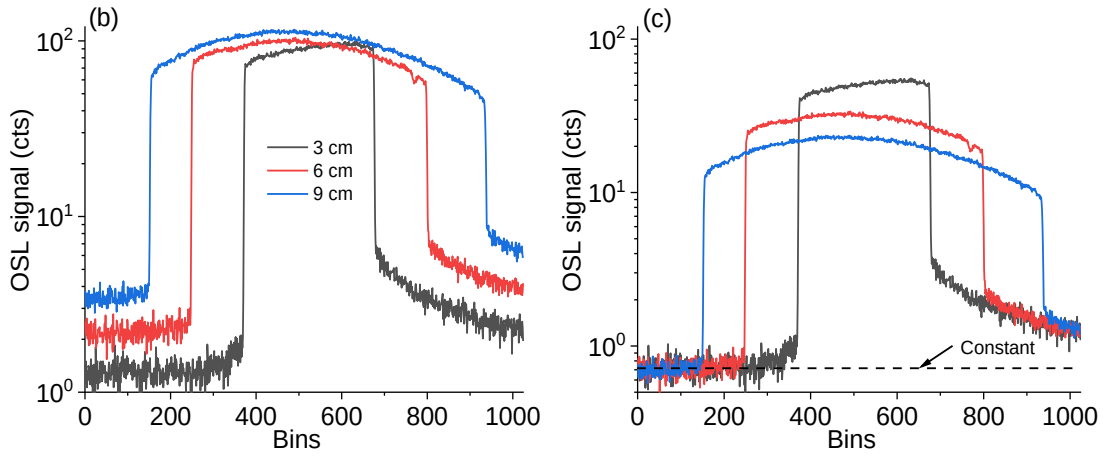

Figure 7-11. Background phosphorescence as a function of the irradiated area for MBO films irradiated with 90 kVp x-ray source in air with ~0.67 Gy total dose. (a) Series of raw images of MBO films, of lengths 3, 6, and 9 cm, respectively, with the same ~1 cm width. (b) Signal profiles (average of 50 rows in one direction only, spanning 100 rows) at the center of each of the images. (c) Estimation of phosphorescence decay time using background phosphorescence.

7.4.2 Phosphorescence bleeding correction

As demonstrated in Section 7.2.3 and Section 7.1, MBO does not require correction for pixel bleeding but some phosphorescence signal is observed at the end of the film after the laser leaves the film. This contribution is probably due to re-trapping of the charges at shallow traps unstable at temperatures below room temperature. These can be corrected using the pixel-bleeding algorithm described by Yukihara and Ahmed (2015), but using the phosphorescence lifetimes from MBO (~4.5 ms and ~ 93 ms). This correction, however, is much lower compared to Al_2O_3, as the phosphorescence contribution in MBO the image is much lower than the slow luminescence contribution due to the F-centers in Al_2O_3.

Figure 7-12 shows the raw image of MBO from Section 7.1 (a) before and (b) after pixel-bleeding, light collection efficiency and geometrical distortion correction is applied. The image reconstruction algorithm was able to correct for the contribution due to phosphorescence signal in the raw image of the MBO film. This data is, of course, just a demonstration, since the MBO

films uniformity is not yet optimum and the irradiation is not necessarily flat. Nevertheless, the objective is to show that the same correction algorithm developed for Al_2O_3:C and Al_2O_3:C,Mg (Yukihara and Ahmed, 2015) applies to MBO provided that the material characteristics are adapted. The amount of correction for the phosphorescence signal of MBO is much lower than the pixel bleeding correction required for MBO, as one can see even in the raw MBO images that little pixel bleeding is present. As a result, less noise is introduced in the case of the MBO correction. The parameter *R* (Yukihara and Ahmed, 2015), the ratio between the slow components (phosphorescence and F-center emission in Al_2O_3) and the fast component, was found to be $R \sim 0.01 – 0.05$ for MgB_4O_7:Ce,Li in comparison with $R \sim 0.5$ and 0.35 for Al_2O_3:C and Al_2O_3:C,Mg films, respectively.

Figure 7-12c shows the signal profiles (average of 2 mm) in x-direction at the center of raw and corrected MBO images. As can be seen the pixel bleeding, background phosphorescence, and the position dependence in the images are corrected. The fluctuations in the signal after correction are due to non-uniformity of this first film samples. Figure 7-12d shows the signal profiles (average of 2 mm) in y-direction at the center of raw and corrected MBO images. There is no pixel bleeding in y-direction except for the, the background phosphorescence signal present at the end of the row which is corrected by the reconstruction algorithm.

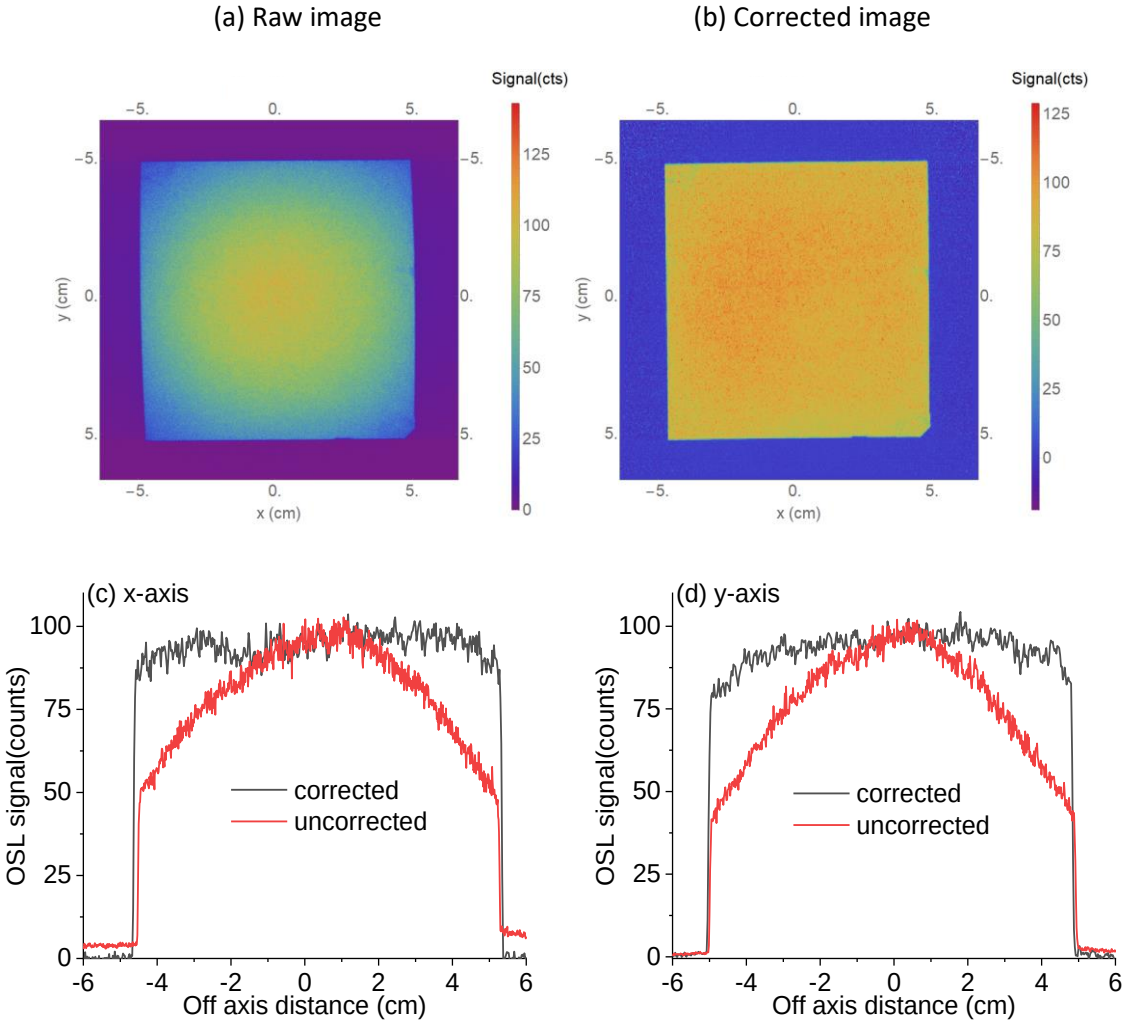

Figure 7-12. (a) Raw image from the 10 cm × 10 cm MBO film irradiated using 90 kVp x-ray source in air with ~0.78 Gy total dose. (b) Image after applying pixel bleeding correction. (c)-(d) Comparion of signal profiles before and after image correction in both directions. Each line profile is an average of 2 mm at the center.

7.5 Dosimetric properties

Even though the MBO films are not yet optimized for final application, preliminary tests using the current samples were performed to evaluate their dosimetric properties and identify potential problems.

7.5.1 Dose response

The goal of this study was to compare the response and sensitivity of the newly developed MBO films to that of Al_2O_3:C and Al_2O_3:C,Mg films in the same experimental conditions. In addition, determine the response of MBO films in steep dose gradient between the region of the film with and without samples. The study was performed using 21 samples of MBO, Al_2O_3:C and Al_2O_3:C,Mg films each, of approximately 1 cm × 1 cm. The detectors were irradiated with doses ranging from 0.1 Gy to 10 Gy (100 mCi $^{90}Sr/^{90}Y$ beta source) using three detectors for each dose. The samples were read simultaneously two days after irradiation using the 2D reader. The images from all material types were then reconstructed using the image reconstruction algorithm.

Figure 7-13a shows the reconstructed image of MBO detectors after all corrections. Each column represents the detectors irradiated with same dose with increasing dose in the x direction. As can be seen, the detectors are well separated demonstrating absence of pixel bleeding. The background signal around the samples with high doses is probably due to stimulation of the film by laser light scattered in the optical filters.

Figure 7-13b shows the signal profiles (average of 2 mm) from the center row of each detector set (Al_2O_3:C and Al_2O_3:C,Mg images not shown). The signal profiles show good repeatability of detectors for all material types.

Figure 7-13c shows that that the dose response for MBO, Al_2O_3:C, and Al_2O_3:C,Mg detectors. The signal was calculated at the center of scan ROI 5 mm × 5 mm of each detectors in the image and the data represent the mean signal for each dose. The error bars represent he standard deviation of the mean signal of 3 detectors irradiated with same dose. MBO shows linear response over range investigated, but in the Al_2O_3 films supralinearity starts to be

observed for doses greater than ~2 Gy. The linear response behavior of MBO and the supralinearity behavior of the Al_2O_3 films has already been reported by in previous work (Ahmed et al., 2017; Yukihara et al., 2017) and these results confirm these findings. The response of this MBO films was found to be ~4 times and ~2.5 times lower than Al_2O_3:C and Al_2O_3:C,Mg respectively. The lower sensitivity of MBO largely depends on the film thickness and scanning parameters, which can be improved by increasing film thickness, or by increasing stimulation intensity or decreasing the stimulation wavelength, or both. Nevertheless, the sensitivity even in the current settings seems to be sufficient for 2D dosimetry in radiotherapy.

(a) MBO

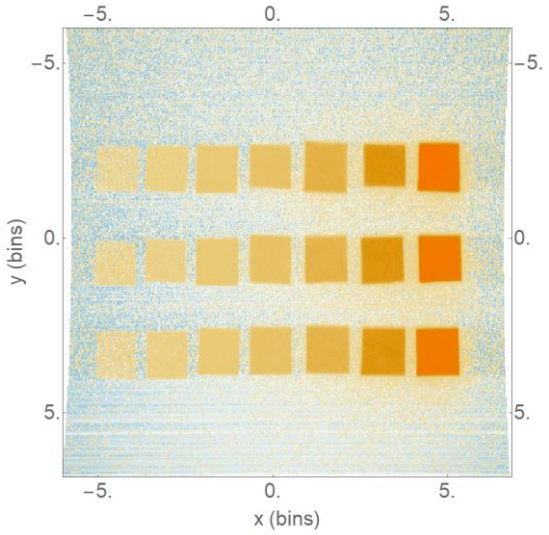

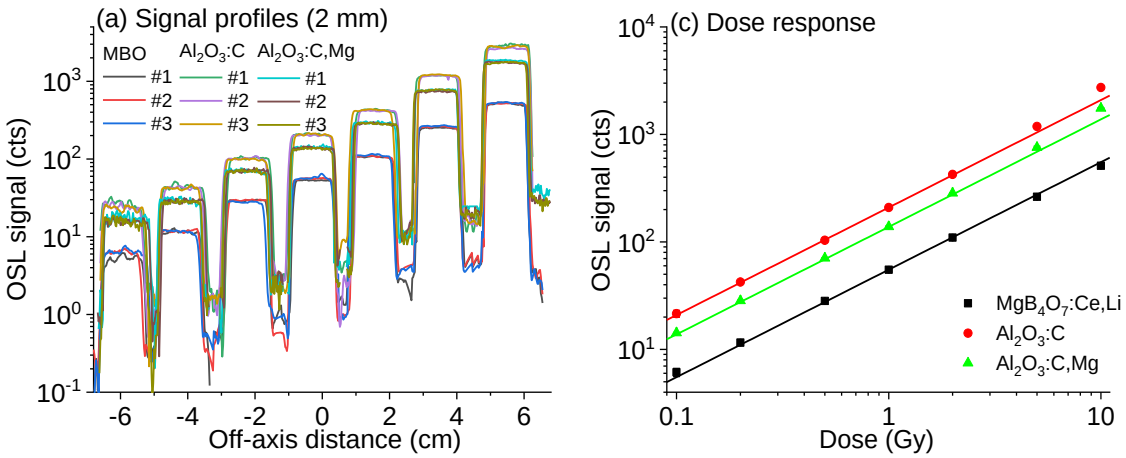

Figure 7-13. (a) Image obtained from readout of 3 sets of smal pieces of MBO, Al_2O_3:C and Al_2O_3:C,Mg detectors (~ 1 cm × 1 cm). Each set contains 9 pieces of detectors irradiated with dose (~0.1 Gy – 10 Gy). (b) Signal profiles from the 3 sets of detectors in x-direction of the image. Each signal profile is averaged over a width of ~ 2mm form the center of the image. (c) Dose response curve of the MBO, Al_2O_3:C and Al_2O_3:C,Mg detectors. Each data point is an average signal over 5 mm × 5 mm (~20 pixels × 20 pixels) around the central axis. The error bars in the dose response curves represent the standard deviation of the mean signal of 3 detectors.

7.5.2 Sensitization and fading

Even though MBO has very attractive properties for 2D dosimetry, sensitization and fading limits the dosimetric performance of MBO. The mechanism behind these two phenomena is complex and still not understood (Gustafson et al., 2019; Yukihara et al., 2017). Thus, the goal of this study is the document the degree of sensitization and fading of current MBO films.

To test sensitization of the samples, 4 sets (3 samples in each set) of MBO (7 mm discs) were irradiated with dose of 0.69 Gy, 2.07 Gy, 6.9 Gy and 20.7 Gy using the beta source of the Risø reader. After irradiation, the samples were then read for 600 s using green LEDs at 90% intensity and bleached overnight in the bleaching unit (Section 3.2). This sequence was repeated five times.

Figure 7-14 shows the initial OSL intensity (average of first 3 seconds) and OSL area (600s of stimulation) normalized to the first run from the sample irradiated with all doses. As can be seen the degree sensitization increases with increases dose and can be conclude that its dose dependent. Gustafson et al. (2019) have proposed that the sensitization in MBO is due to incomplete bleaching of the films, which still needs to be investigated in detail. If it is the case, the current beaching procedure is insufficient to bleach the films and needs further investigation to determine the best bleaching procedure.

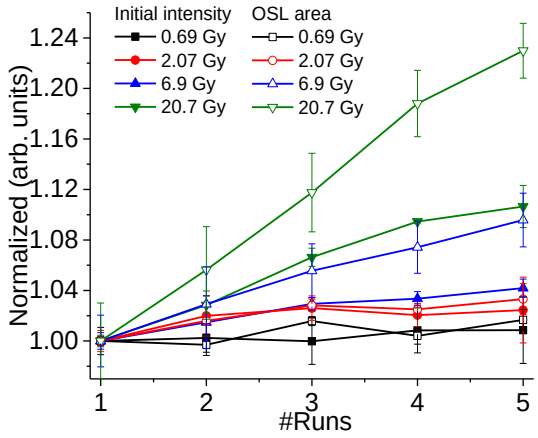

Figure 7-14. OSL initial intensity and OSL area for repeated irradiation and bleaching normalized to run 1 for different doses. The error bars indicate the standard deviation of the 3 samples. After each run, the samples were bleached overnight using the bleaching unit (Section 3.2).

In this study the dark fading of the OSL signal for various durations of time following irradiation was measured. The test was performed irradiating 27 MBO samples (7 mm disc) with 30 s (beta) and allowed to sit in dark for periods up to 72 h. Three samples were used for each fading time. The samples were then read using the Risø reader and green LEDs at 90% intensity. Following the readout, the samples were irradiated with a reference dose of 30 s (beta) and readout immediately post irradiation. The OSL signal from the reference dose (S_R) were used to normalize the faded OSL signal (S) to account for any sample variations. The ratio was then normalized to the signal at 30 min post irradiation.

Figure 7-15 shows OSL dark fading for MBO samples for various periods 72 h post irradiation. The initial OSL intensity (average of first 3 seconds) and total OSL area were normalized to reference dose and renormalize to signal at 30 min. MBO has substantial fading over 72 h post irradiation. The initial OSL intensity fades to ~55% from 30 min to 72 h post irradiation and the total OSL are fades to ~80% from 30 min to 72 h post irradiation.

The fading seems to be mainly immediately after irradiation, as is the case with many new OSL materials. This shows that this may be a result of shallow traps depleting at room temperature. This can possibly be minimized with preheating the samples before readout. However, further investigation is required.

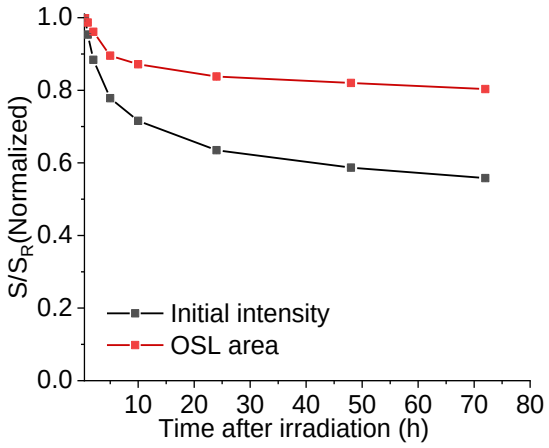

Figure 7-15. OSL dark fading of MgB_4O_7:Ce,Li samples irradiated with 2.07 Gy. The signal is normalized to the OSL signal at 30 min after irradiation.

CHAPTER VIII

CONCLUSIONS

The goal of this work was advance OSL-based 2D dosimetry in radiotherapy by improving the image reconstruction algorithm required for Al_2O_3 films, demonstrate the application of the Al_2O_3 films in small field dosimetry and MRgRT, and finally, investigate the possibility of 2D dosimetry using MgB_4O_7:Ce,Li films.

The initial tests for improving the noise in OSL images were done by implementing various approaches to the Tikhonov algorithm in the pixel bleeding algorithm and applying it to 1D simulated OSL data varying materials luminescence lifetime, the ratio of F-center to F^+-center, and dwell times. The simulation results of 1D flat field profiles and Gaussian profiles showed that the Tikhonov-L2 algorithm (see 0) improves the noise in the signal compared to the LS-algorithm. We further applied the Tikhonov-L2 algorithm to experimental results on flat field irradiations using a 6 MV linac (Siemens Oncor) and small fields using an Accuray CyberKnife. The application of Tikhonov-L2 algorithm on the 1D profiles of the experimental results showed significant improvement in noise, in the case of flat field irradiations by at least 2 times in the flat field signal profiles for doses ranging from 0.01 Gy – 10 Gy.

The results based on implementation of Tikhonov -L2 algorithm in the 2D OSL images showed improvements in image noise. We characterized and evaluated the effect of the

regularization parameter (λ) in the image noise and spatial resolution of the OSL films. The image noise decreases significantly with increasing λ parameters but the spatial resolution gets worse. In addition, we found that it affects the directional dependence in the images where the noise in the scanning direction decreases more than in the sub-scan direction with increasing λ parameter. Therefore, we found that the λ parameter that best reduces the image noise, maintains the spatial resolution and solves the directional dependence in the image for current settings. When compared to a noise filter (Wiener filter), however, we did not find significant improvement to the image noise of the OSL images. Nevertheless, Tikhonov -L2 algorithm solves the directional dependence in the image. We showed that the application of Tikhonov -L2 algorithm does not affect the dosimetric properties of the OSL films. Thus, Tikhonov -L2 algorithm should be implemented in the image reconstruction algorithm and additional noise filter (Wiener filter) can be used to remove additional image noise.

We demonstrated the possibility of application of OSL films in small field dosimetry. We performed initial tests by measuring the Tissue Phantom Ratios (TPR), Off-Central Ray Ratios (OCR), and Output Factors (OF's) in CyberKnife. The OSL films overestimate the output factors compared to diode measurements for the cone sizes studied. The OCR measurements show good agreement with the diode for cone size of 5.0 mm and 7.5 mm, but the discrepancies were larger for larger cone sizes. The TPR measurements agree well with the diode measurements within 1% at depths >10 mm; for depths below 10 mm (buildup region) the differences may be due to difference in the energy dependence of the two detectors. Nevertheless, these measurements are our first attempt at small field dosimetry using OSL films which shows good agreement with diode detectors. Further measurements with additional reference detectors like

radiochromic films combined with Monte-Carlo simulations would be helpful to have a complete study in order to determine the feasibility of using OSL films for small field dosimetry.

We performed initial tests using OSL detectors to test the effect angle of irradiation in presence of magnetic field, and its transmission. The dose measured using the Al_2O_3:C (Mipox) detectors for +90° and – 90° irradiation orientations agrees within 1%. Further tests with additional irradiation angles of 0°, 45°, 90°, 270° and 315° showed a variation of within ~1.4% with the mean dose. The transmission measurements show that the Mipox detectors do not affect the transmission of the beam. The tests with irradiation angle dependence show an increase in the dose measured by the Mipox detectors. It is unclear if the setup geometry causes the increase in dose and therefore, more studies need to be done. A gamma analysis algorithm was written and used to compare the IMRT plan irradiations on OSL images to the TPS data. The gamma analysis of the treatment plan shows good agreement with the TPS. Gamma criteria of 3 % and 3 mm show a passing rate of > 90 % for both film types and IMRT plans. However, with tighter gamma criteria and low dose irradiations, the passing rate decreases due to increased uncertainties for low dose measurements using OSL.

The initial studies of MgB_4O_7:Ce,Li films demonstrate the possibility of 2D dosimetry for radiotherapy applications. Even though the current setup of 2D reader are not fully optimized for these films, we were able to demonstrate the advantage of MBO over Al_2O_3:C or Al_2O_3:C,Mg films. The fast luminescence lifetime of ~ 32.2 ns associated with Ce^{3+} emission offers an advantage for laser-scanning readout, minimizing the need for pixel-bleeding correction required for Al_2O_3:C or Al_2O_3:C,Mg film dosimetry. We characterized the luminescence components in the material which showed short and long-term phosphorescence components. This contribution, however, is relatively low compared to the main emission and can be reduced

or eliminated with faster scanning speeds. However, in the current conditions, the same pixel bleeding algorithm that was used for Al_2O_3 films was successfully applied to MBO images to correct for the pixel bleeding due to the phosphorescence signal. A dose response curve was obtained with MBO film pieces, which shows a linear dose response up to 10 Gy with steep dose gradients. The OSL signal in the MBO films could be satisfactorily bleached using the bleaching unit with the background equivalent dose of <0.5 mGy, which is acceptable for radiotherapy applications. The main disadvantage of MBO is fading, sensitization and the lack of understanding of the processes causing it. The sensitivity of the material increases with the previous dose and has significant dark fading, which makes it difficult to be used for precise dosimetry.

In the future studies, Gafchromic film measurements in CyberKnife needs to be included to better understand the differences between the OSL films and diode detectors. Furthermore, Monte carlo simulations of the irradiation plan may provide additional information to compare the detectors measurements. The tests should include repeating output factor measurements, as current measurements show a large deviation from the diode measurements. The OCR measurements need to be redone alongside gafchromic films in the same irradiation setup for comparison. SRS treatment plans can be irradiated on OSL films and gamma analysis can be done to test the overall performance of the films.

Additional tests using the Mipox detectors regarding the influence of the magnetic field need to be done. In addition, other clinical applications would be to test the detectors in in-vivo dose measurements for Total Body Irradiation treatments in the presence of magnetic field. Even though we are limited to the OSL reader scanning area of 15 cm × 15 cm IMRT treatment

plan irradiations with larger field sizes on larger films can be done and gamma analysis can be performed to compare the OSL film results with the TPS data.

The two main drawbacks of MBO (sensitization and dark fading) needs further investigation. Therefore, future research should focus on identifying the causes for these effects, so that these problems can be minimized by the use of appropriate bleaching or pre-readout procedures, or by further material developments to reduce the trapping centers associated with these processes. The possibility of eliminating the phosphorescence bleeding in the image by scanning the MBO films with faster scanning speeds needs to be investigated. If the pixel bleeding still persists we need to further investigate the application of pixel bleeding algorithm for MBO films.

In conclusion, there is huge potential for 2D OSL dosimetry in small field dosimetry and MRgRT. Currently, there is no single detector that can be used independently for small field dose measurements. In addition, challenges faced by many dosimeters in MRgRT due to the presence of magnetic field indicate a need for new dosimetry techniques. Radiochromic films are the only film dosimetry commercially used in radiotherapy. However, due to the difficulties in measuring absolute dose it has been limited to relative dose measurements only and other detectors are used for absolute dose measurements. In addition, it is not reusable, which increases the cost to the clinic and therefore, use of films in radiotherapy have been fading. 2D dosimetry using OSL is a new technique in film dosimetry that overcomes most of the weaknesses of radiochromic films. In our tests, we showed initial tests in both small field dosimetry and MRgRT. The results using Al_2O_3 films are promising and shows the potential of 2D OSL dosimetry in both areas. In addition to Al_2O_3, the development of new OSL materials can

pave the way to overcome some challenges faced by Al_2O_3. The results from newly developed MBO films show no need for pixel bleeding algorithm but suffers from fading and sensitization.

Currently, Al_2O_3 films are suitable to make further progress in 2D OSL dosimetry. However, more studies need to done to understand the luminescence mechanism in MBO and further develop the material (or identify new materials). The current goal for OSL film dosimetry is to have a material with all the necessary dosimetric properties and can be read out immediately post-irradiation with minimal fading, is reusable and uses a compact reader for readout.

REFERENCES

Ahmed, M.F., Eller, S., Schnell, E., Ahmad, S., Akselrod, M.S. and Yukihara, E.G., 2014. *Development of a 2D dosimetry system based on the optically stimulated luminescence of Al_2O_3*. Radiat. Meas. 71, 187-192.

Ahmed, M.F., Schnell, E., Ahmad, S. and Yukihara, E.G., 2016. *Image reconstruction algorithm for optically stimulated luminescence 2D dosimetry using laser-scanned Al_2O_3 films*. Phys. Med. Biol. 61, 7484-7506.

Ahmed, M.F., 2016. *Development and demonstration of 2D dosimetry using optically stimulated luminescence from new Al2O3 films for radiotherapy applications*. Oklahoma State University.

Ahmed, M.F., Shrestha, N., Ahmad, S., Schnell, E., Akselrod, M.S. and Yukihara, E.G., 2017. *Demonstration of 2D dosimetry using Al2O3 optically stimulated luminescence films for therapeutic megavoltage x-ray and ion beams*. Radiat. Meas. 106, 315-320.

Akselrod, M. and Kortov, V., 1990. *Thermoluminescent and exoemission properties of new high-sensitivity TLD a-Al2O3: C crystals*. Radiation Protection Dosimetry 33, 123-126.

Akselrod, M. and McKeever, S., 1999. *A radiation dosimetry method using pulsed optically stimulated luminescence*. Radiat. Prot. Dosim. 81, 167-175.

Akselrod, M., Bøtter-Jensen, L. and McKeever, S., 2006. *Optically stimulated luminescence and its use in medical dosimetry*. Radiat. Meas. 41, S78-S99.

Akselrod, M.S., Kortov, V.S., Kravetsky, D.J. and Gotlib, V.I., 1990. *Highly sensitive thermoluminescent anion-defect a-Al_2O_3:C single crystal detectors*. Radiat. Prot. Dosim. 33, 119-122.

Akselrod, M.S., Akselrod, A.E., Orlov, S.S., Sanyal, S. and Underwood, T.H., 2003. *Fluorescent Aluminum Oxide Crystals for Volumetric Optical Data Storage and Imaging Applications*. J. Fluoresc. 13, 503-511.

Akselrod, M.S., 2006. *New Al_2O_3:C,Mg crystals for radiophotoluminescent dosimetry and optical imaging*. Radiat. Prot. Dosim. 119, 218-221.

Ariga, E., Ito, S., Deji, S., Saze, T. and Nishizawa, K., 2007. *Development of dosimetry using detectors of diagnostic digital radiography systems*. Med. Phys. 34, 166-174.

Aspradakis, M.M., 2009. *Small Field MV Photon Dosimetry*. Berlin, Heidelberg, Springer Berlin Heidelberg, World Congress on Medical Physics and Biomedical Engineering, September 7 - 12, 2009, Munich, Germany, 854-854.

Aspradakis, M.M., Byrne, J.P., Palmans, H., Duane, S., Conway, J., Warrington, A.P. and Rosser, K., 2010. *IPEM report 103: Small field MV photon dosimetry*. IAEA-CN--182, International Atomic Energy Agency (IAEA), pp. 41-42.

Attix, F.H., 2008. *Introduction to radiological physics and radiation dosimetry*. John Wiley & Sons.

Borca, V.C., Pasquino, M., Russo, G., Grosso, P., Cante, D., Sciacero, P., Girelli, G., Porta, M.R.L. and Tofani, S., 2013. *Dosimetric characterization and use of GAFCHROMIC EBT3 film for IMRT dose verification*. J. Appl. Clin. Med. Phys. 14, 158-171.

Bøtter-Jensen, L., McKeever, S.W. and Wintle, A.G., 2003. *Optically stimulated luminescence dosimetry*. Elsevier.

Chen, X., Prior, P., Chen, G.P., Schultz, C.J. and Li, X.A.J.M.p., 2016. *Dose effects of 1.5 T transverse magnetic field on tissue interfaces in MRI-guided radiotherapy*. Med. Phys. 43, 4797-4802.

Crijns, W., Vandenbroucke, D., Leblans, P. and Depuydt, T., 2017. *A reusable OSL-film for 2D radiotherapy dosimetry*. Phys. Med. Biol. 62, 8441.

Cui, S., Zhu, X., Wang, W. and Xie, Y., 2009. *Calibration of a laser galvanometric scanning system by adapting a camera model*. Appl. Opt. 48, 2632-2637.

Das, I.J., Downes, M.B., Kassaee, A. and Tochner, Z.J., 2000. *Choice of Radiation Detector in Dosimetry of Stereotactic Radiosurgery-Radiotherapy*. Journal of Radiosurgery 3, 177-186.

Das, I.J., Ding, G.X. and Ahnesjo, A., 2008. *Small fields: Nonequilibrium radiation dosimetry*. Med. Phys. 35, 206-215.

De Wagter, C., 2004. *The ideal dosimeter for intensity modulated radiation therapy (IMRT): What is required?* Journal of Physics: Conference Series 3, 4-8.

Denis, G., Rodriguez, M.G., Akselrod, M.S., Underwood, T.H. and Yukihara, E.G., 2011a. *Time-resolved measurements of optically stimulated luminescence of Al_2O_3:C and Al_2O_3:C,Mg*. Radiat. Meas. 46, 1457-1461.

Denis, G., Akselrod, M. and Yukihara, E., 2011b. *Influence of shallow traps on time-resolved optically stimulated luminescence measurements of Al2O3: C, Mg*. J. Appl. Phys. 109, 104906.

Derreumaux, S., Etard, C., Huet, C., Trompier, F., Clairand, I., Bottollier-Depois, J.F., Aubert, B. and Gourmelon, P., 2008. *Lessons from recent accidents in radiation therapy in France*. Radiat. Prot. Dosim. 131, 130-135.

Devic, S., 2011. *Radiochromic film dosimetry: past, present, and future*. Physica Med. 27, 122-134.

Duma, V., Podoleanu, A.G. and Nicolov, M., 2009. *Modeling a galvoscanner with an optimized scanning function*. In: SYROM 2009. Springer, 539-548.

Evans, B.D. and Stapelbroek, M., 1978. *Optical properties of the F^+ center in crystalline Al_2O_3*. Phys. Rev. B 18, 7089-7098.

Ezzell, G.A., Burmeister, J.W., Dogan, N., LoSasso, T.J., Mechalakos, J.G., Mihailidis, D., Molineu, A., Palta, J.R., Ramsey, C.R., Salter, B.J., Shi, J., Xia, P., Yue, N.J. and Xiao, Y., 2009. *IMRT comissioning: Multiple institution planning and dosimetry comparison, a report from AAPM Task Group 119*. Med. Phys. 36, 5359-5373.

Fallone, B., Murray, B., Rathee, S., Stanescu, T., Steciw, S., Vidakovic, S., Blosser, E. and Tymofichuk, D., 2009. *First MR images obtained during megavoltage photon irradiation from a prototype integrated linac-MR system*. Med. Phys. 36, 2084-2088.

Francescon, P., Kilby, W., Satariano, N. and Cora, S., 2012. *Monte Carlo simulated correction factors for machine specific reference field dose calibration and output factor measurement using fixed and iris collimators on the CyberKnife system*. Phys. Med. Biol. 57, 3741.

Francescon, P., Kilby, W. and Satariano, N., 2014. *Monte Carlo simulated correction factors for output factor measurement with the CyberKnife system—results for new detectors and correction factor dependence on measurement distance and detector orientation*. Phys. Med. Biol. 59, N11-N17.

Gomez, A., Gonzalez, R., Lindenboim, D., Mugliaroli, H., Ortigueira, C., Papadopulos, C. and Placer, A., 1973. *Manual of dosimetry in radiotherapy*. Comision Nacional de Energia Atomica.

Gustafson, T.D., Milliken, E.D., Jacobsohn, L.G. and Yukihara, E.G., 2019. *Progress and challenges towards the development of a new optically stimulated luminescence (OSL) material based on MgB4O7:Ce,Li*. J. Lumin. 212, 242-249.

Haasbeek, C., Palma, D., Visser, O., Lagerwaard, F., Slotman, B. and Senan, S., 2012. *Early-stage lung cancer in elderly patients: a population-based study of changes in treatment patterns and survival in the Netherlands*. Annals of oncology 23, 2743-2747.

Hall, W.A., Colbert, L., Nickleach, D., Shelton, J., Marcus, D.M., Switchenko, J., Rossi, P.J., Godette, K., Cooper, S. and Jani, A.B., 2013. *Reduced acute toxicity associated with the use of volumetric modulated arc therapy for the treatment of adenocarcinoma of the prostate*. Prac. Rad. Oncol. 3, e157-e164.

Han, Z., Driewer, J.P., Zheng, Y., Low, D.A. and Li, H.H., 2009. *Quantitative megavoltage radiation therapy dosimetry using the storage phosphor*. Med. Phys. 36, 3748-3757.

Hansen, P.C., 1992a. *Analysis of discrete ill-posed problems by means of the L-curve*. SIAM review 34, 561-580.

Hansen, P.C., 1992b. *Numerical tools for analysis and solution of Fredholm integral equations of the first kind*. Inverse Probl. 8, 849.

Idri, K., Santoro, L., Charpiot, E., Herault, J., Costa, A., Ailleres, N., Delard, R., Vaille, J.R., Fesquet, J. and Dusseau, L., 2004. *Quality control of intensity modulated radiation therapy with optically stimulated luminescent films*. IEEE. Trans. Nucl. Sci 51, 3638-3641.

Jaffray, D., Carlone, M., Menard, C. and Breen, S., 2010. *Image-guided radiation therapy: Emergence of MR-guided radiation treatment (MRgRT) systems*. In: Medical Imaging 2010: Physics of Medical Imaging, International Society for Optics and Photonics, 762202.

Jahn, A., Sommer, M. and Henniger, J., 2010. *2D-OSL-dosimetry using beryllium oxide*. Radiat. Meas. 45, 674-676.

Jelen, U. and Begg, J., 2019. *Dosimetry needs for MRI-linacs*. In: Journal of Physics: Conference Series, IOP Publishing, 012010.

Jin, H., Keeling, V.P., Johnson, D.A. and Ahmad, S., 2014. *Interplay effect of angular dependence and calibration field size of MapCHECK 2 on RapidArc quality assurance*. J. Appl. Clin. Med. Phys. 15, 80-92.

Jursinic, P.A., 2007. *Characterization of optically stimulated luminescent dosimeters, OSLDs, for clinical dosimetric measurements*. Med. Phys. 34, 4594-4604.

Kilby, W., Dooley, J., Kuduvalli, G., Sayeh, S. and Maurer Jr, C., 2010. *The CyberKnife® robotic radiosurgery system in 2010*. Technol Cancer Res Treat. 9, 433-452.

Klein, E.E., Hanley, J., Bayouth, J., Yin, F.F., Simon, W., Dresser, S., Serago, C., Aguirre, F., Ma, L. and Arjomandy, B., 2009. *Task Group 142 report: Quality assurance of medical accelerators a*. Med. Phys. 36, 4197-4212.

Kouwenberg, J., 2018. *Fluorescent Nuclear Track Detectors for Alpha Particle Measurement*. Delft University of Technology.

Laub, W.U. and Wong, T., 2003. *The volume effect of detectors in the dosimetry of small fields used in IMRT*. Med. Phys. 30, 341-347.

Lee, K. and Crawford Jr, J., 1977. *Electron centers in single-crystal Al 2 O 3*. Phys. Rev. B 15, 4065.

Leksell, L.P., 1983. *Stereotactic radiosurgery*. J. Neurol. Neurosurg. 46, 797-803.

Létourneau, D., Gulam, M., Yan, D., Oldham, M. and Wong, J.W., 2004. *Evaluation of a 2D diode array for IMRT quality assurance*. Radiother. Oncol. 70, 199-206.

Low, D.A., Harms, W.B., Mutic, S. and Purdy, J.A., 1998. *A technique for the quantitative evaluation of dose distributions*. Med. Phys. 25, 656-661.

Low, D.A., Parikh, P., Dempsey, J.F., Wahab, S. and Huq, S., 2003. *Ionization chamber volume averaging effects in dynamic intensity modulated radiation therapy beams*. Med. Phys. 30, 1706-1711.

Manakov, A., Seidel, H.-P. and Ihrke, I., 2011. *A mathematical model and calibration procedure for galvanometric laser scanning systems*.

Meijsing, I., Raaymakers, B.W., Raaijmakers, A., Kok, J., Hogeweg, L., Liu, B. and Lagendijk, J.J., 2009. *Dosimetry for the MRI accelerator: the impact of a magnetic field on the response of a Farmer NE2571 ionization chamber*. Phys. Med. Biol. 54, 2993.

Micke, A., Lewis, D.F. and Yu, X., 2011. *Multichannel film dosimetry with nonuniformity correction*. Medical physics 38, 2523-2534.

Mutic, S. and Dempsey, J.F., 2014. *The ViewRay system: magnetic resonance–guided and controlled radiotherapy*. In: Semin. Radiat. Oncol., Elsevier, 196-199.

Nutting, C.M., Morden, J.P., Harrington, K.J., Urbano, T.G., Bhide, S.A., Clark, C., Miles, E.A., Miah, A.B., Newbold, K. and Tanay, M., 2011. *Parotid-sparing intensity modulated versus conventional radiotherapy in head and neck cancer (PARSPORT): a phase 3 multicentre randomised controlled trial*. Lancet Oncol. 12, 127-136.

O'Brien, D., Schupp, N., Pencea, S., Dolan, J. and Sawakuchi, G., 2017. *Dosimetry in the presence of strong magnetic fields*. In: Journal of Physics: Conference Series, IOP Publishing, 012055.

Oliveira, L., Milliken, E. and Yukihara, E., 2013. *Development and characterization of MgO: Nd, Li synthesized by solution combustion synthesis for 2D optically stimulated luminescence dosimetry*. J. Lumin. 133, 211-216.

Palmer, A.L., Dimitriadis, A., Nisbet, A. and Clark, C.H., 2015. *Evaluation of Gafchromic EBT-XD film, with comparison to EBT3 film, and application in high dose radiotherapy verification*. Phys. Med. Biol. 60, 8741.

Parwaie, W., Refahi, S., Ardekani, M.A., Farhood, B.J.J.o.m.s. and sensors, 2018. *Different dosimeters/detectors used in small-field dosimetry: Pros and cons*. J. Med. Sig. 8, 195.

Poppe, B., Blechschmidt, A., Djouguela, A., Kollhoff, R., Rubach, A., Willborn, K.C. and Harder, D., 2006. *Two-dimensional ionization chamber arrays for IMRT plan verification*. Med. Phys. 33, 1005-1015.

Pradhan, A., Lee, J. and Kim, J., 2008. *Recent developments of optically stimulated luminescence materials and techniques for radiation dosimetry and clinical applications*. Journal of medical physics/Association of Medical Physicists of India 33, 85.

Prokić, 1980. *Development of highly sensitive CaSO4: Dy/Tm and MgB4O7: Dy/Tm sintered thermoluminescent dosimeters*. Nucl. Instrum. Methods Phys. Res. A 175, 83-86.

Raaijmakers, A., Raaymakers, B.W., Lagendijk, J.J.J.P.i.M. and Biology, 2005. *Integrating a MRI scanner with a 6 MV radiotherapy accelerator: dose increase at tissue–air interfaces in a lateral magnetic field due to returning electrons*. Phys. Med. Biol. 50, 1363.

Reft, C.S., 2009. *The energy dependence and dose response of a commercial optically stimulated luminescent detector for kilovoltage photon, megavoltage photon, and electron, proton, and carbon beams*. Med. Phys. 36, 1690-1699.

Reynolds, M., Fallone, B. and Rathee, S.J.M.p., 2013. *Dose response of selected ion chambers in applied homogeneous transverse and longitudinal magnetic fields*. Med. Phys. 40, 042102.

Reynolds, M., Fallone, B. and Rathee, S., 2014. *Dose response of selected solid state detectors in applied homogeneous transverse and longitudinal magnetic fields*. Med. Phys. 41.

Reynolds, M., Fallone, B. and Rathee, S.J.M.p., 2015. *Response measurement for select radiation detectors in magnetic fields*. Med. Phys. 42, 2837-2840.

Reynoso, F.J., Curcuru, A., Green, O., Mutic, S., Das, I.J. and Santanam, L., 2016. *Technical Note: Magnetic field effects on Gafchromic-film response in MR-IGRT*. Med. Phys. 43, 6552-6556.

Rodriguez, M.G., Denis, G., Akselrod., M.S., Underwood, T.H. and Yukihara, E.G., 2011. *Thermoluminescence, optically stimulated luminescence and radioluminescence properties of Al_2O_3:C,Mg*. Radiat. Meas. 46, 1469-1473.

Rowlands, J.A., 2002. *The physics of computed radiography*. Phys. Med. Biol. 47, R123.

Schuyt, J. and Williams, G., 2019. *Development of a 2D dosimeter using the optically stimulated luminescence of NaMgF3: Eu with CCD camera readout*. Radiat. Meas. 121, 99-102.

Souza, L., Silva, A., Antonio, P., Caldas, L., Souza, S., d'Errico, F. and Souza, D.J.R.M., 2017. *Dosimetric properties of MgB4O7: Dy, Li and MgB4O7: Ce, Li for optically stimulated luminescence applications*. Radiat. Meas. 106, 196-199.

Souza, L.F., Souza, D.N., Rivera, G.B., Vidal, R.M. and Caldas, L.V.J.P.i.S., 2019. *Dosimetric characterization of MgB4O7: Ce, Li as an optically stimulated dosimeter for photon beam radiotherapy*. Journal of Perspectives in Science 12, 100397.

Spindeldreier, C., Schrenk, O., Ahmed, M.F., Shrestha, N., Karger, C., Greilich, S., Pfaffenberger, A. and Yukihara, E.J.R.M., 2017. *Feasibility of dosimetry with optically stimulated luminescence detectors in magnetic fields*. Radiat. Meas. 106, 346-351.

Stefanowicz, S., Latzel, H., Lindvold, L.R., Andersen, C.E., Jäkel, O. and Greilich, S., 2013. *Dosimetry in clinical static magnetic fields using plastic scintillation detectors*. Radiat. Meas. 56, 357-360.

Sykora, G.J., Akselrod, M.S., Salasky, M. and Marino, S.A., 2007. *Novel Al_2O_3:C,Mg fluorescent nuclear track detector for passive neutron dosimetry*. Radiat. Prot. Dosim. 126, 278-283.

Thariat, J., Hannoun-Levi, J.-M., Myint, A.S., Vuong, T. and Gérard, J.-P., 2013. *Past, present, and future of radiotherapy for the benefit of patients*. Nat. Rev. Clin. Oncol. 10, 52.

Viamonte, A., Da Rosa, L., Buckley, L., Cherpak, A. and Cygler, J., 2008. *Radiotherapy dosimetry using a commercial OSL system*. Med. Phys. 35, 1261-1266.

White, D.R., Booz, J., Griffith, R.V., Spokas, J.J. and Wilson, I.J., 2016. *Report 44*. J. ICRU. os23, NP-NP.

Wolfram Research, I., 2015. *Mathematica* (computer program).

Wuerfel, J., 2013. *Dose measurements in small fields*. Med. Phys. 1, 81-90.

Xie, J., Huang, S., Duan, Z., Shi, Y. and Wen, S., 2005. *Correction of the image distortion for laser galvanometric scanning system*. Opt Laser Technol. 37, 305-311.

Yukihara, E., Yoshimura, E., Lindstrom, T., Ahmad, S., Taylor, K. and Mardirossian, G., 2005. *High-precision dosimetry for radiotherapy using the optically stimulated luminescence technique and thin Al2O3: C dosimeters*. Phys. Med. Biol. 50, 5619.

Yukihara, E. and McKeever, S., 2006. *Spectroscopy and optically stimulated luminescence of Al 2 O 3: C using time-resolved measurements*. J. Appl. Phys. 100, 083512.

Yukihara, E.G. and McKeever, S.W., 2011. *Optically stimulated luminescence: fundamentals and applications*. John Wiley & Sons.

Yukihara, E.G. and Ahmed, M.F., 2015. *Pixel bleeding correction in laser scanning luminescence imaging demonstrated using optically stimulated luminescence*. IEEE Trans. Med. Imaging 34, 2506-2517.

Yukihara, E.G., Doull, B.A., Ahmed, M.F., Brons, S., Tessonnier, T., Jäkel, O. and Greilich, S., 2015. *Time-resolved optically stimulated luminescence of Al_2O_3:C for Ion Beam Therapy Dosimetry*. Phys. Med. Biol. 60, 6613-6638.

Yukihara, E.G., Doull, B.A., Gustafson, T., Oliveira, L.C., Kurt, K. and Milliken, E.D., 2017. *Optically stimulated luminescence of MgB_4O_7:Ce,Li for gamma and neutron dosimetry*. J. Lumin. 183, 525-532.

Yukihara, E.G.J.R.m., 2011. *Luminescence properties of BeO optically stimulated luminescence (OSL) detectors*. Radiat. Meas. 46, 580-587.

VITA

Nishan Shrestha

Candidate for the Degree of

Doctor of Philosophy

Dissertation: FURTHER DEVELOPMENTS IN 2D OPRTICALLY STIMUALTED LUMINESCENCE DOSIMETRY BASED ON Al_2O_3 AND MGB_4O_7

Major Field: Physics

Biographical:

Education:

Completed the requirements for the Doctor of Philosophy in Physics at Oklahoma State University, Stillwater, Oklahoma in May, 2020.

Completed the requirements for the Master of Science in Physics at Oklahoma State University, Stillwater, Oklahoma in 2017.

Completed the requirements for the Bachelor of Science in Engineering Physics at Southern Arkansas University, Magnolia, Arkansas in 2013.

Experience:

Graduate Teaching Assistant at Oklahoma State University (2018-2020)
Graduate Research Assistant at Oklahoma State University (2013-2018)

Professional Memberships:

American Association of Physicist in Medicine (AAPM)
American Physics Society (APS)